arXiv:0910.1608v4 [astro-ph.HE] 20 Dec 2010

Ap J Suppl 187, 460 (2010)

The First Fermi Large Area Telescope Catalog of Gamma-ray Pulsars

A. A. Abdo[2,3], M. Ackermann[4], M. Ajello[4], W. B. Atwood[5], M. Axelsson[6,7], L. Baldini[8], J. Ballet[9], G. Barbiellini[10,11], M. G. Baring[12], D. Bastieri[13,14], B. M. Baughman[15], K. Bechtol[4], R. Bellazzini[8], B. Berenji[4], R. D. Blandford[4], E. D. Bloom[4], E. Bonamente[16,17], A. W. Borgland[4], J. Bregeon[8], A. Brez[8], M. Brigida[18,19], P. Bruel[20], T. H. Burnett[21], S. Buson[14], G. A. Caliandro[18,19,1], R. A. Cameron[4], F. Camilo[22], P. A. Caraveo[23], J. M. Casandjian[9], C. Cecchi[16,17], Ö. Çelik[24,25,26], E. Charles[4], A. Chekhtman[2,27], C. C. Cheung[24], J. Chiang[4], S. Ciprini[16,17], R. Claus[4], I. Cognard[28], J. Cohen-Tanugi[29], L. R. Cominsky[30], J. Conrad[31,7,32], R. Corbet[24,26], S. Cutini[33], P. R. den Hartog[4], C. D. Dermer[2], A. de Angelis[34], A. de Luca[23,35], F. de Palma[18,19], S. W. Digel[4], M. Dormody[5], E. do Couto e Silva[4], P. S. Drell[4], R. Dubois[4], D. Dumora[36,37], C. Espinoza[38], C. Farnier[29], C. Favuzzi[18,19], S. J. Fegan[20], E. C. Ferrara[24,1], W. B. Focke[4], P. Fortin[20], M. Frailis[34], P. C. C. Freire[39], Y. Fukazawa[40], S. Funk[4], P. Fusco[18,19], F. Gargano[19], D. Gasparrini[33], N. Gehrels[24,41], S. Germani[16,17], G. Giavitto[42], B. Giebels[20], N. Giglietto[18,19], P. Giommi[33], F. Giordano[18,19], T. Glanzman[4], G. Godfrey[4], E. V. Gotthelf[22], I. A. Grenier[9], M.-H. Grondin[36,37], J. E. Grove[2], L. Guillemot[36,37], S. Guiriec[43], C. Gwon[2], Y. Hanabata[40], A. K. Harding[24], M. Hayashida[4], E. Hays[24], R. E. Hughes[15], M. S. Jackson[31,7,44], G. Jóhannesson[4], A. S. Johnson[4], R. P. Johnson[5], T. J. Johnson[24,41], W. N. Johnson[2], S. Johnston[45], T. Kamae[4], G. Kanbach[46], V. M. Kaspi[47], H. Katagiri[40], J. Kataoka[48,49], N. Kawai[48,50], M. Kerr[21], J. Knödlseder[51], M. L. Kocian[4], M. Kramer[38,52], M. Kuss[8], J. Lande[4], L. Latronico[8], M. Lemoine-Goumard[36,37], M. Livingstone[47], F. Longo[10,11], F. Loparco[18,19], B. Lott[36,37], M. N. Lovellette[2], P. Lubrano[16,17], A. G. Lyne[38], G. M. Madejski[4], A. Makeev[2,27], R. N. Manchester[45], M. Marelli[23], M. N. Mazziotta[19], W. McConville[24,41], J. E. McEnery[24], S. McGlynn[44,7], C. Meurer[31,7], P. F. Michelson[4], T. Mineo[53], W. Mitthumsiri[4], T. Mizuno[40], A. A. Moiseev[25,41], C. Monte[18,19], M. E. Monzani[4], A. Morselli[54], I. V. Moskalenko[4], S. Murgia[4], T. Nakamori[48], P. L. Nolan[4], J. P. Norris[55], A. Noutsos[38], E. Nuss[29], T. Ohsugi[40], N. Omodei[8], E. Orlando[46], J. F. Ormes[55], M. Ozaki[56], D. Paneque[4], J. H. Panetta[4], D. Parent[36,37,1], V. Pelassa[29], M. Pepe[16,17], M. Pesce-Rollins[8], F. Piron[29], T. A. Porter[5], S. Rainò[18,19], R. Rando[13,14], S. M. Ransom[57], P. S. Ray[2], M. Razzano[8], N. Rea[58,59], A. Reimer[60,4], O. Reimer[60,4], T. Reposeur[36,37], S. Ritz[5], A. Y. Rodriguez[58], R. W. Romani[4,1], M. Roth[21], F. Ryde[44,7], H. F.-W. Sadrozinski[5], D. Sanchez[20], A. Sander[15], P. M. Saz Parkinson[5], J. D. Scargle[61], T. L. Schalk[5], A. Sellerholm[31,7], C. Sgrò[8], E. J. Siskind[62], D. A. Smith[36,37], P. D. Smith[15], G. Spandre[8], P. Spinelli[18,19], B. W. Stappers[38], J.-L. Starck[9], E. Striani[54,63], M. S. Strickman[2], A. W. Strong[46], D. J. Suson[64], H. Tajima[4], H. Takahashi[40], T. Takahashi[56], T. Tanaka[4], J. B. Thayer[4], J. G. Thayer[4], G. Theureau[28], D. J. Thompson[24], S. E. Thorsett[5], L. Tibaldo[13,9,14], O. Tibolla[65], D. F. Torres[66,58], G. Tosti[16,17], A. Tramacere[4,67], Y. Uchiyama[56,4], T. L. Usher[4], A. Van Etten[4], V. Vasileiou[24,25,26], C. Venter[24,68], N. Vilchez[51], V. Vitale[54,63], A. P. Waite[4], P. Wang[4], N. Wang[69], K. Watters[4], P. Weltevrede[45], B. L. Winer[15], K. S. Wood[2], T. Ylinen[44,70,7], M. Ziegler[5]

---

[1] Corresponding authors: G. A. Caliandro, andrea.caliandro@ba.infn.it; E. C. Ferrara, elizabeth.c.ferrara@nasa.gov; D. Parent, parent@cenbg.in2p3.fr; R. W. Romani, rwr@astro.stanford.edu.

[2] Space Science Division, Naval Research Laboratory, Washington, DC 20375, USA

[3] National Research Council Research Associate, National Academy of Sciences, Washington, DC 20001, USA

[4] W. W. Hansen Experimental Physics Laboratory, Kavli Institute for Particle Astrophysics and Cosmology, Department of Physics and SLAC National Accelerator Laboratory, Stanford University, Stanford, CA 94305, USA

[5] Santa Cruz Institute for Particle Physics, Department of Physics and Department of Astronomy and Astrophysics, University of California at Santa Cruz, Santa Cruz, CA 95064, USA

[6] Department of Astronomy, Stockholm University, SE-106 91 Stockholm, Sweden

[7] The Oskar Klein Centre for Cosmoparticle Physics, AlbaNova, SE-106 91 Stockholm, Sweden

[8] Istituto Nazionale di Fisica Nucleare, Sezione di Pisa, I-56127 Pisa, Italy

[9] Laboratoire AIM, CEA-IRFU/CNRS/Université Paris Diderot, Service d'Astrophysique, CEA Saclay, 91191 Gif sur Yvette, France

[10] Istituto Nazionale di Fisica Nucleare, Sezione di Trieste, I-34127 Trieste, Italy

[11] Dipartimento di Fisica, Università di Trieste, I-34127 Trieste, Italy

[12] Rice University, Department of Physics and Astronomy, MS-108, P. O. Box 1892, Houston, TX 77251, USA

[13] Istituto Nazionale di Fisica Nucleare, Sezione di Padova, I-35131 Padova, Italy

[14] Dipartimento di Fisica "G. Galilei", Università di Padova, I-35131 Padova, Italy

[15] Department of Physics, Center for Cosmology and Astro-Particle Physics, The Ohio State University, Columbus, OH 43210, USA

[16] Istituto Nazionale di Fisica Nucleare, Sezione di Perugia, I-06123 Perugia, Italy

[17] Dipartimento di Fisica, Università degli Studi di Perugia, I-06123 Perugia, Italy

[18] Dipartimento di Fisica "M. Merlin" dell'Università e del Politecnico di Bari, I-70126 Bari, Italy

[19] Istituto Nazionale di Fisica Nucleare, Sezione di Bari, 70126 Bari, Italy

[20] Laboratoire Leprince-Ringuet, École polytechnique, CNRS/IN2P3, Palaiseau, France

[21] Department of Physics, University of Washington, Seattle, WA 98195-1560, USA

[22] Columbia Astrophysics Laboratory, Columbia University, New York, NY 10027, USA

[23] INAF-Istituto di Astrofisica Spaziale e Fisica Cosmica, I-20133 Milano, Italy

[24] NASA Goddard Space Flight Center, Greenbelt, MD 20771, USA

[25] Center for Research and Exploration in Space Science and Technology (CRESST), NASA Goddard Space Flight Center, Greenbelt, MD 20771, USA

[26] University of Maryland, Baltimore County, Baltimore, MD 21250, USA

[27] George Mason University, Fairfax, VA 22030, USA

[28] Laboratoire de Physique et Chemie de l'Environnement, LPCE UMR 6115 CNRS, F-45071 Orléans Cedex 02,

---

and Station de radioastronomie de Nançay, Observatoire de Paris, CNRS/INSU, F-18330 Nançay, France

[29]Laboratoire de Physique Théorique et Astroparticules, Université Montpellier 2, CNRS/IN2P3, Montpellier, France

[30]Department of Physics and Astronomy, Sonoma State University, Rohnert Park, CA 94928-3609, USA

[31]Department of Physics, Stockholm University, AlbaNova, SE-106 91 Stockholm, Sweden

[32]Royal Swedish Academy of Sciences Research Fellow, funded by a grant from the K. A. Wallenberg Foundation

[33]Agenzia Spaziale Italiana (ASI) Science Data Center, I-00044 Frascati (Roma), Italy

[34]Dipartimento di Fisica, Università di Udine and Istituto Nazionale di Fisica Nucleare, Sezione di Trieste, Gruppo Collegato di Udine, I-33100 Udine, Italy

[35]Istituto Universitario di Studi Superiori (IUSS), I-27100 Pavia, Italy

[36]Université de Bordeaux, Centre d'Études Nucléaires Bordeaux Gradignan, UMR 5797, Gradignan, 33175, France

[37]CNRS/IN2P3, Centre d'Études Nucléaires Bordeaux Gradignan, UMR 5797, Gradignan, 33175, France

[38]Jodrell Bank Centre for Astrophysics, School of Physics and Astronomy, The University of Manchester, M13 9PL, UK

[39]Arecibo Observatory, Arecibo, Puerto Rico 00612, USA

[40]Department of Physical Sciences, Hiroshima University, Higashi-Hiroshima, Hiroshima 739-8526, Japan

[41]University of Maryland, College Park, MD 20742, USA

[42]Istituto Nazionale di Fisica Nucleare, Sezione di Trieste, and Università di Trieste, I-34127 Trieste, Italy

[43]University of Alabama in Huntsville, Huntsville, AL 35899, USA

[44]Department of Physics, Royal Institute of Technology (KTH), AlbaNova, SE-106 91 Stockholm, Sweden

[45]Australia Telescope National Facility, CSIRO, Epping NSW 1710, Australia

[46]Max-Planck Institut für extraterrestrische Physik, 85748 Garching, Germany

[47]Department of Physics, McGill University, Montreal, PQ, Canada H3A 2T8

[48]Department of Physics, Tokyo Institute of Technology, Meguro City, Tokyo 152-8551, Japan

[49]Waseda University, 1-104 Totsukamachi, Shinjuku-ku, Tokyo, 169-8050, Japan

[50]Cosmic Radiation Laboratory, Institute of Physical and Chemical Research (RIKEN), Wako, Saitama 351-0198, Japan

[51]Centre d'Étude Spatiale des Rayonnements, CNRS/UPS, BP 44346, F-30128 Toulouse Cedex 4, France

[52]Max-Planck-Institut für Radioastronomie, Auf dem Hügel 69, 53121 Bonn, Germany

[53]IASF Palermo, 90146 Palermo, Italy

[54]Istituto Nazionale di Fisica Nucleare, Sezione di Roma "Tor Vergata", I-00133 Roma, Italy

[55]Department of Physics and Astronomy, University of Denver, Denver, CO 80208, USA

[56]Institute of Space and Astronautical Science, JAXA, 3-1-1 Yoshinodai, Sagamihara, Kanagawa 229-8510, Japan

[57]National Radio Astronomy Observatory (NRAO), Charlottesville, VA 22903, USA

ABSTRACT

The dramatic increase in the number of known gamma-ray pulsars since the launch of the *Fermi Gamma-ray Space Telescope* (formerly GLAST) offers the first opportunity to study a sizable population of these high-energy objects. This catalog summarizes 46 high-confidence pulsed detections using the first six months of data taken by the Large Area Telescope (LAT), *Fermi*'s main instrument. Sixteen previously unknown pulsars were discovered by searching for pulsed signals at the positions of bright gamma-ray sources seen with the LAT, or at the positions of objects suspected to be neutron stars based on observations at other wavelengths. The dimmest observed flux among these gamma-ray-selected pulsars is 6.0×10^{-8} ph cm^{-2} s^{-1} (for E >100 MeV). Pulsed gamma-ray emission was discovered from twenty-four known pulsars by using ephemerides (timing solutions) derived from monitoring radio pulsars. Eight of these new gamma-ray pulsars are millisecond pulsars. The dimmest observed flux among the radio-selected pulsars is 1.4×10^{-8} ph cm^{-2} s^{-1} (for E >100 MeV). The remaining six gamma-ray pulsars were known since the *Compton Gamma Ray Observatory* mission, or before. The limiting flux for pulse detection is non-uniform over the sky owing to different background levels, especially near the Galactic plane. The pulsed energy spectra can be described by a power law with an exponential cutoff, with cutoff energies in the range $\sim 1-5$ GeV. The rotational energy loss rate ($\dot{E}$) of these neutron stars spans 5 decades, from $\sim 3 \times 10^{33}$ erg s^{-1} to 5×10^{38} erg s^{-1}, and the apparent efficiencies for conversion to gamma-ray emission range from $\sim$ 0.1% to $\sim$ unity, although distance uncertainties complicate efficiency estimates. The pulse shapes show substantial

---

[58] Institut de Ciencies de l'Espai (IEEC-CSIC), Campus UAB, 08193 Barcelona, Spain

[59] Sterrenkundig Institut "Anton Pannekoek", 1098 SJ Amsterdam, Netherlands

[60] Institut für Astro- und Teilchenphysik and Institut für Theoretische Physik, Leopold-Franzens-Universität Innsbruck, A-6020 Innsbruck, Austria

[61] Space Sciences Division, NASA Ames Research Center, Moffett Field, CA 94035-1000, USA

[62] NYCB Real-Time Computing Inc., Lattingtown, NY 11560-1025, USA

[63] Dipartimento di Fisica, Università di Roma "Tor Vergata", I-00133 Roma, Italy

[64] Department of Chemistry and Physics, Purdue University Calumet, Hammond, IN 46323-2094, USA

[65] Max-Planck-Institut für Kernphysik, D-69029 Heidelberg, Germany

[66] Institució Catalana de Recerca i Estudis Avançats, Barcelona, Spain

[67] Consorzio Interuniversitario per la Fisica Spaziale (CIFS), I-10133 Torino, Italy

[68] North-West University, Potchefstroom Campus, Potchefstroom 2520, South Africa

[69] National Astronomical Observatories-CAS, Ürümqi 830011, China

[70] School of Pure and Applied Natural Sciences, University of Kalmar, SE-391 82 Kalmar, Sweden

diversity, but roughly 75% of the gamma-ray pulse profiles have two peaks, separated by $\gtrsim 0.2$ of rotational phase. For most of the pulsars, gamma-ray emission appears to come mainly from the outer magnetosphere, while polar-cap emission remains plausible for a remaining few. Spatial associations imply that many of these pulsars power pulsar wind nebulae. Finally, these discoveries suggest that gamma-ray-selected young pulsars are born at a rate comparable to that of their radio-selected cousins and that the birthrate of all young gamma-ray-detected pulsars is a substantial fraction of the expected Galactic supernova rate.

Subject headings: catalogs – gamma rays: observations – pulsars: general – stars: neutron

Version corrected for an Erratum sent to the Ap J, December 2010: In the original paper, an error was made in accounting for the delay due to interstellar dispersion in the radio phasing of PSR J1124−5916. This changes the measured gamma-ray to radio lag (δ) to 0.11 ± 0.01. An error was also made in the off-pulse phase range in Table 3 for that pulsar. This error did not affect the spectral results. Corrected versions of Table 3 (with the revised numbers in bold face), Figure 4, and Figure A20 are included here. In addition there was an error in the caption to Figure 9. The figure with corrected caption is included here, with the changed word in bold face.

1. Introduction

Following the 1967 discovery of pulsars by Bell and Hewish (Hewish et al. 1968), Gold (1968) and Pacini (1968) identified these objects as rapidly rotating neutron stars whose observable emission is powered by the slow-down of the rotation. With their strong electric, magnetic, and gravitational fields, pulsars offer an opportunity to study physics under extreme conditions. As endpoints of stellar evolution, these neutron stars, together with their associated supernova remnants (SNRs) and pulsar wind nebulae (PWNe), help probe the life cycles of stars.

Over 1800 rotation-powered pulsars are now listed in the ATNF pulsar catalog (Manchester et al. 2005)[1], as illustrated in Figure 1. The vast majority of these pulsars were discovered by radio telescopes. Small numbers of pulsars have also been seen in the optical band, with more in the X-ray bands (see e.g. Becker 2009).

In the high-energy gamma-ray domain ($\geq$ 30 MeV) the first indications for pulsar emission were obtained for the Crab pulsar by balloon-borne detectors (e.g. Browning et al. 1971), and confirmed by the SAS-2 satellite (Kniffen et al. 1974), which also found gamma radiation from the Vela pulsar (Thompson et al. 1975). The *COS-B* satellite provided additional details about these two gamma-ray pulsars, including a confirmation that the Vela pulsar gamma-ray emission was not in phase with the radio nor did it have the same emission pattern (light curve) as seen in the radio (see e.g. Kanbach et al. 1980).

---

[1] http://www.atnf.csiro.au/research/pulsar/psrcat

The *Compton Gamma Ray Observatory* (*CGRO*) expanded the number of gamma-ray pulsars to at least seven, with six clearly seen by the *CGRO* high-energy instrument, EGRET. This gamma-ray pulsar population allowed a search for trends, such as the increase in efficiency $\eta = L_\gamma/\dot{E}$ with decreasing values of the open field line voltage of the pulsar, first noted by Arons (1996), for gamma-ray luminosity L_γ and spin-down luminosity $\dot{E}$. A summary of gamma-ray pulsar results in the *CGRO* era is given by Thompson (2004).

The third EGRET catalog (3EG; Hartman et al. 1999) included 271 sources of which ∼170 remained unidentified. Determining the nature of these unidentified sources is one of the outstanding problems in high-energy astrophysics. Many of them are at high Galactic latitude and are most likely active galactic nuclei or blazars. However, most of the sources at low Galactic latitudes ($|b| \leq 5^\circ$) are associated with star-forming regions and hence may be pulsars, PWNe, SNRs, winds from massive stars, or high-mass X-ray binaries (e.g. Kaaret & Cottam 1996; Yadigaroglu & Romani 1997; Romero et al. 1999). A number of radio pulsars were subsequently discovered in EGRET error boxes (e.g. Kramer et al. 2003), but gamma-ray pulsations in the archival EGRET data were never clearly seen. Solving the puzzle of the unidentified sources will constrain pulsar emission models: pulsar population synthesis studies, such as those by Cheng & Zhang (1998), Gonthier et al. (2002), and McLaughlin & Cordes (2000), indicate that the number of detectable pulsars in either EGRET or *Fermi* data, as well as the expected ratio of radio-loud and radio-quiet pulsars (Harding et al. 2007), strongly depends on the assumed emission model.

The Large Area Telescope (LAT) on the *Fermi Gamma-ray Space Telescope* has provided a major increase in the known gamma-ray pulsar population, including pulsars discovered first in gamma-rays (Abdo et al. 2009c) and millisecond pulsars (MSPs) (Abdo et al. 2009b). The first aim of this paper is to summarize the properties of the gamma-ray pulsars detected by *Fermi*-LAT during its first six months of data taking. The second primary goal is to use this gamma-ray pulsar catalog to address astrophysical questions such as:

1. Are all the gamma-ray pulsars consistent with one type of emission model?
2. How do the gamma-ray pulsars compare to the radio pulsars in terms of physical properties such as age, magnetic field, spin-down luminosity, and other parameters?
3. Are the trends suggested by the *CGRO* pulsars confirmed by the LAT gamma-ray pulsars?
4. Which of the LAT pulsars are associated with SNRs, PWNe, unidentified EGRET sources, or TeV sources?

The structure of this paper is as follows: Section 2 describes the LAT and the pulsar data analysis procedures; Section 3 presents the catalog and derives some population statistics from our sample; Section 4 studies the LAT sensitivity for gamma-ray pulsar detection, while in Section 5 the implications of our results are briefly discussed. Finally, our conclusions are summarized in Section 6.

2. Observations and Analysis

The *Fermi Gamma-ray Space Telescope* was successfully launched on 2008 June 11, carrying two gamma-ray instruments: the LAT and the Gamma-ray Burst Monitor (GBM). The LAT, *Fermi*'s main instrument, is described in detail in Atwood et al. (2009), with early on-orbit performance reported in Abdo et al. (2009o). It is a pair-production telescope composed of a 4×4 grid of towers. Each tower consists of a silicon-strip detector and a tungsten-foil tracker/converter, mated with a hodoscopic cesium-iodide calorimeter. This grid of towers is covered by a segmented plastic scintillator anti-coincidence detector. The LAT is sensitive to gamma rays with energies in the range from 20 MeV to greater than 300 GeV, and its on-axis effective area is ~ 8000 cm^2 for $E > 1$ GeV. The gamma-ray point spread function (PSF) is energy dependent, and 68% of photons have reconstructed directions within $\theta_{68} \simeq 0\overset{\circ}{.}8E^{-0.8}$ of a point source, with E in GeV, leveling off to $\theta_{68} \lesssim 0\overset{\circ}{.}1$ for $E > 10$ GeV . Effective area, PSF, and energy resolution are tabulated into bins of photon energy and angle of incidence relative to the LAT axis. The tables are called "instrument response functions, and are described in detail in Abdo et al. (2009o). This work uses the version called `P6_v3_diffuse`.

Gamma-ray events recorded with the LAT have time stamps that are derived from a GPS-synchronized clock on board the *Fermi* satellite. The accuracy of the time stamps relative to UTC is < 1 μs (Abdo et al. 2009o). The timing chain from the GPS-based satellite clock through the barycentering and epoch folding software has been shown to be accurate to better than a few μs for binary orbits, and significantly better for isolated pulsars (Smith et al. 2008).

The LAT field-of-view is about 2.4 sr. Nearly the entire first year in orbit has been dedicated to an all-sky survey, imaging the entire sky every two orbits, i.e. every 3 hours. Any given point on the sky is observed roughly $1/6^{\mathrm{th}}$ of the time. The LAT's large effective area and excellent source localization coupled with improved cosmic-ray rejection led to the detection of 46 gamma-ray pulsars in the first six months of LAT observations. These include the six gamma-ray pulsars clearly seen with EGRET (Thompson 2004), two young pulsars seen marginally with EGRET (Ramanamurthy et al. 1996; Kaspi et al. 2000), the MSP seen marginally with EGRET (Kuiper et al. 2000), PSR J2021+3651 discovered in gamma-rays by *AGILE* (Halpern et al. 2008), and some of the other pulsars also studied by *AGILE* (Pellizzoni et al. 2009).

During the LAT commissioning period, several configuration settings were tested that affected the LAT energy resolution and reconstruction. However, these changes had no effect on the LAT timing. Therefore, for the spectral analyses, the data were collected from the start of the *Fermi* sky-survey observations (2008 August 4, shortly before the end of the commissioning period) until

2009 February 1, while the light curve and periodicity test analysis starts from the first events recorded by the LAT after launch (2008 June 25) and also extends through 2009 February 1.

s

2.1. Timing Analysis

We have conducted two distinct pulsation searches of *Fermi* LAT data. One search uses the ephemerides of known pulsars, obtained from radio and X-ray observations. The other method searches for periodicity in the arrival times of gamma-rays coming from the direction of neutron star candidates ("blind period searches"). Both search strategies have advantages. The former is sensitive to lower gamma-ray fluxes, and the comparison of phase-aligned pulse profiles at different wavelengths is a powerful diagnostic of beam geometry. The blind period search allows for the discovery of new pulsars with selection biases different from those of radio searches, such as, for example, favoring pulsars with a broader range of inclinations between the rotation and magnetic axes.

For each gamma-ray event (index i), the topocentric gamma-ray arrival time recorded by the LAT is transferred to times at the solar-system barycenter t_i by correcting for the position of *Fermi* in the solar-system frame. The rotation phase $\phi_i(t_i)$ of the neutron star is calculated from a timing model, such as a truncated Taylor series expansion,

$$\phi_i(t_i) = \phi_0 + \sum_{j=0}^{j=N} \frac{f_j \times (t_i - T_0)^{j+1}}{(j+1)!}. \tag{1}$$

Here, T_0 is the reference epoch of the pulsar ephemeris and ϕ_0 is the pulsar phase at $t = T_0$. The coefficients f_j are the rotation frequency derivatives of order j. The rotation period is $P = 1/f_0$. Different timing models, described in detail in Edwards et al. (2006), can take into account various physical effects. Most germane to the present work is accurate $\phi_i(t_i)$ computations, even in the presence of the rotational instabilities of the neutron star called "timing noise". "Phase-folding" a light curve, or pulse profile, means filling a histogram with the fractional part of the ϕ_i values. An ephemeris includes the pulsar coordinates necessary for barycentering, the f_j and T_0 values, and may include parameters describing the pulsar proper motion, glitch epochs, and more. The radio dispersion measure (DM) is used to extrapolate the radio pulse arrival time to infinite frequency, and uncertainties in the DM translate to an uncertainty in the phase offset between the radio and gamma-ray peaks.

2.1.1. Pulsars with Known Rotation Ephemerides

The ATNF database (version 1.36, Manchester et al. 2005) lists 1826 pulsars, and more have been discovered and await publication (Figure 1). The LAT observes them continuously during the all-sky survey. Phase-folding the gamma rays coming from the positions of all of these pulsars (consistent with the energy-dependent LAT PSF) requires only modest computational resources. However, the best candidates for gamma-ray emission are the pulsars with high $\dot{E}$, which often have substantial timing noise. Ephemerides accurate enough to allow phase-folding into, at a minimum, 25-bin phase histograms can degrade within days to months. The challenge is to have *contemporaneous* ephemerides.

We have obtained 762 contemporaneous pulsar ephemerides from radio observatories, and 5 from X-ray telescopes, in two distinct groups. The first consists of 218 pulsars with high spin-down power ($\dot{E} > 10^{34}$ erg s^{-1}) timed regularly as part of a campaign by a consortium of astronomers for the *Fermi* mission, as described in Smith et al. (2008). With one exception (PSR J1124−5916, which is a faint radio source with large timing noise), all of the 218 targets of the campaign have been monitored since shortly before *Fermi* launch. Some results from the timing campaign can be found in Weltevrede et al. (2009).

The second group is a sample of 544 pulsars from nearly the entire $P - \dot{P}$ plane (Figure 2) being timed for other purposes for which ephemerides were shared with the LAT team. These pulsars reduce possible bias of the LAT pulsar searches created by our focus on the high $\dot{E}$ sample requiring frequent monitoring. Gamma-ray pulsations from six radio pulsars with $\dot{E} < 10^{34}$ erg s^{-1} were discovered in this manner, all of which are MSPs.

Table 1 lists properties of the 46 detected gamma-ray pulsars. Five of the 46 pulsars, all MSPs, are in binary systems. The period first derivative $\dot{P}$ is corrected for the kinematic Shklovskii effect (Shklovskii 1970): $\dot{P} = \dot{P}_{\rm obs} - \mu^2 P_{\rm obs} d/c$, where μ is the pulsar proper motion, and d the distance. The correction is small except for a few MSPs (Abdo et al. 2009b). The characteristic age is $\tau_{\rm c} = P/2\dot{P}$ and the spin-down luminosity is

$$\dot{E} = 4\pi^2 I \dot{P} P^{-3}, \tag{2}$$

taking the neutron star's moment of inertia I to be 10^{45}g cm^2. The magnetic field at the light cylinder (radius $R_{\rm LC} = cP/2\pi$) is

$$B_{\rm LC} = \left(\frac{3I8\pi^4 \dot{P}}{c^3 P^5} \right)^{1/2} \approx 2.94 \times 10^8 (\dot{P} P^{-5})^{1/2}\,{\rm G}. \tag{3}$$

Table 2 lists which observatories provided ephemerides for the gamma-ray pulsars. An “L” indicates that the pulsar was timed using LAT gamma rays, as described in the next Section.

“P” is the Parkes radio telescope (Manchester 2008; Weltevrede et al. 2009). The majority of the Parkes observations were carried out at intervals of 4 – 6 weeks using the 20 cm Multibeam receiver (Staveley-Smith et al. 1996) with a 256 MHz band centered at 1369 MHz. At 6 month intervals observations were also made at frequencies near 0.7 and 3.1 GHz with bandwidths of 32 and 1024 MHz respectively. The required frequency resolution to avoid dispersive smearing across the band was provided by a digital spectrometer system.

"N" is the Nançay radio telescope (Theureau et al. 2005). Nançay observations are carried out every three weeks on average. The recent version of the BON backend is a GPU-based coherent dedispersor allowing the processing of a 128 MHz bandwidth over two complex polarizations (Cognard et al. 2009). The majority of the data are collected at 1398 MHz, while for MSPs in particular, observations are duplicated at 2048 MHz to allow DM monitoring.

"J" is the 76-m Lovell radio telescope at Jodrell Bank in the United Kingdom. Jodrell Bank observations (Hobbs et al. 2004) were carried out at typical intervals of between 2 days and 10 days in a 64-MHz band centered on 1404 MHz, using an analog filterbank to provide the frequency resolution required to remove interstellar dispersive broadening. Occasionally, observations are also carried out in a band centered on 610 MHz to monitor the interstellar dispersion delay.

"G" is the 100-m NRAO Green Bank Telescope (GBT). PSR J1833–1034 was observed monthly at 0.8 GHz with a bandwidth of 48 MHz using the BCPM filter bank (Backer et al. 1997). The other pulsars monitored at the GBT were observed every two weeks at a frequency of 2 GHz across a 600 MHz band with the Spigot spectrometer (Kaplan et al. 2005). Individual integration times ranged between 5 minutes and 1 hour.

Arecibo ("A") observations of the very faint PSRs J1930+1852 and J2021+3651 are carried out every two weeks, with the L-wide receiver (1100 to 1730 MHz). The back-ends used are the Wideband Arecibo Pulsar Processor (WAPP) correlators (Dowd et al. 2000), each with a 100 MHz-wide band. The antenna voltages are 3-level digitized and then auto-correlated with a total of 512 lags, accumulated every 128 μs, and written to disk as 16-bit sums. Processing includes Fourier-transforms to obtain power spectra, which are then dedispersed and phase-folded. The average pulse profiles are cross-correlated with a low-noise template profile to obtain topocentric times of arrival.

"W" is the Westerbork Synthesis Radio Telescope, with which observations were made approximately monthly at central frequencies of 328, 382 and 1380 MHz with bandwidths of 10 MHz at the lower frequencies and 80 MHz at the higher frequencies. The PuMa pulsar backend (Voûte et al. 2002) was used to record all the observations. Folding and dedispersion were performed offline.

The rms of the radio timing residuals for most of the solutions used in this paper is $< 0.5\%$ of a rotation period, but ranges as high as 1.2% for five pulsars. This is adequate for the 50- or 25-bin phase histograms used in this paper. The ephemerides used for this catalog will be available on the *Fermi* Science Support Center data servers[2].

---

[2] http://fermi.gsfc.nasa.gov/ssc/

2.1.2. Pulsars Discovered in Blind Periodicity Searches

For all 16 of the pulsars found in the blind searches of the LAT data, we determined the timing ephemerides used in this catalog directly from the LAT data as described below. In addition, for two other pulsars the LAT data provided the best available timing model. The first is the radio-quiet pulsar Geminga. Since Geminga is such a bright gamma-ray pulsar, it is best timed directly using gamma-ray observations. During the period between EGRET and *Fermi*, occasional *XMM-Newton* observations maintained the timing model (Jackson & Halpern 2005) but a substantially improved ephemeris has now been derived from the LAT data (Abdo et al. 2009a). The second is PSR J1124−5916, which is extremely faint in the radio (see Table 1) and exhibits a large amount of timing noise (Camilo et al. 2002c). In this Section, we briefly describe the blind pulsar searches and how the timing models for these pulsars are created. These pulsars have an "L" in the "ObsID" column of Table 2.

Even though L_γ of a young pulsar can be several percent of $\dot{E}$, the gamma-ray counting rates are low. As an example, the LAT detects a gamma ray from the Crab pulsar approximately every 500 rotations, when the Crab is well within the LAT's field-of-view. Such sparse photon arrivals make periodicity searches difficult. Extensive searches for pulsations performed on EGRET data (Chandler et al. 2001; Ziegler et al. 2008) were just sensitive enough to detect the very bright pulsars Vela, Crab, and Geminga in a blind search, had they not already been known as pulsars. Blind periodicity searches of all other EGRET sources proved fruitless.

By contrast, the improvements afforded by the LAT have enabled highly successful blind searches for pulsars. In the first six months of operation, we discovered a total of 16 new pulsars in direct pulsation searches of the LAT data (see e.g. Abdo et al. 2008, 2009c). A computationally efficient time-difference search technique made these searches possible (Atwood et al. 2006), enabling searches of hundreds of *Fermi* sources to be performed on a small computer cluster with only a modest loss in sensitivity compared to fully coherent search techniques. Still, owing to the large number of frequency and frequency derivative trials required to search a broad parameter space, the minimum gamma-ray flux needed for a statistically significant detection is considerably higher than the minimum flux needed for the phase-folding technique using a known ephemeris (as in Section 2.1, Eq. 1).

We performed these blind searches on ~ 100 candidate sources identified before launch and on another ~ 200 newly detected LAT sources. The parameter space covered by the blind searches included frequencies from 0.5 Hz to 64 Hz (periods of 156.25 ms to 2 s), and a frequency derivative from zero to the spin-down of the young Crab pulsar ($f_1 = -3.7 \times 10^{-10}$), which covers $\sim 86\%$ of the pulsars contained in the ATNF database (Abdo et al. 2009c). Of the 16 pulsars detected in these searches, 13 are associated with previously known EGRET sources. The discoveries include several long-suspected pulsars in SNRs and PWNe.

These 16 pulsars are gamma-ray selected, as they were discovered by the LAT and thus the population is subject to very different selection effects than the general radio pulsar population.

However, this does not necessarily imply that they are radio quiet. For several cases, deep radio searches have already been performed on known PWNe or X-ray point sources suspected of harboring pulsars. In most cases, new radios searches are required to investigate whether there is a radio pulsar counterpart down to a meaningful luminosity limit. These searches are now being undertaken and are yielding the first results (Camilo et al. 2009).

For these 18 pulsars (16 new plus Geminga and PSR J1124−5916), we derived timing models from the LAT data using the procedure summarized here. A more detailed description of pulsar timing using LAT data can be found in Ray et al. (2010).

The LAT timing analysis starts from the first events recorded by the LAT after launch (2008 June 25) and extends through about 2009 May 1. During the commissioning period, several configuration settings were tested that affected the LAT energy resolution and reconstruction. However, these changes had no effect on the LAT timing. We selected photons from a small radius of interest (ROI) around the pulsar of $< 0.5^\circ$ or $< 1^\circ$ (see further Section 2.1.3 and Table 2). For this pulsar timing analysis, we used *diffuse* class photons with energies above a cutoff (typically $E > 300$ MeV) selected to optimize the signal-to-noise ratio for that particular pulsar. We converted the photon arrival times to the geocenter using the GTBARY science tool[2]. This correction removes the effects of the spacecraft motion about the Earth, resulting in times as would be observed by a virtual observatory at the geocenter.

Using an initial timing model for the pulsar, we then used TEMPO2 (Hobbs et al. 2006) in its predictive mode to generate polynomial coefficients describing the pulse phase as a function of time for an observatory at the geocenter. Using these predicted phases, we produced folded pulse profiles over segments of the LAT observation. The length of the segments depends on the brightness of the pulsar but are typically 10–20 days. We then produced a pulse time of arrival (TOA) for each data segment by Fourier domain cross-correlation with a template profile (Taylor 1992). The template profile for most of the pulsars is based on a multi-Gaussian fit to the observed LAT pulse profile. However, in the case of Geminga, which has very high signal-to-noise and a complex profile not well described by a small number of Gaussians, we used a template profile that was the full mission light curve itself.

Finally, we used TEMPO2 to fit a timing model to each pulsar. For most of the pulsars, the model includes pulsar celestial coordinates, frequency and frequency derivative. In several cases, the fit also required a frequency second derivative term to account for timing noise. In the case of PSR J1124−5916, we required three sinusoidal terms (Hobbs et al. 2006) to model the effects of the strong timing noise in this source. Two pulsars (J1741−2054 and J1809−2332) have positions too close to the ecliptic plane for the Declination to be well-constrained by pulsar timing and thus we fixed the positions based on X-ray observations of the presumed counterparts[3]. For Geminga and PSR J1124−5916 we also used known, fixed positions (Caraveo et al. 1998; Faherty et al. 2007; Camilo et al. 2002c) because they were of much higher precision than could be determined from less than one year of *Fermi* timing. The rms of the timing residuals are between 0.5 and 2.9% of a rotation period, with the highest being for PSR J1459−60. The TEMPO2 timing models used for the catalog analysis will be made available online at the FSSC web site[2].

---

[3] Pulsar timing positions are measured by fitting the sinusoidal delays of the pulse arrival times associated with the Earth moving along its orbit. For pulsars very close to the ecliptic plane the derivative of this delay with respect to

2.1.3. Light Curves

The light curves of 46 gamma-ray pulsars detected by the LAT are appended to the end of this paper, in Figures A-1 to A-46. The gray light curve in the top panel includes all photons with $E > 0.1$ GeV, while the other panels show the profiles in exclusive energy ranges: $E > 1.0$ GeV (with $E > 3.0$ GeV in black) in the second panel from the top; 0.3 to 1.0 GeV in the next panel; and 0.1 to 0.3 GeV in the fourth panel. Phase-aligned radio profiles for the radio-selected pulsars are in the bottom panel. The light curves are plotted with $N = 25$ or 50 bins, with 25 bins used when required to keep at least 50 counts per bin in the peak of the light curve or to prevent undue smearing due to the accuracy of the timing model.

Table 3 lists light curve parameters, taken from the > 100 MeV profiles (top panel of Figures A-1–A-46). For some pulsars (e.g. PSR J1420−6048) the peak multiplicity is unclear: the data are consistent with both a single, broad peak and with two closely spaced narrow peaks. For the Crab (PSR J0534+2200) the phase offset of the first gamma-ray peak is relative to radio "precursor" peak, not visible in Figure A-8.

Table 2 lists the Z_2^2 (Buccheri et al. 1983) and H (de Jager et al. 1989) periodicity test values for $E > 0.3$ GeV. Only one trial is made for each pulsar, and the significance calculations do not take into account the trials factor for the ~ 800 pulsars searched. Detection of gamma-ray pulsations are claimed when the significance of the periodicity test exceeds 5σ (i.e. a chance probability of $< 6 \times 10^{-7}$). We have used the Z-test with $m = 2$ harmonics (Z_2^2) which provides an analytical distribution function for the null hypothesis described by a χ^2 distribution with $2m$ degrees of freedom. The H-test uses Monte-Carlo simulations to calculate probabilities, limited to a minimum of 4×10^{-8} (equivalent to 5.37σ). Each method is sensitive to different pulse profile shapes. Four pulsars in the catalog fall short of the 5σ significance threshold in the six-month data set with the selection cuts applied here: the 3 MSPs J0218+4232, J0751+1807, and J1744−1134 reported in Abdo et al. (2009b), and the radio pulsar PSR J2043+2740. The characteristic pulse shape as well as the trend of the significance versus time lead us to include these four in the catalog.

Table 2 also lists "maxROI", the maximum angular radius around the pulsar position within which gamma-ray events were kept, generally $1^\circ\!.0$, but $0^\circ\!.5$ in some cases. The choice was made

---

ecliptic latitude is greatly reduced and thus such pulsars have one spatial dimension poorly constrained, as discussed in Ray et al. (2010).

by using the energy spectrum for the phase-averaged source, described in Section 2.2, to maximize S^2/N over a grid of maximum radii and minimum energy thresholds (where S is the number of counts attributed to the point source, and N is the number of counts due to the diffuse background and neighboring sources). We selected photons within a radius θ_{68} of the pulsar position, requiring a radius of at least $0\overset{\circ}{.}35$, but no larger than the reported maxROI.

We estimated the background level represented by the dashed horizontal lines in Figures A-1 to A-46 from an annulus between $1^\circ < \theta < 2^\circ$ surrounding the source. Nearby sources were removed, and we normalized to the same solid angle as the source ROI. The poor spatial resolution of the LAT at low energies can blur structured diffuse emission and bias this background estimate. The levels shown are intended only to guide the eye. Detailed analyses of off-pulse emission will be discussed in future work.

2.2. Spectral Analysis

The pulsar spectra were fitted with an exponentially cutoff power-law model of the form

$$\frac{\mathrm{d}N}{\mathrm{d}E} = K E_{\mathrm{GeV}}^{-\Gamma} \exp\left(-\frac{E}{E_{\mathrm{cutoff}}}\right) \tag{4}$$

in which the three parameters are the photon index at low energy Γ, the cutoff energy E_{cutoff}, and a normalization factor K (in units of ph cm^{-2} s^{-1} MeV^{-1}), in keeping with the observed spectral shape of bright pulsars (Abdo et al. 2009g). The energy at which the normalization factor K is defined is arbitrary. We chose 1 GeV because it is, for most pulsars, close to the energy at which the relative uncertainty on the differential flux is minimal.

We wish to extract the spectra down to 100 MeV in order to constrain the power-law part of the spectrum, and to measure the flux above 100 MeV directly. Because the spatial resolution of *Fermi* is not very good at low energies ($\sim 5^\circ$ at 100 MeV), we need to account for all neighboring sources and the diffuse emission together with each pulsar. This was done using the framework used for the LAT Bright Source List (Abdo et al. 2009i). A 6-month source list was generated in the same way as the 3-month source list described in Abdo et al. (2009i), but covering the extended period of time used for the pulsar analysis. We have added the source Cyg X-3 (Abdo et al. 2009l), although it was not detected automatically as a separate source, because it is very close to PSR J2032+4127, and impacts the spectral fit of the pulsar. Cyg X-3 was fit with a simple power-law as were all other non-pulsar sources in the list.

We used a Galactic diffuse model designated `54_77Xvarh7S` calculated using GALPROP[4], an evolution of that used in Abdo et al. (2009i). A similar model, `gll_iem_v02`, is publicly available[2].

We kept events with $E > 100$ MeV belonging to the *diffuse* event class, which has the tightest cosmic-ray background rejection (Atwood et al. 2009). To avoid contamination by gamma-rays produced by cosmic-ray interactions in the Earth's atmosphere, we select time intervals when the entire ROI, of radius 10° around the source, has a zenith angle $< 105°$. We extracted events in a circle of radius 10° around each pulsar, and included all sources up to 17° into the model (sources outside the extraction region can contribute at low energy). Sources further away than 3° from the pulsar were assigned fixed spectra, taken from the all-sky analysis. Spectral parameters for the pulsar and sources within 3° of it were left free for the analysis.

---

[4] http://galprop.stanford.edu/

The fit was performed by maximizing unbinned likelihood (direction and energy of each event is considered) as described in Abdo et al. (2009i) and using the MINUIT fitting engine[5]. The uncertainties on the parameters were estimated from the quadratic development of the log(likelihood) surface around the best fit. In addition to the index Γ and the cutoff energy $E_{\rm cutoff}$ which are explicit parameters of the fit, the important physical quantities are the photon flux F_{100} (in units of ph cm^{-2} s^{-1}) and the energy flux G_{100} (in units of erg cm^{-2} s^{-1}),

$$F_{100} = \int_{100\,\rm MeV}^{100\,\rm GeV} \frac{{\rm d}N}{{\rm d}E}{\rm d}E, \text{ and} \tag{5}$$

$$G_{100} = \int_{100\,\rm MeV}^{100\,\rm GeV} E\frac{{\rm d}N}{{\rm d}E}{\rm d}E. \tag{6}$$

These derived quantities are obtained from the primary fit parameters. Their statistical uncertainties are obtained using their derivatives with respect to the primary parameters and the covariance matrix obtained from the fitting process.

For a number of pulsars, an exponentially cutoff power-law spectral model is not significantly better than a simple power-law. We identified these by computing $TS_{\rm cutoff} = 2\Delta\log(\text{likelihood})$ (comparable to a χ^2 distribution with one degree of freedom) between the models with and without the cutoff. Pulsars with $TS_{\rm cutoff} < 10$ have poorly measured cutoff energies. $TS_{\rm cutoff}$ is reported in Table 4.

The above analysis yields a fit to the overall spectrum, including both the pulsar and any unpulsed emission, such as from a PWN. To do better we split the data into on-pulse and off-pulse samples and modeled the off-pulse spectrum by a simple power-law. The off-pulse window used for this background estimation is defined in the last column of Table 3.

In a second step we re-fitted the on-pulse emission to the exponentially cutoff power-law as before, with the off-pulse emission (scaled to the on-pulse phase interval) added to the model and fixed to the off-pulse result. In many cases the off-pulse emission was not significant at the 5σ or even 3σ level, but we kept the formal best fit anyway, in order to not bias the pulsed emission upwards. The results summarized in Table 4 come from this on-pulse analysis.

Using an off-pulse pure power law is not ideal for the Crab or any other PWN with synchrotron and inverse Compton components within the *Fermi* energy range. Judging from the Crab pulsar, using a simple power-law to model the off-pulse emission mainly affects the value of the cutoff energy. The analysis specific to the Crab, with a model adapted to the pulsar synchrotron component low energies and to the high energy nebular component, yields $E_{\rm cutoff} \sim 6$ GeV (Abdo et al. 2010d). This is the value listed in Table 4. The cutoff value obtained with the simplified model applied to most pulsars in this paper is higher (> 10 GeV). The photon and energy fluxes given by the two analyses are within 10% of each other. Additional exceptions in Table 4 are for PSRs J1836+5925 and J2021+4026. The off-pulse phase definition for these pulsars is unclear, so the spectral parameters reported in the Table are from the initial, phase-averaged spectral analysis.

---

[5] http://lcgapp.cern.ch/project/cls/work-packages/mathlibs/minuit/doc/doc.html

We have checked whether our imperfect knowledge of the Galactic diffuse emission may impact the pulsar parameters by applying the same analysis with a different diffuse model, as was done in Abdo et al. (2009i). The phase-averaged emission is affected. Seven (relatively faint) pulsars see their flux move up or down by more than a factor of 1.5. On the other hand, the pulsed flux is much more robust, because the off-pulse component absorbs part of the background difference, and the source-to-background ratio is better after on-pulse phase selection. Only two pulsars see their pulsed flux move up or down by more than a factor of 1.2, and none shift by more than a factor of 1.4 when changing the diffuse model. Overall, the systematic uncertainties due to the diffuse model on the fluxes F_{100} and G_{100}, on the photon index Γ, and on $E_{\rm cutoff}$ scale with the statistical uncertainty. Adding the statistical and systematic errors in quadrature amounts, to a good approximation, to multiplying the statistical errors on F_{100}, G_{100}, and Γ by 1.2. The uncertainties listed in Table 4 and plotted in the figures include this correction. The increase in the uncertainty on $E_{\rm cutoff}$ due to the diffuse model is $< 5\%$ and is neglected.

Systematic uncertainties on the LAT effective area are of order 5% near 1 GeV, 10% below 0.1 GeV, and 20% above 10 GeV. To propagate their effect on the spectral parameters in Equation 4, we modify the instrument response functions to bracket the nominal values, and repeat the likelihood calculations. This is reported in detail for most of the individual LAT pulsars already referenced. The bias values reported in Abdo et al. (2009b) well describe our current knowledge of the effect of the uncertainties in the instrument response functions on the spectral parameters: they are $\delta\Gamma = (+0.3, -0.1)$, $\delta E_{\rm cutoff} = (+20\%, -10\%)$, $\delta F_{100} = (+30\%, -10\%)$, and $\delta G_{100} = (+20\%, -10\%)$. The bias on the integral energy flux is somewhat less than that of the integral photon flux, due to the weighting by photons in the energy range where the effective area uncertainties are smallest. We do not sum these uncertainties in quadrature with the others, since a change in instrument response will tend to shift all spectral parameters similarly.

The pulsar spectra were also evaluated using an unfolding method (D'Agostini 1995; Mazziotta 2009), that takes into account the energy dispersion introduced by the instrument response function and does not assume any model for the spectral shapes. "Unfolding" is essentially a deconvolution of the observed data from the instrument response functions. For each pulsar we selected photons within 68% of the PSF with a minimum radius of $0.^{\circ}35$ and a maximum of 5°.

The observed pulsed spectrum was built by selecting the events in the on-pulse phase interval and subtracting the events in the off-pulse interval, properly scaled for the phase ratio. The instrument response function, expressed as a smearing matrix, was evaluated using the LAT *Geant4*-based[6] Monte Carlo simulation package called *Gleam* (Boinee et al. 2003), taking into account the pointing history of the source.

The true pulsar energy spectra were then reconstructed from the observed ones using an iterative procedure based on Bayes' theorem (Mazziotta 2009). Typically, convergence is reached after a few iterations. When the procedure has converged, both statistical and systematic errors on the observed energy distribution can be easily propagated to the unfolded spectra. The results obtained from the unfolding analysis were consistent within errors with the likelihood analysis results.

3. The LAT Pulsar Sample

We describe here the astronomical context of the observed LAT pulsars, including our current best understanding of the source distances, the Galactic distribution and possible associations. We also note correlations among some observables which may help probe the origin of the pulsar emission.

3.1. Distances

Converting measured pulsar fluxes to radiated power requires reliable distance estimates. Annual trigonometric parallax measurements are the most reliable, but are generally only available for a few relatively nearby pulsars.

The most commonly used technique to obtain radio pulsar distances exploits the pulse delay as a function of wavelength by free electrons along the path to Earth. A distance can be computed from the DM coupled to an electron density distribution model. We use the NE2001 model (Cordes & Lazio 2002) unless noted otherwise. It assumes uniform electron densities in and between the Galactic spiral arms, with smooth transitions between zones, and spheres of greater density for specific regions such as the Gum nebula, or surrounding Vela. Specific lines-of-sight can traverse unmodeled regions of over- (or under-) density, as, for example, along the tangents of the spiral arms, causing significant discrepancies between the true pulsar distances and those inferred from the electron-column density.

A third method, kinematic, associates the pulsar with objects whose distance can be measured from the Doppler shift of absorption or emission lines in the neutral hydrogen (HI) spectrum, together with a rotation curve of the Galaxy. It breaks down where the velocity gradients are very small or where the distance-velocity relation has double values. The associations are often uncertain, and these distance measurements can be controversial.

---

[6] http://geant4.web.cern.ch/geant4/

In a small number of cases, the distance is evaluated either from X-ray measurements of the absorbing column at low energies (below 1 keV), or from consideration of the X-ray flux assuming some standard parameters for the neutron star.

Table 5 presents the best known distances of 37 pulsars detected by *Fermi*, the methods used to obtain them, and the references. For distances obtained from the NE2001 model and the DM, the reference indicates the DM measurement. We assume a minimum DM distance uncertainty of 30%. When distances from different methods disagree and no method is more convincing than the other, a range is given, and 30% uncertainties on the upper and lower values are used. For the remaining 9 *Fermi*-discovered pulsars no distance estimates have been established so far. Here follow comments for some of the distance values reported in Table 5:

PSR J0205+6449 – The pulsar is in the PWN 3C 58. NE2001 gives 4.5 kpc for DM=141 cm^{-3} pc in this direction (Camilo et al. 2002d). Using HI absorption and emission lines from the PWN yields from 2.6 kpc (Green & Gull 1982) to 3.2 kpc (Roberts et al. 1993). The lower V-band reddening (Fesen et al. 1988, 2008) compared to the Galactic-disk edge (Schlegel et al. 1998) suggests that the PWN is in the range 3–4 kpc. Table 5 quotes the distance range found by Green & Gull (1982) and Roberts et al. (1993).

PSR J0218+4232 – The DM measurements from Navarro et al. (1995) together with NE2001 yield 2.7 ± 0.8 kpc. Comparing the pulsar characteristic age with the cooling models of its white-dwarf companion gives a distance range of 2.5 to 4 kpc (Bassa et al. 2003).

PSR J0248+6021 – The DM of 376 cm^{-3} pc (Cognard et al. 2010) puts this pulsar beyond the edge of the Galaxy for this line-of-sight. The line-of-sight, however, borders the giant HII region W5 in the Perseus Arm. We bracket the pulsar distance as being between W5 (2 kpc) and the Galaxy edge (9 kpc).

PSR J0631+1036 – The DM = 125.3 cm^{-3} pc (Zepka et al. 1996) is large for a source in the direction of the Galactic anticenter. The dark cloud LDN 1605, part of the active star-forming region 3 Mon, is in the line-of-sight. The pulsar could be inside the cloud, at ∼0.75 kpc. Ionized material in the cloud could cause NE2001 to overestimate the distance.

PSR J1124−5916 – It lies towards the Carina arm where NE2001 biases are acute. The DM distance is 5.7 kpc (Camilo et al. 2002c). The kinematic distance of the associated SNR (G292.0+1.8) indicates a lower limit of 6.2±0.9 kpc (Gaensler & Wallace 2003). The value in Table 5 is derived by Gonzalez & Safi-Harb (2003) linking the X-ray absorption column with the extinction along the pulsar direction.

PSR J1418−6058 – This pulsar is likely associated with the PWN G313.3+0.1, near the Kookaburra complex. A nearby HII region is at 13.4 kpc (Caswell & Haynes 1987) but could easily be in the background. Such a large distance implies an unreasonably large gamma-ray efficiency. Table 5 lists a crude estimate of the distance range with the lower limit (Yadigaroglu & Romani 1997) taking the pulsar to be related to one of the near objects (Clust 3, Cl Lunga 2 or SNR G312.4−0.4), and the higher limit (Ng et al. 2005) determined by applying the relation found by Possenti et al. (2002) and the correlation between pulsar X-ray photon index and luminosity given by Gotthelf (2003).

PSR J1709–4429 – The NE2001 DM distance is 2.3±0.7 kpc (Taylor et al. 1993). Kinematic distances give upper and lower limits of 3.2±0.4 kpc and 2.4±0.6 kpc, respectively (Koribalski et al. 1995). The X-ray flux from the neutron star detected by *Chandra* (Romani et al. 2005) and *XMM-Newton* (McGowan et al. 2004) is compatible with a distance of 1.4–2.0 kpc. We assume the range 1.4–3.6 kpc.

PSR J1747–2958 – The pulsar is associated with the PWN G359.23−0.82. HI measurements yield a distance upper limit of 5.5 kpc (Uchida et al. 1992), but the DM (101 $\mathrm{pc\,cm^{-3}}$) suggests 2.0±0.6 kpc (Camilo et al. 2002b). The X-ray absorbing column detected by *Chandra* is between 4 and 5 kpc, while the closer value of 2 kpc would imply that an otherwise unknown molecular cloud lies in front of the pulsar (Gaensler et al. 2004). A range of 2–5 kpc is used in our analysis.

PSR J2021+3651 – The DM distance of ∼12 kpc implies a high gamma-ray conversion efficiency (Roberts et al. 2002; Abdo et al. 2009m). The open cluster Berkeley 87 near the line-of-sight could be responsible for an electron column density higher than modeled by NE2001. The distance in Table 5 comes from a *Chandra* X-ray observation of the pulsar and its surrounding nebula (Van Etten et al. 2008). A similar range (1.3–4.1 kpc) was obtained for the X-ray flux detected from the associated PWN.

PSR J2032+4127 – The DM value (115 pc $\mathrm{cm^{-3}}$) gives an NE2001 distance of 3.6 kpc. If the pulsar belongs to the star cluster Cyg OB2, it would be located at approximately 1.6 kpc (Camilo et al. 2009). In this text we use a range of 1.6–3.6 kpc for this source.

PSR J2229+6114 – The distance derived from the X-ray absorption is ∼3 kpc (Halpern et al. 2001b), between the values from the DM (6.5 kpc; Halpern et al. 2001a) and from the kinematic method (0.8 kpc; Kothes et al. 2001).

Figure 3 shows a polar view of the distribution of known pulsars over the Galactic plane. When two different distances are listed, we plot the closer one.

3.2. Spatial Distributions, Luminosity, and Other Pulse Properties

Figure 1 shows the pulsars projected on the sky. A Gaussian fit to the Galactic latitude distribution for those with $|b| < 10^\circ$ and having distance estimates yields a standard deviation of $\sigma_{\rm b} = 3.5 \pm 0.8$ degrees. The distances range from $d = 0.25$ to 5.6 kpc, and we can use the most distant to place an upper limit on the scale height, obtaining $h < d \sin 3\overset{\circ}{.}5 = 340$ pc, close to the typical scale height for all radio pulsars (the value used in Lyne et al. (1998) is 450 pc).

The light curve peak separations Δ and the radio lags δ from Table 3 are summarized in Figure 4. As we will discuss in Section 5, outer magnetosphere emission models predict correlations between these parameters. Figure 5 shows $B_{\rm LC}$ versus the characteristic age ($\tau_{\rm c}$). The magnetic fields at the light cylinder for the detected MSPs are comparable to those of the other gamma-ray pulsars, suggesting that the emission mechanism for the two families may be similar.

Table 4 lists L_γ and η, while Figure 6 plots L_γ vs. $\dot{E}$. The dashed line indicates $L_\gamma = \dot{E}$, while the dot-dashed line indicates $L_\gamma \propto \dot{E}^{1/2}$, where

$$L_\gamma \equiv 4\pi d^2 f_\Omega G_{100}. \tag{7}$$

The flux correction factor f_Ω (Watters et al. 2009) is model-dependent and depends on the magnetic inclination and observer angles α and ζ. Both the outer gap and slot gap models predict $f_\Omega \sim 1$, in contrast to earlier use of $f_\Omega = 1/4\pi \approx 0.08$ (in e.g. Thompson et al. 1994), or $f_\Omega = 0.5$ for MSPs (in e.g. Fierro et al. 1995). For simplicity, we use $f_\Omega = 1$ throughout the paper, which presumably induces an artificial spread in the quoted L_γ values. However, it is the quadratic distance dependence for L_γ that dominates the uncertainty in L_γ in nearly all cases.

Gamma-rays dominate the total power $L_{\rm tot}$ radiated by most known high-energy pulsars, that is, $L_{\rm tot} \approx L_\gamma$. The Crab is a notable exception, with X-ray luminosity $L_X \sim 10 L_\gamma$. In Figure 6 we plot both L_γ and $L_X + L_\gamma$. L_X for $E < 100$ MeV is taken from Figure 9 of Kuiper et al. (2001).

3.3. Associations

Table 6 provides some alternate names and positional associations of the pulsars in this catalog with other astrophysical sources. For the EGRET 3EG, EGR, and GEV and AGILE AGL catalogs, the uncertainties in the localization of the counterparts is worse than for the LAT sources. In these cases, we consider a source is a possible counterpart to a LAT pulsar when the separation between the two positions is less than the quadratic sum of their 95% confidence error radii.

We see that 25 of the 46 pulsars are associated with sources in the 3EG, EGR and GEV catalogs of EGRET sources, though 19 were seen only as unidentified unpulsed sources. A number of these unidentified EGRET sources had previously been associated with SNRs, PWNe, or other objects (e.g. Walker et al. 2003; De Becker et al. 2005). In all cases, the gamma-ray emission seen with the LAT is dominated by the pulsed emission. Of the 25 EGRET sources, 14 are gamma-ray-selected pulsars, and 11 are radio-selected, including 2 MSPs. All 6 high-confidence EGRET pulsars (Nolan et al. 1996) are detected, and the 3 marginal EGRET detections are confirmed as pulsars (Ramanamurthy et al. 1996; Kaspi et al. 2000; Kuiper et al. 2000). The 21 sources without 3EG, EGR, or GEV counterparts include 18 previously detected radio pulsars (6 of which are MSPs) and 3 gamma-ray selected pulsars.

Not surprisingly, many of the young pulsars have SNR or PWN associations. At least 19 of the 46 pulsars are associated with a PWN and/or SNR (Roberts et al. 2005; Green 2009). We do not test here whether the gamma-ray flux from any of these pulsars includes a non-magnetospheric component, as might be indicated by spatially extended emission or a spectrum at pulse minimum not characteristic of a pulsar. Such studies are underway.

At least 12 of the pulsars are associated with TeV sources, 9 of which are also associated with PWNe. Those pulsars with both TeV and PWN associations are typically young, with ages less than 20 kyr.

4. Pulsar Flux Sensitivity

In order to interpret the population of gamma-ray pulsars discovered with the LAT, we need to evaluate the sensitivity of our searches for pulsed emission. While the precise sensitivity at any location is a function of the local background flux, the pulsar spectrum, and the pulse shape, we can derive an approximate pulsed sensitivity by calculating the *unpulsed* flux sensitivity for a typical pulsar spectrum at all locations in the sky and correlating with the observed Z_2^2 test statistic for the ensemble of detected pulsars.

Figures 7 and 8 show the distributions of the cutoff energy and the photon index, respectively, for all the LAT-detected pulsars. The distribution of photon indices peaks in the range $\Gamma = 1 - 2$, and the distribution of cutoffs peaks at $E_{\rm cutoff} = 1 - 3$ GeV. For a typical spectrum, we used $\Gamma = 1.4$ and $E_{\rm cutoff} = 2.2$ GeV, values approximately equal to their respective weighted averages.

We then generated a sensitivity map for unpulsed emission for the six-month data set used here. For each *(l,b)* location in the sky, we computed the DC flux sensitivity at a threshold likelihood test statistic TS = 25 integrated above 100 MeV, assuming the typical pulsar spectrum within the source PSF and an underlying diffuse gamma-ray flux from the `rings_Galaxy_v0` model (Abdo et al. 2009f). This is an earlier version of the publicly available[2] model `gll_iem_v02`, similar to the model used for the spectral analysis. We note that the likelihood calculation assumes that the source flux is small compared to the diffuse background flux within the PSF, which is appropriate for a source just at the detection limit. Finally, we converted this map to pulsed sensitivity by a simple scale factor that accounts for the correspondence between the Z_2^2 periodicity test confidence level and the unpulsed likelihood TS for the detected pulsars.

The resulting 5σ sensitivity map for pulsed emission is shown in Figure 9. Comparing the measured fluxes with the predicted sensitivities at the pulsar locations (Figure 10), we see that this 5σ limit indeed provides a reasonable lower envelope to the pulsed detections in this catalog. Thus the effective sensitivity for high latitude (e.g. millisecond) pulsars with known rotation ephemerides is $1 - 2 \times 10^{-8}$ cm^{-2} s^{-1}; at low latitude there is large variation, with typical detection thresholds $3 - 5\times$ higher. We expect the threshold to be somewhat higher for pulsars found in blind period searches. Figure 10 suggests that this threshold is $2 - 3\times$ higher than that for pulsars discovered in folding searches, with resulting values as high as 2×10^{-7} cm^{-2} s^{-1} on the Galactic plane.

The Log N–Log S plot is shown in Figure 11. The approximate $N \propto 1/S$ dependence expected for a disk population is apparent for the higher flux objects. This shows that while radio-selected pulsars are detected down to a threshold of 2×10^{-8} cm^{-2} s^{-1}, the faintest gamma-ray-selected pulsar detected has a flux $\sim 3\times$ higher at 6×10^{-8} cm^{-2} s^{-1}. It is interesting to note that, aside from the lower flux threshold for the former, the radio-selected and gamma-ray-selected histograms are well matched, suggesting similar underlying populations.

5. Discussion

The striking results of the early *Fermi* pulsar discoveries demonstrate the LAT's excellent power for pulsed gamma-ray detection. By increasing the gamma-ray pulsar sample size by nearly an order of magnitude and by firmly establishing the gamma-ray-selected (radio-quiet Geminga-type) and millisecond gamma-ray pulsar populations, we have promoted GeV pulsar astronomy to a major probe of the energetic pulsar population and its magnetospheric physics. Our large pulsar sample allows us both to establish patterns in the pulse emission possibly pointing to a common origin of pulsar gamma-rays and to find anomalous systems that may point to exceptional pulsar geometries and/or unusual emission physics. In this Section we discuss some initial conclusions drawn from the sample, recognizing that the full exploitation of these new results will flow from the detailed population and emission physics studies to follow.

5.1. Pulsar Detectability

A widely-cited predictor of gamma-ray pulsar detectability is the spin-down flux at Earth $\dot{E}/d^2$ (see e.g. Smith et al. 2008). However, as argued by Arons (2006) (see also Harding & Muslimov 2002), it is natural in many models for the gamma-ray emitting gap to maintain a fixed voltage drop. This implies that L_γ is simply proportional to the particle current (Harding 1981), which gives $L_\gamma \propto \dot{E}^{1/2}$, i.e. gamma-ray efficiency increases with decreasing spin-down power down to $\dot{E} \sim 10^{34} - 10^{35}$ erg s^{-1} where the gap saturates at large efficiency. In Figure 12 we show how our detected pulsars rank in $\dot{E}^{1/2}/d^2$ against the set of searched pulsars. We see that for both MSPs and young pulsars, the detected objects have among the largest values of this metric. The presence of missing objects among the detected pulsars is interesting, but must be treated with caution, as the detectability metric may be inflated by poor DM distances, or the sensitivity of the pulse search might be anomalously low due to high local background or unfavorable pulsar spectrum or pulse profile. Alternatively, some missing objects may be truly gamma-ray faint for the Earth line-of-sight. A more complete study of the implications of the pulsar non-detections and upper limits is in progress.

To study the luminosity evolution in the observed pulsar population, we plot in Figure 6 our present best estimate of L_γ against $\dot{E}$, based on the pulsed flux measured for each pulsar. Two important caveats must be emphasized here. First, the inferred luminosities are quadratically sensitive to the often large distance uncertainties. Indeed, for many radio selected pulsars (green points) we have only DM-based distance estimates. For many gamma-ray-selected pulsars we have only rather tenuous SNR or birth cluster associations with rough distance bounds. Only a handful of pulsars have secure parallax-based distances. Second, we have assumed here uniform phase-averaged beaming across the sky (f_Ω=1). This is not realized for many emission models, especially for low $\dot{E}$ pulsars (Watters et al. 2009).

To guide the eye, Figure 6 shows lines for 100% conversion efficiency ($L_\gamma = \dot{E}$) and a heuristic constant voltage line $L_\gamma = (10^{33}\ \mathrm{erg\ s^{-1}}\dot{E})^{1/2}$. In view of the large luminosity uncertainties, we must conclude that it is not yet possible to test the details of the luminosity evolution. However, some trends are apparent and individual objects highlight possible complicating factors. For the highest $\dot{E}$ pulsars, there does seem to be rough agreement with the $\dot{E}^{1/2}$ trend. However, large variance between different distance estimates for the Vela-like PSRs J2021+3651 and J1709−4429 complicate the interpretation. In the range 10^{35} erg s^{-1} $< \dot{E} <$ $10^{36.5}$ erg s^{-1}, the L_γ seems nearly constant, although the lack of precise distance measurements limits our ability to draw conclusions. For example, the very large nominal DM distance of PSR J0248+6021 would require $>$ 100% efficiency, and so is unlikely to be correct. Two other pulsars with apparent high efficiency (J1836+5925 and J2021+4026) are plotted including relatively bright unpulsed emission; this may be magnetospheric, but may also be a surrounding or nearby source. The association distances for the gamma-ray-selected pulsars must additionally be treated with caution. For example PSR J2021+4026 has a $\tau_c \sim 10\times$ larger than the age of the putative associated SNR γ Cygni. Improved distance estimates in this range are the key to probing luminosity evolution.

From 10^{34} erg s^{-1} $< \dot{E} <$ 10^{35} erg s^{-1} we have several nearby pulsars with reasonably accurate parallax distance estimates. However we see a wide range of gamma-ray efficiencies. This is the range over which, for both slot gap and outer gap models, the gap is expected to 'saturate' and use most of the available potential to maintain the pair cascade. In slot gap models (Muslimov & Harding 2003), the break occurs at about 10^{35} erg s^{-1}, when the gap is limited by screening of the accelerating field by pairs. The efficiency below this saturation is predicted to be $\sim$ 10%. In outer gap models (Zhang et al. 2004), the break is predicted to occur at somewhat lower $\dot{E} \sim 10^{34}$ erg s^{-1}. With the present statistics and uncertainties, it is not possible to discriminate between these model predictions except to note that both are consistent with the observed results. In some models the gap saturation dramatically affects the shape of the beam on the sky and accordingly the flux conversion factor f_Ω; for outer gap models Watters et al. (2009) estimate $f_\Omega \sim 0.1 - 0.15$ for Geminga (similar values are obtained for J1836+5925), driving down the rather high inferred luminosity of these pulsars by an order of magnitude. In contrast, another pulsar with an accurate parallax distance, PSR J0659+1414, has an inferred luminosity 30× *lower* than the $\dot{E}^{1/2}$ prediction. Clearly, some parameter in addition to $\dot{E}$ controls the observed L_γ. Finally, for $< 10^{34}$ erg s^{-1} the sample is dominated by the MSPs. These nearby, low luminosity objects clearly lie below the $\dot{E}^{1/2}$ trend, and in fact seem more consistent with $L_\gamma \propto \dot{E}$.

Upper limits on radio pulsars with high values of the spin-down flux at Earth or large $\dot{E}^{1/2}/d^2$ can help constrain viable efficiency models. In practice, the modest present exposure, the large background in the Galactic plane and the need to rely on uncertain dispersion-based distance estimates limit the value of such constraints. Still, a few pulsars are already interesting; for example, using the DM-based distance, the sensitivity in Figure 9, and an assumed $f_\Omega = 1$, we find that PSR J1740+1000 shows less than 1/5 of the flux expected from the $\dot{E}^{1/2}$ (constant voltage) line in Figure 6. Similarly, PSRs J1357−6429 and J1930+1852 have upper limits just below the expected fluxes. Further, some detected pulsars, e.g. PSRs J0659+1414 and J0205+6449, lie significantly below the constant voltage trend. We expect that as LAT exposure and the significance of such limits increase, we should obtain additional constraints on the factors controlling pulsar detectability.

One likely candidate for the additional factor affecting gamma-ray detectability is beaming. For PSR J1930+1852 (Camilo et al. 2002a), X-ray torus fitting (Ng & Romani 2008) suggests a small viewing angle $|\zeta| \sim 33^\circ$. In outer gap models this makes it highly unlikely that the pulsar will produce strong emission on the Earth line-of-sight. Similarly it has been argued that PSR J0659+1414 has a small viewing angle $\zeta < 20^\circ$ (Everett & Weisberg 2001) (but see Weltevrede & Wright (2009) for a discussion of uncertainties). Again, strong emission from above the null charge surface is not expected for this ζ. One possible interpretation is that we are seeing slot gap or even polar cap emission from this pulsar, which is expected at this ζ. The unusual pulse profile and spectrum of this pulsar may allow us to test this idea of alternate emission zones.

In discussing non-detections, we should also note that the only binary pulsar systems reported in this paper are the radio-timed MSPs. In particular, our blind searches are not, as yet, sensitive to pulsars that are undergoing strong acceleration in binary systems. However, we do expect such objects to exist. Population syntheses (Pfahl et al. 2002) suggest that several percent of the young pulsars are born while retained in massive star binary systems. A few such systems are known in the radio pulsar sample (e.g. the TeV-detected PSR B1259−63); we expect that with the gamma-ray signal immune to dispersion effects an appreciable number of pulsar massive-star binaries will eventually be discovered. Indeed, it is entirely possible that the bright gamma-ray binaries LSI +61° 303 (Abdo et al. 2009h) and LS 5039 (Abdo et al. 2009j) may host pulsed GeV signals that have not yet been found.

5.2. Pulsar Population

With the above caveats about missing binary systems in mind, we can already draw some conclusions about the *single* gamma-ray pulsar population. For example, there are 17 gamma-ray selected pulsars with a faintest flux of $\sim 6 \times 10^{-8}\mathrm{cm}^{-2}\mathrm{s}^{-1}$; there are 16 non-millisecond radio-selected pulsars to this flux limit. Of course, some gamma-ray-selected objects can indeed be detected in the radio (Camilo et al. 2009). Indeed, the detection of PSR J1741−2054 at $L_{1.4\mathrm{GHz}} \approx$

0.03 mJy kpc^2 underlines the fact that the radio emission can be very faint. Deep searches for additional radio counterparts are underway. However, with deep radio observations of several objects, e.g. Geminga, PSR J0007+7303, PSR J1836+5925 (Kassim & Lazio 1999; Halpern et al. 2004, 2007), providing no convincing detections, it is clear that some objects are truly radio faint. The substantial number of radio faint objects suggests that gamma-ray emission has an appreciably larger extent than the radio beams, such as expected in the outer gap (OG) and slot-gap/two pole caustic (SG/TPC) models.

Population synthesis studies for normal (non-millisecond) pulsars predicted that LAT would detect from 40–80 radio loud pulsars and comparable numbers of radio quiet pulsars in the first year (Gonthier et al. 2004; Zhang et al. 2007). The ratio of radio-selected to gamma-ray-selected gamma-ray pulsars has been noted as a particularly sensitive discriminator of models, since the outer magnetosphere models predict much smaller ratios than polar cap models (Harding et al. 2007). Studies of the MSP population (Story et al. 2007) predicted that LAT would detect around 12 radio-selected and 33–40 gamma-ray-selected MSPs in the first year, in rough agreement with the number of radio-selected MSPs seen to date (searches for gamma-ray selected MSPs have not yet been conducted). Thus, in the first six months the numbers of LAT pulsar detections are consistent with the predicted range, and the large number of gamma-ray selected pulsars discovered so early in the mission points towards the outer magnetosphere models.

We can in fact use our sample of detected gamma-ray pulsars to estimate the Galactic birthrates. For each object with an available distance estimate, we compute the maximum distance for detection from $D_{\rm max} = D_{\rm est}(F_\gamma/F_{\rm min})^{1/2}$, where $D_{\rm est}$ comes from Table 5, the photon flux F_{100} from Table 4 and $F_{\rm min}$ from Figure 9. We limit $D_{\rm max}$ to 15 kpc, and compare V, the volume enclosed within the estimated source distance, to $V_{\rm max}$, that enclosed within the maximum distance, for a Galactic disk with radius 10 kpc and thickness 1 kpc. If we assume a blind search threshold 2× higher than that for a folding search at a given sky position, the inferred values of $\langle V/V_{\rm max}\rangle$ are 0.49, 0.59 and 0.55 for the radio-selected young pulsars, millisecond pulsars and gamma-ray-selected pulsars, respectively. These are close to 0.5, the value expected for a population uniformly filling a given volume (Schmidt 1968); the MSP value is somewhat high as our sample includes three objects detected at $< 5\sigma$. The value for the gamma-ray-selected pulsars is also high but is controlled by PSR J2032+4127. If we exclude this object from the sample, we get $\langle V/V_{\rm max}\rangle = 0.5$ at an effective threshold of 3× the ephemeris-folding value.

Although we do not attempt a full population synthesis here, if we assume that the pulsar characteristic ages are the true ages, our sample can give rough estimates for local volume birthrates: 8×10^{-5} kpc^{-3} yr^{-1} (young radio-selected), 4×10^{-5} kpc^{-3} yr^{-1} (young gamma-ray-selected, 2× threshold) and 2×10^{-8} kpc^{-3} yr^{-1} (MSP). Note that only half of the gamma-ray-selected objects have distance estimates. If we assume that the set without distance information has comparable luminosity, the gamma-ray-selected birthrate is $\sim 2\times$ larger. These estimates retain appreciable uncertainty; for example if the effective blind search detection threshold is 3× that for folding, the inferred gamma-ray-selected birthrate increases by an additional $\sim 65\%$. If we extrapolate these local birthrates to a full disk with an effective radius of 10 kpc we get 1/100 yr (radio-selected young pulsars), 1/100 yr (gamma-ray-selected pulsars) and $1/(6 \times 10^5$ yr) (radio-selected MSPs). Normally in estimating radio pulsar birthrates one would correct for the radio beaming fraction. However if young gamma-ray-selected pulsars are simply similar objects viewed outside of the radio beam, this would result in double-counting. In any case one infers a total Galactic birthrate for energetic pulsars of $\sim 1/50$ yr, with gamma-ray-selected objects representing half. This represents a large fraction of the estimated Galactic supernova rate, so clearly more careful population syntheses will be needed to see if these numbers are compatible.

5.3. Trends in Light Curves and Other Observables

The pulse shape properties can also help us to probe the geometry and physics of the emission region. The great majority of the pulsars show two dominant, relatively sharp peaks, suggesting that we are seeing caustics from the edge of a hollow cone. When a single peak is seen, it tends to be broader, suggesting a tangential cut through an emission cone. This picture is realized in the OG and the high altitude portion of the SG models.

For the radio-emitting pulsars, we can compare the phase lag between the radio and first gamma-ray peak δ with the separation of the two gamma-ray peaks Δ. As first pointed out in Romani & Yadigaroglu (1995), these should be correlated in outer magnetosphere models — this is indeed seen (Figure 4). The distribution can be compared with predictions of the TPC and OG models shown in Watters et al. (2009). The $\delta - \Delta$ distribution and in particular the presence of $\Delta \sim 0.2 - 0.3$ values appear to favor the OG picture. However, there are a greater number having $\Delta \sim 0.4 - 0.5$, which favors TPC models. In Figure 13 we show the peak separation as a function of pulsar spin-down luminosity — the Δ distribution appears to be bimodal, with no strong dependence on pulsar $\dot{E}$ (or age). A full comparison will require detailed population models, which are being created. It may also be hoped that the precise distribution of measured values can help probe details of the emission geometry. In particular, whenever we have external constraints on the viewing angle ζ (typically from X-ray images of the PWN) or magnetic inclination α (occasionally measured from radio polarization), then the observed values of δ and Δ become a powerful probe of the precise location of the emission sheet within the magnetosphere. This can be sensitive to the field perturbations from magnetospheric currents and hence can probe the global electrodynamics of the pulsar magnetosphere.

If one examines the energy dependence of the light curves of both the radio-selected and gamma-ray-selected pulsars, a decrease in the P1/P2 ratio with increasing energy seems to be a common feature. However, the P1/P2 ratio evolution does not occur for all pulsars, notably J0633+0632, J1028−5819, J1124−5916, J1813−1246, J1826−1256, J1836+5925, J2021+3651, and J2238+59. Most of these pulsars have two peaks with phase separation of ∼0.5 and little or no bridge emission between the peaks. Perhaps the lack of P1/P2 energy evolution is connected with an overall symmetry of the light curve.

The LAT pulsar sample also shows evidence of trends in other observables that may offer additional clues to the pulsar physics. While the detected objects have a wide range of surface magnetic fields, their inferred light cylinder magnetic fields $B_{\rm LC}$ are uniformly relatively large ($\gtrsim 10^3$ G). Indeed, the LAT-detected MSPs are those with the highest light cylinder fields with values very similar to those of the detected normal pulsars. Comparison of the spectral cut-off $E_{\rm cutoff}$ with surface magnetic field shows no significant correlation. This evidence argues against classical low altitude polar cap models supported by γ-B cascades. However, there is a weak correlation of $E_{\rm cutoff}$ with $B_{\rm LC}$, as shown in Figure 7. It is interesting that the values of $E_{\rm cutoff}$ have a range of only about a decade, from 1 to 10 GeV, and that all the different types of pulsars seem to follow the same correlation. This strongly implies that the gamma-ray emission originates in similar locations in the magnetosphere relative to the light cylinder. Such a correlation of $E_{\rm cutoff}$ with $B_{\rm LC}$ is actually expected in all outer magnetosphere models where the gamma-ray emission primarily comes from curvature radiation of electrons whose acceleration is balanced by radiation losses. In this case,

$$E_{\rm cutoff} = 0.32\lambda_c \left(\frac{E_\parallel}{e}\right)^{3/4} \rho_c^{1/2} \tag{8}$$

in $m_{\rm e}c^2$, where λ_c is the electron Compton wavelength, $E_\parallel$ is the electric field that accelerates particles parallel to the magnetic field and ρ_c is the magnetic field radius of curvature. In both SG (Muslimov & Harding 2004) and OG (Zhang et al. 2004; Hirotani 2008) models, $E_\parallel \propto B_{\rm LC}\, w^2$, where w is the gap width. All these models give values of $E_{\rm cutoff}$ that are roughly consistent with those measured for the LAT pulsars. Although $\rho_c \sim R_{\rm LC}$, the gap widths are expected to decrease with increasing $B_{\rm LC}$, so that $E_{\rm cutoff}$ is predicted to be only weakly dependent on $B_{\rm LC}$ in most outer magnetosphere models, as observed.

The detection of pulsed flux at $E_{\rm max} >$ a few GeV provides additional, physical motivation for high altitude emission, since one expects strong (hyper-exponential) attenuation from γ-B$\longrightarrow e^+e^-$ absorption in the high magnetic fields at low altitudes of a near-surface polar gap. For a polar cap model with spin period P and surface field $10^{12}B_{12}$G, Equation 1 of Baring (2004) gives $r \gtrsim (E_{\rm max}B_{12}/1.76{\rm GeV})^{2/7}\, P^{-1/7}\, 10^6$cm. While the largest minimum r is derived from the 25 GeV detection of the Crab by MAGIC (Albert et al. 2008), significant minimum altitudes of 2 to 3 stellar radii are found for many LAT pulsars with large B_{12} and high $E_{\rm cutoff}$, assuming maximum energies set at around $2.5E_{\rm cutoff}$. Such altitudes are inconsistent with the $r \lesssim 1-2$ stellar radii of polar cap models, hence implicating outer magnetosphere (e.g. TPC or OG) models where the bulk of the emission occurs at tens to hundreds of stellar radii.

In Figure 8, we see a general trend for the young pulsars to show a softer spectrum at large $\dot{E}$, although there is a great deal of scatter; a similar trend was noted in Thompson et al. (1999). This may be indicative of higher pair multiplicity, which would steepen the spectrum for the more energetic pulsars, either by steepening the spectrum of the curvature radiation-generating primary electrons (Romani 1996) or by inclusion of an additional soft spectral component associated with robust pair formation (Takata & Chang 2007; Harding et al. 2008). In either case, one would expect steepening from the simple monoenergetic curvature radiation spectrum $\Gamma = 2/3$ for the higher $\dot{E}$ pulsars. Interestingly, the MSPs do not extend the trend to lower $\dot{E}$. Of course EGRET (and now the LAT) find strong variations of photon index with phase for the brighter pulsars. A full understanding of photon index trends will doubtless require phase-resolved modeling.

6. Conclusion

The new gamma-ray pulsar populations established by early LAT observations show that we are detecting many nearby young pulsars. In addition we are detecting the millisecond pulsars with the highest spin-down flux at Earth. Thus we see that the LAT is providing a new, local, but relatively unbiased view of the energetic pulsar population (see Figures 1, 2, and 3). These detections provide a new window into pulsar demographics and physics.

We conclude that a large fraction of the local energetic pulsars are GeV emitters. There is also a significant correlation with X-ray and TeV bright pulsar wind nebulae. Conversely, we have now uncovered the pulsar origin of a large fraction of the bright unidentified Galactic EGRET sources, as proposed by several authors (Kaaret & Cottam 1996; Yadigaroglu & Romani 1997). We have also found plausible pulsar counterparts for several previously detected TeV sources. In this sense the "mystery" of the unidentified EGRET sources is largely solved. It is possible that the two LAT-detected massive binaries (LSI +61° 303, LS 5059) and some of the remaining unidentified sources also contain spin-powered pulsars. Thus we expect that the LAT pulsar population will increase, with both the detection of binary gamma-ray pulsars and fainter and more distant pulsars.

The light curve and spectral evidence summarized above suggests that these pulsars have high altitude emission zones whose fan-like beams scan over a large portion of the celestial sphere. This means that they should provide a relatively unbiased census of energetic neutron star formation. A rough estimate of the young gamma-ray pulsar birthrate extrapolating from our local sample suggests a Galactic birthrate as high as $\sim 1/50$ yr, a large fraction of the estimated Galactic supernova rate. Gamma-ray detectable MSPs in the Galactic field are born rarely, $\sim 1/6 \times 10^5$ yr, but with their long lifetimes are inferred to contribute comparably to the number of (in principle) detectable Galactic gamma-ray pulsars.

The data also advance our understanding of emission zone physics. It is now clear that the gamma-ray emission from the brightest pulsars arises largely in the outer magnetosphere. The photon emission also accounts for a large fraction of the spin-down luminosity, increasing as the pulsars approach $\dot{E} \sim 10^{33-34}$ erg s^{-1}. While these wide, bright beams are a boon for population studies, as noted above, they represent a challenge for theorists trying to understand pulsar magnetospheres. Further LAT pulsar observations and, in particular, the high quality, highly phase-resolved spectra now being obtained for the brightest LAT pulsars will surely sharpen this challenge.

The *Fermi* LAT Collaboration acknowledges the generous support of a number of agencies and institutes that have supported the Fermi LAT Collaboration. These include the National Aeronautics and Space Administration and the Department of Energy in the United States, the Commissariat à l'Energie Atomique and the Centre National de la Recherche Scientifique / Institut National de Physique Nucléaire et de Physique des Particules in France, the Agenzia Spaziale Italiana and the Istituto Nazionale di Fisica Nucleare in Italy, the Ministry of Education, Culture, Sports, Science and Technology (MEXT), High Energy Accelerator Research Organization (KEK) and Japan Aerospace Exploration Agency (JAXA) in Japan, and the K. A. Wallenberg Foundation and the Swedish National Space Board in Sweden.

Additional support for science analysis during the operations phase is gratefully acknowledged from the Istituto Nazionale di Astrofisica in Italy and the Centre National d'Études Spatiales in France.

The Parkes radio telescope is part of the Australia Telescope which is funded by the Commonwealth Government for operation as a National Facility managed by CSIRO. The Green Bank Telescope is operated by the National Radio Astronomy Observatory, a facility of the National Science Foundation operated under cooperative agreement by Associated Universities, Inc. The Arecibo Observatory is part of the National Astronomy and Ionosphere Center (NAIC), a national research center operated by Cornell University under a cooperative agreement with the National Science Foundation. The Nançay Radio Observatory is operated by the Paris Observatory, associated with the French Centre National de la Recherche Scientifique (CNRS). The Lovell Telescope is owned and operated by the University of Manchester as part of the Jodrell Bank Centre for Astrophysics with support from the Science and Technology Facilities Council of the United Kingdom. The Westerbork Synthesis Radio Telescope is operated by Netherlands Foundation for Radio Astronomy, ASTRON.

REFERENCES

Abdo, A. A., et al. 2008, Science, 322, 1218, (CTA1)

—. 2009a, ApJ, submitted (Geminga)

—. 2009b, Science, 325, 848, (Millisecond Pulsars)

—. 2009c, Science, 325, 840, (Blind Search Pulsars)

—. 2009d, ApJ, 699, L102, (PSR J0205+6449)

—. 2009e, ApJ, 695, L72, (PSR J1028−5819)

—. 2009f, ApJ, 706, 1331, (PSRs J1048−5832 and J2229+6114)

—. 2009g, ApJ, 696, 1084, (Vela)

—. 2009h, ApJ, 701, L123, (LSI+61°303)

—. 2009i, ApJS, 183, 46, (Bright Source List)

—. 2009j, ApJ, 706, L56, (LS5039)

—. 2009k, ApJ, 700, L127, (Milagro Observations of Bright Source List)

—. 2009l, Science, 326, 1512, (Cyg X-3)

—. 2009m, ApJ, 700, 1059, (PSR J2021+3651)

—. 2009n, ApJ, 699, 1171, (PSR J0030+0451)

—. 2009o, Astroparticle Physics, 32, 193, (On-orbit calibration)

—. 2010a, ApJ, in prep (Three EGRET Pulsars)

—. 2010b, ApJ, in press, arXiv:1001.0792 (PSR J1907+0602)

—. 2010c, ApJ, in prep (γ-Cygni)

—. 2010d, ApJ, 708, 1254, (Crab)

Aharonian, F., et al. 2006a, A&A, 456, 245

—. 2006b, A&A, 448, L43

—. 2006c, A&A, 457, 899

—. 2007, A&A, 472, 489

—. 2009, A&A, 499, 723

Albert, J., et al. 2008, ApJ, 674, 1037

Arons, J. 1996, A&AS, 120, C49

—. 2006, On the Present and Future of Pulsar Astronomy, 26th meeting of the IAU, Joint Discussion 2, 16-17 August, 2006, Prague, Czech Republic, JD02, #39, 2

Atwood, W. B., Ziegler, M., Johnson, R. P., & Baughman, B. M. 2006, ApJ, 652, L49

Atwood, W. B., et al. 2009, ApJ, 697, 1071, (LAT)

Backer, D. C., Dexter, M. R., Zepka, A., Ng, D., Werthimer, D. J., Ray, P. S., & Foster, R. S. 1997, PASP, 109, 61

Baring, M. G. 2004, Advances in Space Research, 33, 552

Bassa, C. G., van Kerkwijk, M. H., & Kulkarni, S. R. 2003, A&A, 403, 1067

Becker, W. 2009, in Astrophysics and Space Science Library, Vol. 357, Astrophysics and Space Science Library, ed. W. Becker

Boinee, P., et al. 2003, in Science with the New Generation of High Energy Gamma-Ray Experiments: Between Astrophysics and Astroparticle Physics, ed. S. Ciprini, A. de Angelis, P. Lubrano, & O. Mansutti, 141

Brisken, W. F., Fruchter, A. S., Goss, W. M., Herrnstein, R. M., & Thorsett, S. E. 2003, AJ, 126, 3090

Browning, R., Ramsden, D., & Wright, P. J. 1971, Nature, 232, 99

Buccheri, R., et al. 1983, A&A, 128, 245

Camilo, F., Lorimer, D. R., Bhat, N. D. R., Gotthelf, E. V., Halpern, J. P., Wang, Q. D., Lu, F. J., & Mirabal, N. 2002a, ApJ, 574, L71

Camilo, F., Manchester, R. N., Gaensler, B. M., & Lorimer, D. R. 2002b, ApJ, 579, L25

Camilo, F., Manchester, R. N., Gaensler, B. M., Lorimer, D. R., & Sarkissian, J. 2002c, ApJ, 567, L71

Camilo, F., Ransom, S. M., Gaensler, B. M., Slane, P. O., Lorimer, D. R., Reynolds, J., Manchester, R. N., & Murray, S. S. 2006, ApJ, 637, 456

Camilo, F., et al. 2002d, ApJ, 571, L41

—. 2009, ApJ, 705, 1

—. 2010, ApJ, in prep (PSRs J1833−1034 and J1747−2958)

Caraveo, P. A., Lattanzi, M. G., Massone, G., Mignani, R. P., Makarov, V. V., Perryman, M. A. C., & Bignami, G. F. 1998, A&A, 329, L1

Casandjian, J.-M., & Grenier, I. A. 2008, A&A, 489, 849

Caswell, J. L., & Haynes, R. F. 1987, A&A, 171, 261

Chandler, A. M., Koh, D. T., Lamb, R. C., Macomb, D. J., Mattox, J. R., Prince, T. A., & Ray, P. S. 2001, ApJ, 556, 59

Cheng, K. S., & Zhang, L. 1998, ApJ, 498, 327

Cognard, I., Theureau, G., Desvignes, G., & Ferdman, R. 2009, in Windows on the Universe, XXI Rencontres de Blois, France, June 21-26 2009, ed. J. T. T. Van, GPU dedispersor at Nancay Radiotelescope, arXiv:0911.1612

Cognard, I., et al. 2010, A&A, in prep - (PSRs J0248+6021 and J2240+5832)

Cordes, J. M., & Lazio, T. J. W. 2002, ArXiv e-prints, (arXiv:astro-ph/0207156)

Crawford, F., Roberts, M. S. E., Hessels, J. W. T., Ransom, S. M., Livingstone, M., Tam, C. R., & Kaspi, V. M. 2006, ApJ, 652, 1499

D'Agostini, G. 1995, Nuclear Instruments and Methods in Physics Research A, 362, 487

D'Amico, N., et al. 2001, ApJ, 552, L45

De Becker, M., Rauw, G., & Swings, J.-P. 2005, Ap&SS, 297, 291

de Jager, O. C., Raubenheimer, B. C., & Swanepoel, J. W. H. 1989, A&A, 221, 180

Deller, A. T., Verbiest, J. P. W., Tingay, S. J., & Bailes, M. 2008, ApJ, 685, L67

Djannati-Ataï, A., De Jager, O. C., Terrier, R., Gallant, Y. A., & Hoppe, S. 2007, ArXiv e-prints, (arXiv:0710.2247)

Dodson, R., Legge, D., Reynolds, J. E., & McCulloch, P. M. 2003, ApJ, 596, 1137

Edwards, R. T., Hobbs, G. B., & Manchester, R. N. 2006, MNRAS, 372, 1549

Everett, J. E., & Weisberg, J. M. 2001, ApJ, 553, 341

Faherty, J., Walter, F. M., & Anderson, J. 2007, Ap&SS, 308, 225

Fesen, R., Rudie, G., Hurford, A., & Soto, A. 2008, ApJS, 174, 379

Fesen, R. A., Kirshner, R. P., & Becker, R. H. 1988, in IAU Colloq. 101: Supernova Remnants and the Interstellar Medium, ed. R. S. Roger & T. L. Landecker, 55

Fierro, J. M., et al. 1995, ApJ, 447, 807

Gaensler, B. M., van der Swaluw, E., Camilo, F., Kaspi, V. M., Baganoff, F. K., Yusef-Zadeh, F., & Manchester, R. N. 2004, ApJ, 616, 383

Gaensler, B. M., & Wallace, B. J. 2003, ApJ, 594, 326

Gold, T. 1968, Nature, 218, 731

Gonthier, P. L., Ouellette, M. S., Berrier, J., O'Brien, S., & Harding, A. K. 2002, ApJ, 565, 482

Gonthier, P. L., Van Guilder, R., & Harding, A. K. 2004, ApJ, 604, 775

Gonzalez, M., & Safi-Harb, S. 2003, ApJ, 583, L91

Goodman, J., & Sinnis, G. 2009, The Astronomer's Telegram, 2172, 1

Gotthelf, E. V. 2003, ApJ, 591, 361

Green, D. A. 2009, Bulletin of the Astronomical Society of India, 37, 45

Green, D. A., & Gull, S. F. 1982, Nature, 299, 606

Greidanus, H., & Strom, R. G. 1990, A&A, 240, 376

Halpern, J. P., Camilo, F., & Gotthelf, E. V. 2007, ApJ, 668, 1154

Halpern, J. P., Camilo, F., Gotthelf, E. V., Helfand, D. J., Kramer, M., Lyne, A. G., Leighly, K. M., & Eracleous, M. 2001a, ApJ, 552, L125

Halpern, J. P., Gotthelf, E. V., Camilo, F., Helfand, D. J., & Ransom, S. M. 2004, ApJ, 612, 398

Halpern, J. P., Gotthelf, E. V., Leighly, K. M., & Helfand, D. J. 2001b, ApJ, 547, 323

Halpern, J. P., et al. 2008, ApJ, 688, L33

Harding, A. K. 1981, ApJ, 245, 267

Harding, A. K., Grenier, I. A., & Gonthier, P. L. 2007, Ap&SS, 309, 221

Harding, A. K., & Muslimov, A. G. 2002, ApJ, 568, 862

Harding, A. K., Stern, J. V., Dyks, J., & Frackowiak, M. 2008, ApJ, 680, 1378

Hartman, R. C., et al. 1999, ApJS, 123, 79

Hewish, A., Bell, S. J., Pilkington, J. D. H., Scott, P. F., & Collins, R. A. 1968, Nature, 217, 709

Hirotani, K. 2008, ApJ, 688, L25

Hobbs, G., Edwards, R., & Manchester, R. 2006, Chinese Journal of Astronomy and Astrophysics Supplement, 6, 189

Hobbs, G. B., Lyne, A. G., Kramer, M., Martin, C. E., & Jordan, C. 2004, MNRAS, 353, 1311

Hoppe, S., de Oña-Wilhemi, E., Khélifi, B., Chaves, R. C. G., de Jager, O. C., Stegmann, C., Terrier, R., & for the H. E. S. S. Collaboration. 2009, ArXiv e-prints, (arXiv:0906.5574)

Hotan, A. W., Bailes, M., & Ord, S. M. 2006, MNRAS, 369, 1502

Jackson, M. S., & Halpern, J. P. 2005, ApJ, 633, 1114

Johnston, S., Manchester, R. N., Lyne, A. G., D'Amico, N., Bailes, M., Gaensler, B. M., & Nicastro, L. 1996, MNRAS, 279, 1026

Kaaret, P., & Cottam, J. 1996, ApJ, 462, L35

Kanbach, G., et al. 1980, A&A, 90, 163

Kaplan, D. L., et al. 2005, PASP, 117, 643

Kaspi, V. M., Lackey, J. R., Mattox, J., Manchester, R. N., Bailes, M., & Pace, R. 2000, ApJ, 528, 445

Kassim, N. E., & Lazio, T. J. W. 1999, ApJ, 527, L101

Keith, M. J., Johnston, S., Kramer, M., Weltevrede, P., Watters, K. P., & Stappers, B. W. 2008, MNRAS, 389, 1881

Kniffen, D. A., Hartman, R. C., Thompson, D. J., Bignami, G. F., & Fichtel, C. E. 1974, Nature, 251, 397

Koribalski, B., Johnston, S., Weisberg, J. M., & Wilson, W. 1995, ApJ, 441, 756

Kothes, R., Uyaniker, B., & Pineault, S. 2001, ApJ, 560, 236

Kramer, M., et al. 2003, MNRAS, 342, 1299

Kuiper, L., Hermsen, W., Cusumano, G., Diehl, R., Schönfelder, V., Strong, A., Bennett, K., & McConnell, M. L. 2001, A&A, 378, 918

Kuiper, L., Hermsen, W., Krijger, J. M., Bennett, K., Carramiñana, A., Schönfelder, V., Bailes, M., & Manchester, R. N. 1999, A&A, 351, 119

Kuiper, L., Hermsen, W., Verbunt, F., Thompson, D. J., Stairs, I. H., Lyne, A. G., Strickman, M. S., & Cusumano, G. 2000, A&A, 359, 615

Lamb, R. C., & Macomb, D. J. 1997, ApJ, 488, 872

Landecker, T. L., Roger, R. S., & Higgs, L. A. 1980, A&AS, 39, 133

Lommen, A. N., Kipphorn, R. A., Nice, D. J., Splaver, E. M., Stairs, I. H., & Backer, D. C. 2006, ApJ, 642, 1012

Lyne, A. G., et al. 1998, MNRAS, 295, 743

Manchester, R. N. 2008, in American Institute of Physics Conference Series, Vol. 983, 40 Years of Pulsars: Millisecond Pulsars, Magnetars and More, ed. C. Bassa, Z. Wang, A. Cumming, & V. M. Kaspi, 584

Manchester, R. N., Hobbs, G. B., Teoh, A., & Hobbs, M. 2005, AJ, 129, 1993

Manchester, R. N., et al. 2001, MNRAS, 328, 17

Mazziotta, M. N. 2009, ArXiv e-prints, (arXiv:0907.0638)

McGowan, K. E., Zane, S., Cropper, M., Kennea, J. A., Córdova, F. A., Ho, C., Sasseen, T., & Vestrand, W. T. 2004, ApJ, 600, 343

McLaughlin, M. A., & Cordes, J. M. 2000, ApJ, 538, 818

Muslimov, A. G., & Harding, A. K. 2003, ApJ, 588, 430

—. 2004, ApJ, 606, 1143

Navarro, J., de Bruyn, A. G., Frail, D. A., Kulkarni, S. R., & Lyne, A. G. 1995, ApJ, 455, L55+

Ng, C.-Y., Roberts, M. S. E., & Romani, R. W. 2005, ApJ, 627, 904

Ng, C.-Y., & Romani, R. W. 2008, ApJ, 673, 411

Nice, D. J., Splaver, E. M., Stairs, I. H., Löhmer, O., Jessner, A., Kramer, M., & Cordes, J. M. 2005, ApJ, 634, 1242

Nolan, P. L., et al. 1996, A&AS, 120, C61

Noutsos, A., et al. 2010, ApJ, in prep (PSR J2043+2740)

Oka, T., Kawai, N., Naito, T., Horiuchi, T., Namiki, M., Saito, Y., Romani, R. W., & Kifune, T. 1999, ApJ, 526, 764

Pacini, F. 1968, Nature, 219, 145

Pellizzoni, A., et al. 2009, ApJ, 695, L115

Pfahl, E., Rappaport, S., Podsiadlowski, P., & Spruit, H. 2002, ApJ, 574, 364

Pineault, S., Landecker, T. L., Madore, B., & Gaumont-Guay, S. 1993, AJ, 105, 1060

Pittori, C., et al. 2009, A&A, 506, 1563

Possenti, A., Cerutti, R., Colpi, M., & Mereghetti, S. 2002, A&A, 387, 993

Ramanamurthy, P. V., Fichtel, C. E., Kniffen, D. A., Sreekumar, P., & Thompson, D. J. 1996, ApJ, 458, 755

Ray, P. S., Thorsett, S. E., Jenet, F. A., van Kerkwijk, M. H., Kulkarni, S. R., Prince, T. A., Sandhu, J. S., & Nice, D. J. 1996, ApJ, 470, 1103

Ray, P. S., et al. 2010, ApJ, in prep (Precise Timing of Fermi Gamma-Ray Pulsars)

Roberts, D. A., Goss, W. M., Kalberla, P. M. W., Herbstmeier, U., & Schwarz, U. J. 1993, A&A, 274, 427

Roberts, M. S. E., Brogan, C. L., Gaensler, B. M., Hessels, J. W. T., Ng, C.-Y., & Romani, R. W. 2005, Ap&SS, 297, 93

Roberts, M. S. E., Hessels, J. W. T., Ransom, S. M., Kaspi, V. M., Freire, P. C. C., Crawford, F., & Lorimer, D. R. 2002, ApJ, 577, L19

Romani, R. W. 1996, ApJ, 470, 469

Romani, R. W., Ng, C.-Y., Dodson, R., & Brisken, W. 2005, ApJ, 631, 480

Romani, R. W., & Yadigaroglu, I.-A. 1995, ApJ, 438, 314

Romero, G. E., Benaglia, P., & Torres, D. F. 1999, A&A, 348, 868

Schlegel, D. J., Finkbeiner, D. P., & Davis, M. 1998, ApJ, 500, 525

Schmidt, M. 1968, ApJ, 151, 393

Shklovskii, I. S. 1970, Soviet Astronomy, 13, 562

Smith, D. A., et al. 2008, A&A, 492, 923

Staveley-Smith, L., et al. 1996, Publications of the Astronomical Society of Australia, 13, 243

Story, S. A., Gonthier, P. L., & Harding, A. K. 2007, ApJ, 671, 713

Takata, J., & Chang, H.-K. 2007, ApJ, 670, 677

Taylor, J. H. 1992, Royal Society of London Philosophical Transactions Series A, 341, 117

Taylor, J. H., Manchester, R. N., & Lyne, A. G. 1993, ApJS, 88, 529

Theureau, G., et al. 2005, A&A, 430, 373

Thompson, D. J. 2004, in Astrophysics and Space Science Library, Vol. 304, Cosmic Gamma-Ray Sources, ed. K. S. Cheng & G. E. Romero, 149

Thompson, D. J., Fichtel, C. E., Kniffen, D. A., & Ogelman, H. B. 1975, ApJ, 200, L79

Thompson, D. J., et al. 1994, ApJ, 436, 229

—. 1999, ApJ, 516, 297

Toscano, M., Britton, M. C., Manchester, R. N., Bailes, M., Sandhu, J. S., Kulkarni, S. R., & Anderson, S. B. 1999, ApJ, 523, L171

Trimble, V. 1973, PASP, 85, 579

Uchida, K., Morris, M., & Yusef-Zadeh, F. 1992, AJ, 104, 1533

Van Etten, A., Romani, R. W., & Ng, C.-Y. 2008, ApJ, 680, 1417

Voûte, J. L. L., Kouwenhoven, M. L. A., van Haren, P. C., Langerak, J. J., Stappers, B. W., Driesens, D., Ramachandran, R., & Beijaard, T. D. 2002, A&A, 385, 733

Walker, M., Mori, M., & Ohishi, M. 2003, ApJ, 589, 810

Watters, K. P., Romani, R. W., Weltevrede, P., & Johnston, S. 2009, ApJ, 695, 1289

Weltevrede, P., & Wright, G. 2009, MNRAS, 395, 2117

Weltevrede, P., et al. 2009, PASA in press, arXiv:0909.5510

—. 2010, ApJ, 708, 1426

Yadigaroglu, I.-A., & Romani, R. W. 1997, ApJ, 476, 347

Zepka, A., Cordes, J. M., Wasserman, I., & Lundgren, S. C. 1996, ApJ, 456, 305

Zhang, L., Cheng, K. S., Jiang, Z. J., & Leung, P. 2004, ApJ, 604, 317

Zhang, L., Fang, J., & Chen, S. B. 2007, ApJ, 666, 1165

Ziegler, M., Baughman, B. M., Johnson, R. P., & Atwood, W. B. 2008, ApJ, 680, 620

This preprint was prepared with the AAS LaTeX macros v5.2.

Table 1. Measured and intrinsic parameters of LAT-detected pulsars

PSR	Type, *Ref.*	l (°)	b (°)	P (ms)	$\dot{P}$ (10^{-15})	age τ_c (kyr)	$\dot{E}$ (10^{34} erg s^{-1})	B_{LC} (kG)	S_{1400} (mJy)
J0007+7303	g [a,b]	119.7	10.5	316	361	14	45.2	3.1	[1] < 0.1
J0030+0451	m [c,d]	113.1	−57.6	4.9	10×10^{-6}	7.7×10^{6}	0.3	17.8	0.6
J0205+6449	r [e]	130.7	3.1	65.7	194	5	2700	115.9	0.04
J0218+4232	mb [d]	139.5	−17.5	2.3	77×10^{-6}	0.5×10^{6}	24	313.1	0.9
J0248+6021	r [f]	137.0	0.4	217	55.1	63	21	3.1	9
J0357+32	g [b]	162.7	−16.0	444	12.0	590	0.5	0.2	···
J0437−4715	mb [d]	253.4	−42.0	5.8	14×10^{-6}	6.6×10^{6}	0.3	13.7	140
J0534+2200	r [h]	184.6	−5.8	33.1	423	1	46100	950.0	14
J0613−0200	mb [d]	210.4	−9.3	3.1	9×10^{-6}	5.3×10^{6}	1.3	54.3	1.4
J0631+1036	r [i]	201.2	0.5	288	105	44	17.3	2.1	0.8
J0633+0632	g [b]	205.0	−1.0	297	79.5	59	11.9	1.7	[2] < 0.2
J0633+1746	g [h]	195.1	4.3	237	11.0	340	3.3	1.1	< 1
J0659+1414	r [i]	201.1	8.3	385	55.0	110	3.8	0.7	3.7
J0742−2822	r [i]	243.8	−2.4	167	16.8	160	14.3	3.3	15
J0751+1807	mb [d]	202.7	21.1	3.5	6×10^{-6}	8.0×10^{6}	0.6	32.3	3.2
J0835−4510	r [k]	263.6	−2.8	89.3	124	11	688	43.4	1100
J1028−5819	r [l]	285.1	−0.5	91.4	16.1	90	83.2	14.6	0.36
J1048−5832	r [m]	287.4	0.6	124	96.3	20	201	16.8	6.5
J1057−5226	r [n]	286.0	6.6	197	5.8	540	3.0	1.3	11
J1124−5916	r	292.0	1.8	135	747	3	1190	37.3	0.08
J1418−6058	g [b]	313.3	0.1	111	170	10	495	29.4	[2,3] < 0.06
J1420−6048	r [i]	313.5	0.2	68.2	83.2	13	1000	69.1	0.9
J1459−60	g [b]	317.9	−1.8	103	25.5	64	91.9	13.6	[2] < 0.2
J1509−5850	r [i]	320.0	−0.6	88.9	9.2	150	51.5	11.8	0.15
J1614−2230	mb [d]	352.5	20.3	3.2	4×10^{-6}	1.2×10^{6}	0.5	33.7	···
J1709−4429	r [n]	343.1	−2.7	102	93.0	18	341	26.4	7.3
J1718−3825	r [i]	349.0	−0.4	74.7	13.2	90	125	21.9	1.3
J1732−31	g [b]	356.2	0.9	197	26.1	120	13.6	2.7	[2] < 0.2
J1741−2054	g [b,t]	6.4	4.6	414	16.9	390	0.9	0.3	[2] 0.16
J1744−1134	m [d]	14.8	9.2	4.1	7×10^{-6}	9×10^{6}	0.4	24.0	3
J1747−2958	r [o]	359.3	−0.8	98.8	61.3	26	251	23.5	0.08
J1809−2332	g [b]	7.4	−2.0	147	34.4	68	43.0	6.5	[2,3] < 0.06
J1813−1246	g [b]	17.2	2.4	48.1	17.6	43	626	76.2	[2] < 0.2
J1826−1256	g [b]	18.5	−0.4	110	121	14	358	25.2	[2,3] < 0.06
J1833−1034	r [o]	21.5	−0.9	61.9	202	5	3370	137.3	0.07
J1836+5925	g [b]	88.9	25.0	173	1.5	1800	1.2	0.9	[4] < 0.007
J1907+06	g [b,r]	40.2	−0.9	107	87.3	19	284	23.2	< 0.02
J1952+3252	r [n]	68.8	2.8	39.5	5.8	110	374	71.6	1
J1958+2846	g [b]	65.9	−0.2	290	222	21	35.8	3.0	···
J2021+3651	r [p]	75.2	0.1	104	95.6	17	338	26.0	0.1
J2021+4026	g [b,s]	78.2	2.1	265	54.8	77	11.6	1.9	···
J2032+4127	g [b,t]	80.2	1.0	143	19.6	120	26.3	5.3	[2] 0.24
J2043+2740	r [q]	70.6	−9.2	96.1	1.3	1200	5.6	3.6	[5] 3
J2124−3358	m [d]	10.9	−45.4	4.9	12×10^{-6}	0.6×10^{6}	0.4	18.8	1.6
J2229+6114	r [m]	106.6	2.9	51.6	78.3	11	2250	134.5	0.25

Table 1—Continued

PSR	Type, *Ref.*	l (°)	b (°)	P (ms)	$\dot{P}$ (10^{-15})	age τ_c (kyr)	$\dot{E}$ (10^{34} erg s^{-1})	B_{LC} (kG)	S_{1400} (mJy)
J2238+59	g ^{b}	106.5	0.5	163	98.6	26	90.3	8.6	···

Note. — The first two columns are pulsar names and types: r for radio-selected, g for gamma-ray-selected, m for MSPs, and b for binary pulsars. The 3^{rd} and 4^{th} columns are Galactic coordinates for each pulsar. The 5^{th} and 6^{th} columns list the period (P) and its first derivative ($\dot{P}$), corrected for the Shklovskii effect (see text). Following are the characteristic age τ_c (column 7), the spin-down luminosity $\dot{E}$ (column 8), and the magnetic field at the light cylinder $B_{\rm LC}$ (column 9) . The last column is the radio flux density at 1400 MHz, or an upper limit when one is available. These values are taken from the ATNF database (Manchester et al. 2005) except for the noted entries where: (1) (Halpern et al. 2004); (2) (Camilo et al. 2009); (3) (Roberts et al. 2002); (4) (Halpern et al. 2007); (5) (Ray et al. 1996). Note that PSR J1509−5850 should not be confused with PSR B1509−58 observed by *CGRO*.

References. — References to *Fermi* LAT publications specific to these pulsars: *a* (Abdo et al. 2008) ; *b* (Abdo et al. 2009c) ; *c* (Abdo et al. 2009n) ; *d* (Abdo et al. 2009b) ; *e* (Abdo et al. 2009d) ; *f* (Cognard et al. 2010) ; *h* (Abdo et al. 2010d) ; *i* (Weltevrede et al. 2010) ; *j* (Abdo et al. 2009a) ; *k* (Abdo et al. 2009g) ; *l* (Abdo et al. 2009e) ; *m* (Abdo et al. 2009f) ; *n* (Abdo et al. 2010a) ; *o* (Camilo et al. 2010) ; *p* (Abdo et al. 2009m) ; *q* (Noutsos et al. 2010) ; *r* (Abdo et al. 2010b) ; *s* (Abdo et al. 2010c) ; *t* (Camilo et al. 2009).

Table 2. Pulsation detection significances for LAT-detected pulsars

PSR	Z_2^2 value	H value	maxROI(°)	ObsID
J0007+7303	2072.1	2371.8	1.0	L
J0030+0451	121.1	362.7	1.0	N
J0205+6449	90.9	206.0	1.0	G, J
J0218+4232	24.7	22.5	1.0	N, W
J0248+6021	57.5	75.1	0.5	N
J0357+32	422.7	450.7	1.0	L
J0437−4715	126.9	153.6	1.0	P
J0534+2200	4397.8	15285.0	1.0	N, J
J0613−0200	93.6	139.9	1.0	N
J0631+1036	48.6	44.8	1.0	N, J
J0633+0632	230.2	573.3	1.0	L
J0633+1746	10053.6	20346.4	1.0	L
J0659+1414	80.5	99.0	1.0	N, J
J0742−2822	38.9	44.9	1.0	N, J
J0751+1807	29.7	26.5	1.0	N
J0835−4510	26903.9	74716.7	1.0	P
J1028−5819	291.5	915.9	0.5	P
J1048−5832	208.5	634.0	1.0	P
J1057−5226	1668.9	1772.4	1.0	P
J1124−5916	93.5	179.9	1.0	L
J1418−6058	230.1	343.7	1.0	L
J1420−6048	104.7	114.4	1.0	P
J1459−60	148.2	159.3	1.0	L
J1509−5850	71.6	73.3	0.5	P
J1614−2230	36.2	69.5	0.5	G
J1709−4429	4680.1	5612.1	1.0	P
J1718−3825	111.9	109.8	0.5	N, P
J1732−31	141.2	279.6	1.0	L
J1741−2054	332.6	355.9	1.0	L
J1744−1134	28.4	38.1	1.0	N
J1747−2958	47.2	69.0	0.5	G
J1809−2332	589.3	1562.5	1.0	L
J1813−1246	140.0	162.0	1.0	L
J1826−1256	442.4	979.0	1.0	L
J1833−1034	35.2	87.6	1.0	G
J1836+5925	349.2	385.3	1.0	L
J1907+06	257.1	521.0	1.0	L
J1952+3252	464.8	1008.8	1.0	J, N
J1958+2846	146.9	233.1	1.0	L
J2021+3651	1433.5	4603.7	1.0	G, A
J2021+4026	222.0	275.8	1.0	L
J2032+4127	224.9	485.9	0.5	L
J2043+2740	28.2	38.2	1.0	N, J
J2124−3358	77.8	80.9	1.0	N
J2229+6114	1026.0	1237.4	1.0	G, J
J2238+59	135.8	373.0	1.0	L

Table 2—Continued

PSR	Z_2^2 value	H value	maxROI($^\circ$)	ObsID

Note. — Columns 2 and 3 list the Z_2^2 (Buccheri et al. 1983) and H (de Jager et al. 1989) periodicity test values for $E > 0.3$ GeV respectively. Detection of gamma-ray pulsations are claimed when the significance of the periodicity test exceeds 5σ, with the exceptions of J0218+4232, J0751+1807, J1744−1134, and J2043+2740 as described in Section 2.1.3. A significance greater than 5σ corresponds to $Z_2^2 > 36$ and $H > 42$; greater than 7σ corresponds to $Z_2^2 > 61$; and greater than 10σ corresponds to $Z_2^2 > 114$ (see Section 2.1.3). Column 4 gives the maximum angular radius (maxROI) around the pulsar position within which gamma-ray events were searched for pulsations. The final column indicates the observatories that provided ephemerides (see Section 2.1.1 for details): “A” – Arecibo telescope; “G” – Green Bank Telescope; “J” – Lovell telescope at Jodrell Bank; “L” – Large Area Telescope; “N” – Nançay Radio Telescope; “P” – Parkes radio telescope; “W” – Westerbork Synthesis Radio Telescope.

Table 3. Pulse shape parameters of LAT-detected pulsars

PSR	Type[a]	Peak multiplicity	Radio lag δ	γ-ray peak separation Δ	Off-pulse definition ϕ
J0007+7303	g	2	...	0.23 ± 0.01	0.29 – 0.87
J0030+0451	m	2	0.18 ± 0.01	0.44 ± 0.01	0.68 – 0.12
J0205+6449	r	2	0.08 ± 0.01	0.50 ± 0.01	0.64 – 0.02
J0218+4232	m	2	0.32 ± 0.02	0.36 ± 0.02	0.84 – 0.16
J0248+6021	r	1	0.35 ± 0.01	...	0.71 – 0.19
J0357+32	g	1	...	...	0.34 – 0.86
J0437−4715	m	1	0.43 ± 0.02	...	0.60 – 0.20
J0534+2200	r	2	0.09 ± 0.01	0.40 ± 0.01	0.62 – 0.98
J0613−0200	m	1	0.42 ± 0.01	...	0.56 – 0.16
J0631+1036	r	1	0.54 ± 0.02	...	0.80 – 0.20
J0633+0632	g	2	...	0.48 ± 0.01	0.09 – 0.45
J0633+1746	g	2	...	0.50 ± 0.01	0.24 – 0.54
J0659+1414	r	1	0.21 ± 0.01	...	0.40 – 1.00
J0742−2822	r	1	0.61 ± 0.02	...	0.84 – 0.44
J0751+1807	m	1	0.43 ± 0.02	...	0.63 – 0.99
J0835−4510	r	2	0.13 ± 0.01	0.43 ± 0.01	0.66 – 0.06
J1028−5819	r	2	0.19 ± 0.01	0.47 ± 0.01	0.76 – 0.12
J1048−5832	r	2	0.15 ± 0.01	0.42 ± 0.02	0.64 – 0.04
J1057−5226	r	2	0.35 ± 0.05	0.20 ± 0.07	0.72 – 0.20
J1124−5916	r	2	**0.11 ± 0.01**	0.49 ± 0.01	**0.70 – 0.06**
J1418−6058	g	2	...	0.47 ± 0.01	0.54 – 0.90
J1420−6048	r	2[b]	0.26 ± 0.02	0.18 ± 0.02	0.60 – 0.10
J1459−60	g	2	...	0.15 ± 0.03	0.34 – 0.78
J1509−5850	r	2[b]	0.18 ± 0.03	0.20 ± 0.03	0.52 – 1.00
J1614−2230	m	2	0.19 ± 0.01	0.51 ± 0.01	0.92 – 0.14
J1709−4429	r	2	0.24 ± 0.01	0.25 ± 0.01	0.66 – 0.14
J1718−3825	r	1	0.42 ± 0.02	...	0.68 – 0.20
J1732−31	g	2	...	0.42 ± 0.02	0.49 – 0.93
J1741−2054	g	2	0.30 ± 0.01	0.18 ± 0.02	0.67 – 0.19
J1744−1134	m	1	0.83 ± 0.02	...	0.08 – 0.44
J1747−2958	r	2	0.18 ± 0.01	0.42 ± 0.04	0.64 – 0.10
J1809−2332	g	2	...	0.35 ± 0.01	0.41 – 0.89
J1813−1246	g	2	...	0.47 ± 0.02	0.56 – 0.90
J1826−1256	g	2	...	0.47 ± 0.01	0.54 – 0.94
J1833−1034	r	2	0.15 ± 0.01	0.44 ± 0.01	0.68 – 0.10
J1836+5925	g	2	...	0.48 ± 0.01	...
J1907+06	g	2	...	0.40 ± 0.01	0.46 – 0.94
J1952+3252	r	2	0.15 ± 0.01	0.49 ± 0.01	0.68 – 0.08
J1958+2846	g	2	...	0.45 ± 0.01	0.55 – 0.95
J2021+3651	r	2	0.17 ± 0.01	0.47 ± 0.01	0.70 – 0.04
J2021+4026	g	2	...	0.48 ± 0.01	...
J2032+4127	g	2	0.15 ± 0.01	0.50 ± 0.01	0.60 – 0.92
J2043+2740	r	2	0.20 ± 0.01	0.36 ± 0.01	0.64 – 0.08
J2124−3358	m	1	0.86 ± 0.02	...	0.92 – 0.58
J2229+6114	r	1	0.49 ± 0.01	...	0.64 – 0.14

Table 3—Continued

PSR	Type[a]	Peak multiplicity	Radio lag δ	γ-ray peak separation Δ	Off-pulse definition ϕ
J2238+59	g	2	...	0.50 ± 0.01	0.60 – 0.92

[a] Types are r=radio-selected, g=gamma-ray-selected, m=millisecond

[b] For some pulse profiles the current dataset does not allow clear discrimination between a single, broad pulse and two unresolved pulses. See the discussion in Weltevrede et al. (2010) regarding PSRs J1420−6048 and J1509−5850.

Note. — Light curve shape parameters evaluated from the full energy range light curve (see Section 2.1.3). These include the peak multiplicity (3rd column), the lag δ of the first gamma peak from the main radio peak for the radio-detected pulsars (4th column), and the phase difference Δ between the main gamma-ray peaks (5th column). Column 6 lists the off-pulse phase range used in the spectral analysis. The boldface entries for PSR J1124-5916 are the corrected values as per an Erratum sent to the ApJ in December 2010.

Table 4. Spectral fitting results for LAT-detected pulsars

PSR	Type[a]	Photon Flux (F_{100}) (10^{-8} ph cm^{-2} s^{-1})	Energy Flux (G_{100}) (10^{-11} erg cm^{-2} s^{-1})	Γ	$E_{\rm cutoff}$ (GeV)	TS	TS$_{\rm cutoff}$	Luminosity (10^{33} erg s^{-1})	Efficiency[b] ($f_\Omega = 1$)
J0007+7303	g	30.7 ± 1.3	38.2 ± 1.3	1.38 ± 0.05	4.6 ± 0.4	7384	274.7	89 ± 38	0.20 ± 0.08
J0030+0451	m	5.83 ± 0.78	5.26 ± 0.42	1.22 ± 0.19	1.8 ± 0.4	960	59.2	0.57 ± 0.35	0.17 ± 0.10
J0205+6449	r	13.2 ± 2.0	6.64 ± 0.65	2.09 ± 0.17	3.5 ± 1.4	346	12.5	54 – 81	0.002 – 0.003
J0218+4232	m	6.2 ± 1.7	3.62 ± 0.64	2.02 ± 0.28	5.1 ± 4.2	119	4.7	27 – 69	0.11 – 0.29
J0248+6021	r	3.7 ± 1.8	3.07 ± 0.70	1.15 ± 0.59	1.4 ± 0.6	103	18.5	15 – 300	0.07 – 1.4
J0357+32	g	10.4 ± 1.2	6.38 ± 0.44	1.29 ± 0.22	0.9 ± 0.2	949	71.6	···	···
J0437−4715	m	3.65 ± 0.84	1.86 ± 0.26	1.74 ± 0.38	1.3 ± 0.7	172	9.9	0.054 ± 0.008	0.02 ± 0.003
J0534+2200[c]	r	209 ± 4	130.6 ± 3.4	1.97 ± 0.02	5.8 ± 0.5	21507	80.2	620 ± 310	0.001 ± 0.001
J0613−0200	m	3.38 ± 0.85	3.23 ± 0.42	1.38 ± 0.29	2.7 ± 1.0	285	18.5	$0.89^{+0.71}_{-0.42}$	$0.07^{+0.06}_{-0.03}$
J0631+1036	r	2.8 ± 1.2	3.04 ± 0.61	1.38 ± 0.42	3.6 ± 1.8	86	10.0	2.0 – 48	0.01 – 0.27
J0633+0632	g	8.4 ± 1.4	8.0 ± 0.77	1.29 ± 0.22	2.2 ± 0.6	370	50.8	···	···
J0633+1746	g	305.3 ± 3.5	338.1 ± 3.5	1.08 ± 0.02	1.9 ± 0.05	62307	5120.4	25^{+24}_{-12}	$0.78^{+0.74}_{-0.38}$
J0659+1414	r	10 ± 1.4	3.17 ± 0.36	2.37 ± 0.50	0.7 ± 0.5	206	6.9	0.31 ± 0.08	0.01 ± 0.002
J0742−2822	r	3.18 ± 1.2	1.82 ± 0.42	1.76 ± 0.48	2.0 ± 1.4	47	4.2	9.0^{+12}_{-9}	$0.07^{+0.09}_{-0.07}$
J0751+1807	m	1.35 ± 0.66	1.09 ± 0.38	1.56 ± 0.70	3.0 ± 4.3	37	3.8	$0.47^{+1}_{-0.35}$	$0.08^{+0.17}_{-0.06}$
J0835−4510	r	1061 ± 7.0	879.4 ± 5.4	1.57 ± 0.01	3.2 ± 0.1	219585	5971.0	87 ± 12	0.01 ± 0.002
J1028−5819	r	19.6 ± 3.1	17.7 ± 1.4	1.25 ± 0.20	1.9 ± 0.5	620	75.1	120 ± 73	0.14 ± 0.09
J1048−5832	r	19.7 ± 3.0	17.2 ± 1.3	1.31 ± 0.18	2.0 ± 0.4	881	81.8	150 ± 90	0.08 ± 0.05
J1057−5226	r	30.45 ± 1.7	27.2 ± 0.98	1.06 ± 0.10	1.3 ± 0.1	4961	366.3	17 ± 9	0.56 ± 0.31
J1124−5916	r	5.2 ± 1.8	3.79 ± 0.70	1.43 ± 0.40	1.7 ± 0.7	111	16.7	100^{+34}_{-53}	$0.01^{+0.003}_{-0.004}$
J1418−6058	g	27.7 ± 8.3	23.5 ± 3.8	1.32 ± 0.24	1.9 ± 0.4	162	54.1	110 – 700	0.02 – 0.14
J1420−6048	r	24.2 ± 7.9	15.8 ± 3.5	1.73 ± 0.24	2.7 ± 1.0	63	21.4	590 ± 380	0.06 ± 0.04
J1459−60	g	17.8 ± 3.4	10.56 ± 1.2	1.83 ± 0.24	2.7 ± 1.1	337	21.1	···	···
J1509−5850	r	8.7 ± 1.4	9.7 ± 1.2	1.36 ± 0.28	3.5 ± 1.1	262	26.3	78 ± 49	0.15 ± 0.10
J1614−2230	m	2.89 ± 1.2	2.74 ± 0.50	1.34 ± 0.43	2.4 ± 1.0	149	13.3	5.3 ±3.4	1.0 ± 0.7
J1709−4429	r	149.8 ± 4.1	124 ± 2.6	1.70 ± 0.04	4.9 ± 0.4	16009	373.6	290 – 1900	0.09 – 0.57
J1718−3825	r	9.1 ± 5.8	6.7 ± 1.9	1.26 ± 0.74	1.3 ± 0.6	105	19.7	120 ± 80	0.09 ± 0.06
J1732−31	g	25.3 ± 3.0	24.2 ± 1.4	1.27 ± 0.14	2.2 ± 0.3	1002	131.2	···	···
J1741−2054	g	20.3 ± 2.0	12.8 ± 0.8	1.39 ± 0.17	1.2 ± 0.2	935	92.6	2.2 ± 1.3	0.24 ± 0.14
J1744−1134	m	4.3 ± 1.6	2.8 ± 0.6	1.02 ± 0.71	0.7 ± 0.4	78	20.0	0.43 ± 0.13	0.1 ± 0.03
J1747−2958	r	18.2 ± 4.2	13.1 ± 1.7	1.11 ± 0.34	1.0 ± 0.2	213	59.3	63 – 390	0.02 – 0.16
J1809−2332	g	49.5 ± 3.0	41.3 ± 1.6	1.52 ± 0.07	2.9 ± 0.3	3451	201.9	140 ± 140	0.33 ± 0.33
J1813−1246	g	28.1 ± 3.5	16.9 ± 1.3	1.83 ± 0.14	2.9 ± 0.8	482	39.7	···	···
J1826−1256	g	41.8 ± 4.1	33.4 ± 1.8	1.49 ± 0.11	2.4 ± 0.3	1152	138	···	···

Table 4—Continued

PSR	Type[a]	Photon Flux (F_{100}) (10^{-8} ph cm^{-2} s^{-1})	Energy Flux (G_{100}) (10^{-11} erg cm^{-2} s^{-1})	Γ	$E_{\rm cutoff}$ (GeV)	TS	TS$_{\rm cutoff}$	Luminosity (10^{33} erg s^{-1})	Efficiency[b] ($f_\Omega = 1$)
J1833−1034	r	20.5 ± 4.6	10.1 ± 1.4	2.24 ± 0.18	7.7 ± 4.8	110	4.9	270 ± 60	0.01 ± 0.002
J1836+5925[d]	g	65.6 ± 1.8	59.9 ± 1.3	1.35 ± 0.04	2.3 ± 0.1	20982	674.6	<46	<4.0
J1907+06	g	40.25 ± 3.8	27.5 ± 1.6	1.84 ± 0.10	4.6 ± 1.0	1209	59.3	...	...
J1952+3252	r	17.6 ± 1.9	13.4 ± 0.9	1.75 ± 0.12	4.5 ± 1.2	1008	36.4	64 ± 32	0.02 ± 0.01
J1958+2846	g	7.65 ± 1.6	8.45 ± 0.83	0.77 ± 0.31	1.2 ± 0.2	491	89.2	...	...
J2021+3651	r	67.35 ± 4.4	47.0 ± 1.8	1.65 ± 0.07	2.6 ± 0.3	3138	223.5	250^{+500}_{-240}	$0.07^{+0.15}_{-0.07}$
J2021+4026[d]	g	152.6 ± 4.9	97.6 ± 2.0	1.79 ± 0.04	3.0 ± 0.2	10180	331.4	260 ± 150	2.2 ± 1.3
J2032+4127	g	6 ± 2.3	11.1 ± 1.4	0.68 ± 0.46	2.1 ± 0.6	487	56.3	34 – 170	0.13 – 0.64
J2043+2740	r	2.41 ± 0.90	1.55 ± 0.32	1.07 ± 0.66	0.8 ± 0.3	79	15.1	6.0 ± 3.8	0.09 ± 0.06
J2124−3358	m	1.95 ± 0.49	2.75 ± 0.42	1.05 ± 0.34	2.7 ± 1.0	226	22.9	$0.21^{+0.42}_{-0.14}$	$0.05^{+0.11}_{-0.04}$
J2229+6114	r	32.6 ± 2.2	22.0 ± 1.0	1.74 ± 0.08	3.0 ± 0.5	1929	96.0	17 – 1100	0.001 – 0.05
J2238+59	g	6.8 ± 1.8	5.44 ± 0.71	1.00 ± 0.43	1.0 ± 0.3	219	37.2	...	...

[a] Types are r=radio-selected, g=gamma-ray-selected, m=millisecond.

[b] Here, f_Ω is assumed to be 1, which can result in an efficiency > 1.

[c] For the Crab the spectral parameters come from Abdo et al. (2010d).

[d] For J1836+5925 and J2021+4026 the spectral parameters come from the phase-averaged analysis (see Section 2.2).

Note. — Results of the unbinned maximum likelihood spectral fits for the LAT gamma-ray pulsars (see Section 2.2). Columns 3 and 4 list the on-pulse photon flux F_{100} and on-pulse energy flux G_{100} respectively. The fits used an exponentially cutoff power-law model (see Eq. 4) with photon index Γ and cutoff energy $E_{\rm cutoff}$ given in columns 5 and 6. The systematic uncertainties on F_{100}, G_{100}, and Γ due to uncertainties in the Galactic diffuse emission model have been added in quadrature with the statistical errors. Uncertainties in the instrument response induce additional biases of $\delta F_{100} = (+30\%, -10\%)$, $\delta G_{100} = (+20\%, -10\%)$, $\delta\Gamma = (+0.3, -0.1)$, and $\delta E_{\rm cutoff} = (+20\%, -10\%)$. The test statistic ($TS$) for the source significance is provided in column 7. The significance of an exponential cutoff (as compared to a simple power-law) is indicated by $TS_{\rm cutoff}$ in column 8, where a value < 10 indicates that the two models are comparable. The total gamma-ray luminosity L_γ and the resulting calculated gamma-ray conversion efficiency $\eta_\gamma \equiv L_\gamma/\dot{E}$ (where $f_\Omega = 1$ as described in Section 3.2) are listed in columns 9 and 10, respectively. The uncertainties in L_γ and η include the flux and distance uncertainties. Nevertheless, the strong dependence of these variables on the measured distance (see Table 5) and beaming factor means that they should be considered with care.

Table 5. Pulsar distance estimates

Pulsar Name	Distance (kpc)	Method[a]	(Ref[b])
J0007+7303	1.4±0.3	K	(30)
J0030+0451	0.300±0.090	P	(23)
J0205+6449	2.6–3.2	K	(14,32)
J0218+4232	2.5–4	O	(1)
J0248+6021	2–9	O	(6)
J0437−4715	0.1563±0.0013	P	(9)
J0534+2200	2.0±0.5	O	(35)
J0613−0200	$0.48^{+0.19}_{-0.11}$	P	(18)
J0631+1036	0.75–3.62	O	(39)
J0633+1746	$0.250^{+0.120}_{-0.062}$	P	(11)
J0659+1414	$0.288^{+0.033}_{-0.027}$	P	(2)
J0742−2822	$2.07^{+1.38}_{-1.07}$	DM	(33)
J0751+1807	$0.6^{+0.6}_{-0.2}$	P	(28)
J0835−4510	$0.287^{+0.019}_{-0.017}$	P	(10)
J1028−5819	2.33±0.70	DM	(19)
J1048−5832	2.71±0.81	DM	(21)
J1057−5226	0.72 ±0.2	DM	(37)
J1124−5916	$4.8^{+0.7}_{-1.2}$	O	(13)
J1418−6058	2–5	O	(27,38)
J1420−6048	5.6±1.7	DM	(8)
J1509−5850	2.6±0.8	DM	(24)
J1614−2230	1.27±0.39	DM	(7)
J1709−4429	1.4–3.6	O	(26,33)
J1718−3825	3.82±1.15	DM	(25)
J1741−2054	0.38±0.11	DM	(3)
J1744−1134	$0.357^{+0.043}_{-0.035}$	P	(34)
J1747−2958	2–5	O	(5,12)
J1809−2332	1.7±1.0	K	(29)
J1833−1034	4.7±0.4	K	(4)
J1836+5925	<0.8	O	(16)
J1952+3252	2.0±0.5	K	(15)
J2021+3651	$2.1^{+2.1}_{-1.0}$	O	(36)
J2021+4026	1.5±0.45	K	(22)
J2032+4127	1.6–3.6	O	(3)
J2043+2740	1.80±0.54	DM	(31)
J2124−3358	$0.25^{+0.25}_{-0.08}$	P	(18)
J2229+6114	0.8–6.5	O	(17,20)

[a] K distance evaluation from kinematic model; P from parallax; DM from dispersion measure using the Cordes & Lazio (2002) model; O from other measurements. For DM measurements, we assume a minimum distance uncertainty of 30%, as discussed in Section 3.1.

[b] For DM, the reference gives the DM measurement.

Note. — The best known distances of 37 pulsars detected by *Fermi*. Nine of the pulsars in the catalog have no distance estimate and are not included in this table.

References. — (1) Bassa et al. (2003); (2) Brisken et al. (2003); (3) Camilo et al. (2009); (4) Camilo et al. (2006); (5) Camilo et al. (2002b); (6) Cognard et al. (2010); (7) Crawford et al. (2006); (8) D'Amico et al. (2001); (9) Deller et al. (2008); (10) Dodson et al. (2003); (11) Faherty et al. (2007); (12) Gaensler et al. (2004); (13) Gonzalez & Safi-Harb (2003); (14) Green & Gull (1982); (15) Greidanus & Strom (1990); (16) Halpern et al. (2007); (17) Halpern et al. (2001a); (18) Hotan et al. (2006); (19) Keith et al. (2008); (20) Kothes et al. (2001); (21) Johnston et al. (1996); (22) Landecker et al. (1980); (23) Lommen et al. (2006); (24) Manchester et al. (2005); (25) Manchester et al. (2001); (26) McGowan et al. (2004); (27) Ng et al. (2005); (28) Nice et al. (2005); (29) Oka et al. (1999); (30) Pineault et al. (1993); (31) Ray et al. (1996); (32) Roberts et al. (1993); (33) Taylor et al. (1993); (34) Toscano et al. (1999); (35) Trimble (1973); (36) Van Etten et al. (2008); (37) Weltevrede & Wright (2009); (38) Yadigaroglu & Romani (1997); (39) Zepka et al. (1996)

Table 6. Positional associations with known GeV and TeV sources for LAT-detected pulsars

PSR	Alt. name	LAT BSL association[a]	GeV associations[b]	Other associations
J0007+7303	···	0FGL J0007.4+7303	3EG J0010+7309 EGR J0008+7308 GEV J0008+7304 1AGL J0006+7311	SNR CTA 1 [2] PWN G119.5+10.2 [1]
J0030+0451	···	0FGL J0030.3+0450	EGR J0028+0457	···
J0205+6449	···	···	···	SNR/PWN 3C 58 [2] PWN G119.5+10.2 [1]
J0218+4232	···	···	···	···
J0248+6021	···	···	···	···
J0357+32	···	0FGL J0357.5+3205	···	···
J0437−4715	···	···	···	PWN G253.4−42.0 [1]
J0534+2200	Crab PSR B0531+21	0FGL J0534.6+2201	3EG J0534+2200 EGR J0534+2159 GEV J0534+2159 1AGL J0535+2205	SNR/PWN G184.6−5.8 [1,2] HESS J0534+220 [4]
J0613−0200	···	0FGL J0613.9−0202	···	···
J0631+1036	···	0FGL J0631.8+1034	···	···
J0633+0632	···	0FGL J0633.5+0634	3EG J0631+0642 EGR J0633+0646 GEV J0633+0645	···
J0633+1746	Geminga	0FGL J0634.0+1745	3EG J0633+1751 EGR J0633+1750 GEV J0634+1746 1AGL J0634+1748	PWN G195.1+4.3 [1] MGRO J0632+17 [3,11]
J0659+1414	PSR B0656+14	···	···	SNR 203.0+12.0
J0742−2822	PSR B0740−28	···	···	···
J0751+1807	···	···	···	···
J0835−4510	Vela PSR B0833−45	0FGL J0835.4−4510	3EG J0834−4511 EGR J0834−4512 GEV J0835−4512 1AGL J0835−4509	SNR/PWN G263.9−3.3 [1,2] HESS J0835−455 [5]
J1028−5819	···	0FGL J1028.6−5817	3EG J1027−5817 GEV J1025−5809	···
J1048−5832	PSR B1046−58	0FGL J1047.6−5834	3EG J1048−5840 EGR J1048−5839 GEV J1047−5840	PWN G287.4+0.58 [1]
J1057−5226	PSR B1055−52	0FGL J1058.1−5225	3EG J1058−5234 EGR J1058−5221 GEV J1059−5218 1AGL J1058−5239	···
J1124−5916	···	···	···	MSH 11−54 SNR/PWN G292.0+1.8 [1,2]
J1418−6058	···	0FGL J1418.8−6058	3EG J1420−6038 GEV J1417−6100 1AGL J1419−6055	PWN G313.3+0.1 [1] HESS J1418−609 [6]
J1420−6048	···	···	3EG J1420−6038	PWN G313.6+0.3 [1]

Table 6—Continued

PSR	Alt. name	LAT BSL association[a]	GeV associations[b]	Other associations
			EGR J1418−6040 GEV J1417−6100 1AGL J1419−6055	HESS J1420−607 [6]
J1459−60	···	0FGL J1459.4−6056	···	···
J1509−5850[c]	···	0FGL J1509.5−5848	1AGL J1506−5859	PWN G319.97−0.62 [1]
J1614−2230	···	···	3EG J1616−2221	···
J1709−4429	PSR B1706−44	0FGL J1709.7−4428	3EG J1710−4439 EGR J1710−4435 GEV J1709−4430 1AGL J1709−4428	SNR/PWN G343.1−2.3 [1,2] HESS J1708−443 [7]
J1718−3825	···	···	···	HESS J1718−385 [8]
J1732−31	···	0FGL J1732.8−3135	3EG J1734−3232 EGR J1732−3126 GEV J1732−3130	···
J1741−2054	···	0FGL J1742.1−2054	3EG J1741−2050	···
J1744−1134	···	···	···	···
J1747−2958	···	···	1AGL J1746−3017	PWN G359.23−0.82 [1]
J1809−2332	···	0FGL J1809.5−2331	3EG J1809−2328 GEV J1809−2327 1AGL J1809−2333	PWN G7.4−2.0 [1]
J1813−1246	···	0FGL J1813.5−1248	GEV J1814−1228	···
J1826−1256	···	0FGL J1825.9−1256	3EG J1826−1302 GEV J1825−1310 1AGL J1827−1277	PWN G18.5−0.4 [1]
J1833−1034	···	···	···	SNR/PWN G21.5−0.9 [1,2] HESS J1833−105 [9]
J1836+5925	···	0FGL J1836.2+5924	3EG J1835+5918 GEV J1835+5921 1AGL J1836+5923	···
J1907+06	···	0FGL J1907.5+0602	GEV J1907+0557 1AGL J1908+0613	MGRO J1908+063 [3] HESS J1908+06 [10]
J1952+3252[d]	PSR B1951+32	0FGL J1953.2+3249	···	SNR CTB 80 [2] PWN G69.0+2.7 [1]
J1958+2846	···	0FGL J1958.1+2848	3EG J1958+2909 GEV J1957+2859	···
J2021+3651	···	0FGL J2020.8+3649	GEV J2020+3658 1AGL J2021+3652	PWN G75.2+0.1 [1] MGRO J2019+37 [3]
J2021+4026	···	0FGL J2021.5+4026	3EG J2020+4017 1AGL J2021+3652	SNR γ Cygni [2] SNR G78.2+2.1 [2]
J2032+4127	···	0FGL J2032.2+4122	3EG J2033+4118 EGR J2033+4117 1AGL J2032+4102	MGRO J2031+41 [3]
J2043+2740	···	···	···	···
J2124−3358	···	0FGL J2124.7−3358	···	PWN G10.9−45.4 [1]
J2229+6114	···	0FGL J2229.0+6114	3EG J2227+6122 EGR J2227+6114	PWN G106.6+2.9 [1] MGRO J2228+61 [3,11]

Table 6—Continued

PSR	Alt. name	LAT BSL association[a]	GeV associations[b]	Other associations
			GEV J2227+6101 1AGL J2231+6109	
J2238+59	···	···	···	···

[a] Source designator from the LAT Bright Source List (Abdo et al. 2009i).

[b] Source designator(s) from the 3rd EGRET (3EG: Hartman et al. 1999), Revised EGRET (EGR: Casandjian & Grenier 2008), High-energy EGRET (GEV Lamb & Macomb 1997) and/or the first AGILE (1AGL: Pittori et al. 2009) catalogs.

[c] PSR J1509−5850 should not be confused with PSR B1509−58 observed by *CGRO* (Kuiper et al. 1999).

[d] While pulsations from PSR J1952+3252 were detected in EGRET data, it was never cataloged as a point source.

Note. — Alternate names for the pulsars in this catalog are given in column 2. Positional associations with SNRs, PWNe and selected TeV sources are provided in column 5.

References. — 1. Roberts et al. (2005), 2. Green (2009), 3. Abdo et al. (2009k), 4. Aharonian et al. (2006c), 5. Aharonian et al. (2006b), 6. Aharonian et al. (2006a), 7. Hoppe et al. (2009), 8. Aharonian et al. (2007), 9. Djannati-Ataï et al. (2007), 10. Aharonian et al. (2009), 11. Goodman & Sinnis (2009) .

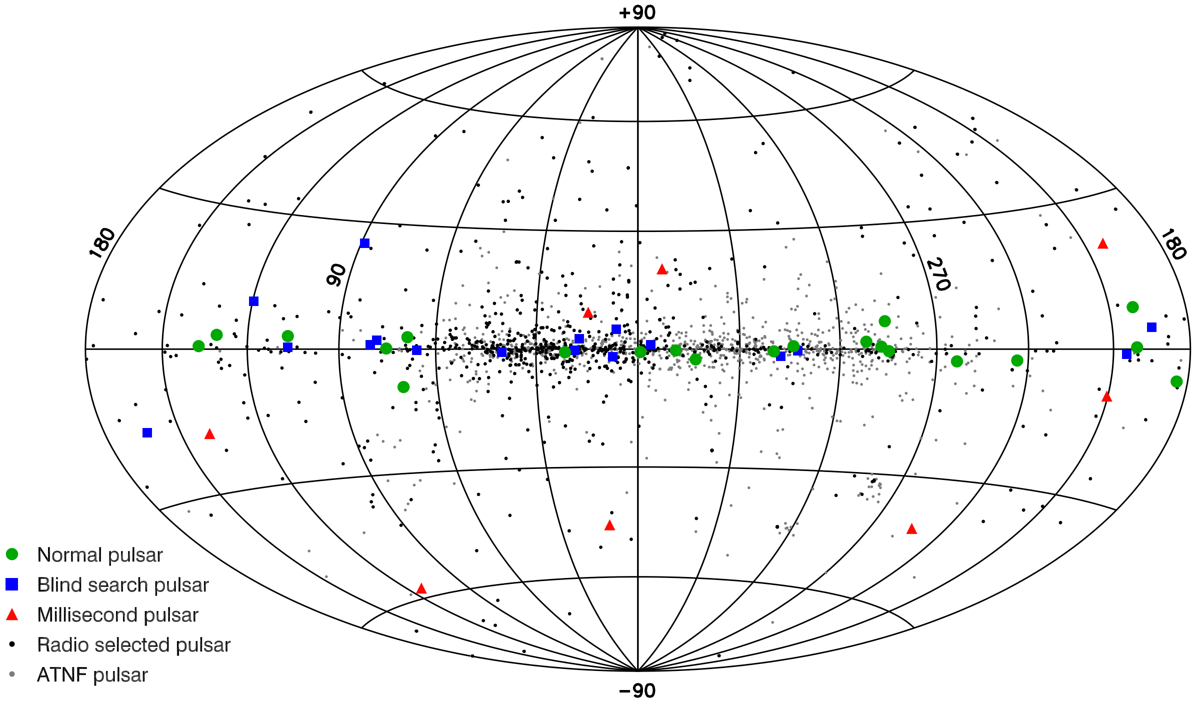

Fig. 1.— Pulsar sky map in Galactic coordinates. Blue squares: gamma-ray-selected pulsars. Red triangles: millisecond gamma-ray pulsars. Green circles: all other radio loud gamma-ray pulsars. Black dots: Pulsars for which gamma-ray pulsation searches were conducted using rotational ephemerides. Gray dots: Known pulsars which were not searched for pulsations.

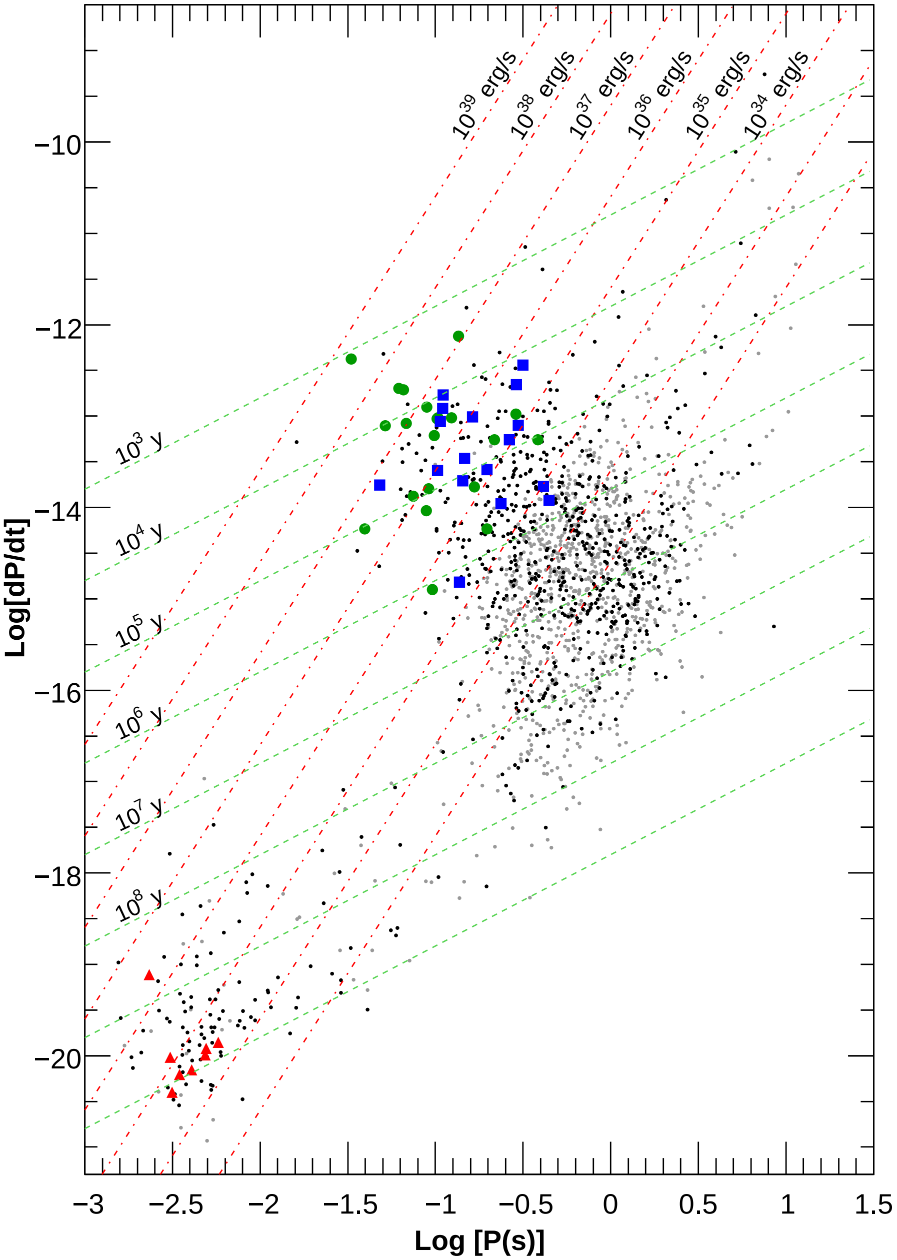

Fig. 2.— $P - \dot{P}$ diagram. Dashed lines: characteristic age τ_c. Dot-dashed lines: rotational energy loss rate $\dot{E}$. Blue squares: gamma-ray-selected pulsars. Red triangles: millisecond gamma-ray pulsars. Green circles: all other radio loud gamma-ray pulsars. Black dots: Pulsars for which gamma-ray pulsation searches were conducted using rotational ephemerides. Gray dots: Known pulsars which were not searched for pulsations.

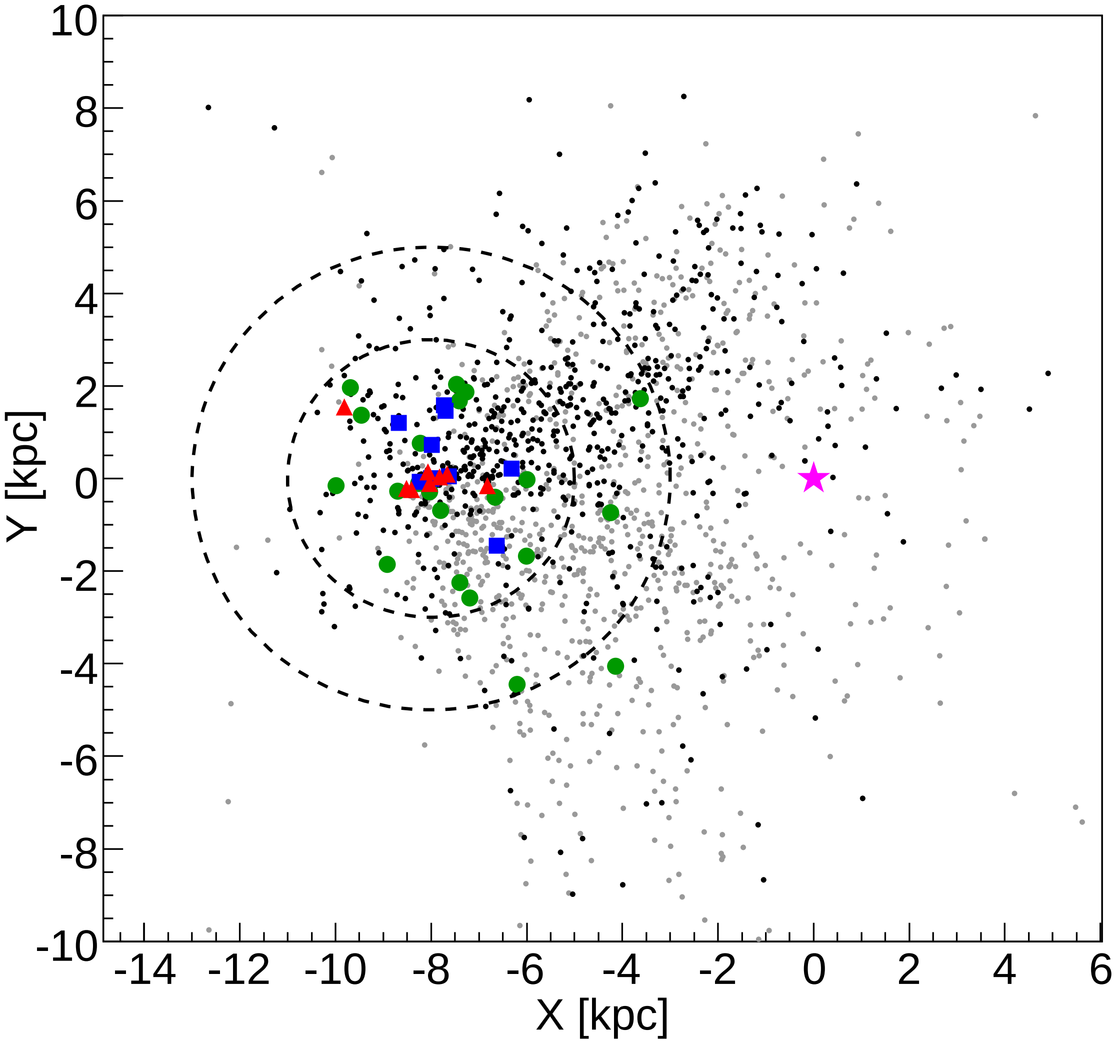

Fig. 3.— Galactic plane pulsar distribution (polar view). The star represents the Galactic center. The two circles centered at the Earth's position have radii of 3 kpc and 5 kpc. For pulsars with different possible distances, the nearer values from Table 5 are used. Note that the millisecond pulsars (MSPs), while having a significantly lower $\dot{E}$ than the other pulsars (see Figure 8), are detectable due to their close proximity. The one exception (PSR J0218+4232) also exhibits a significantly higher $\dot{E}$ than the other MSPs. Blue squares: gamma-ray-selected pulsars. Red triangles: millisecond gamma-ray pulsars. Green circles: all other radio loud gamma-ray pulsars. Black dots: Pulsars for which gamma-ray pulsation searches were conducted using rotational ephemerides. Gray dots: Known pulsars which were not searched for pulsations.

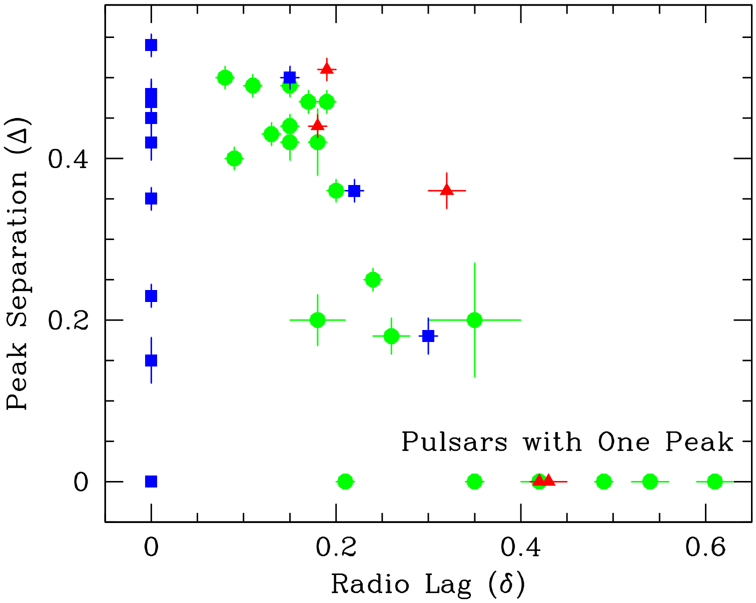

Fig. 4.— Phase difference Δ between the gamma-ray peaks, versus the phase lag δ between the main radio peak and the nearest gamma-ray peak. Pulsars without a radio detection are plotted with $\delta = 0$. With present light curves we cannot generally measure $\Delta < 0.15$; objects classified as single-peaked are plotted with Δ=0. Two such objects, both MSPs, are off the plot at $\delta > 0.8$. Blue squares: gamma-ray-selected pulsars. Red triangles: millisecond gamma-ray pulsars. Green circles: all other radio loud gamma-ray pulsars. The plot has been corrected for the updated value of δ for PSR J1124-5916, as per an Erratum sent to the ApJ (December 2010).

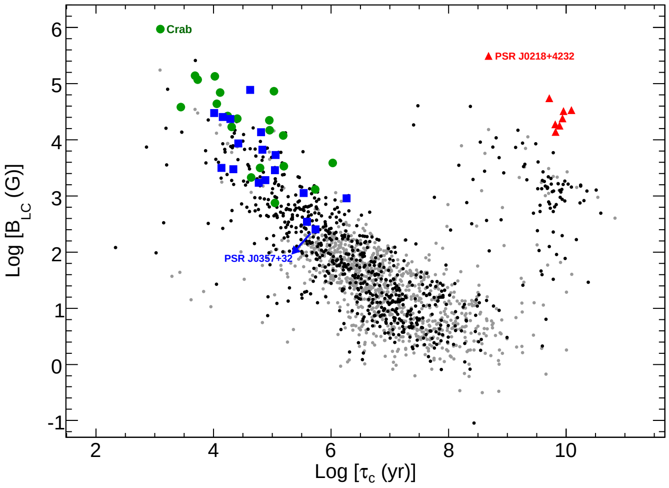

Fig. 5.— Magnetic field strength at the light cylinder $B_{\rm LC}$ versus pulsar characteristic age $\tau_{\rm c}$. Blue squares: gamma-ray-selected pulsars. Red triangles: millisecond gamma-ray pulsars. Green circles: all other radio loud gamma-ray pulsars. Black dots: Pulsars for which gamma-ray pulsation searches were conducted using rotational ephemerides. Gray dots: Known pulsars which were not searched for pulsations.

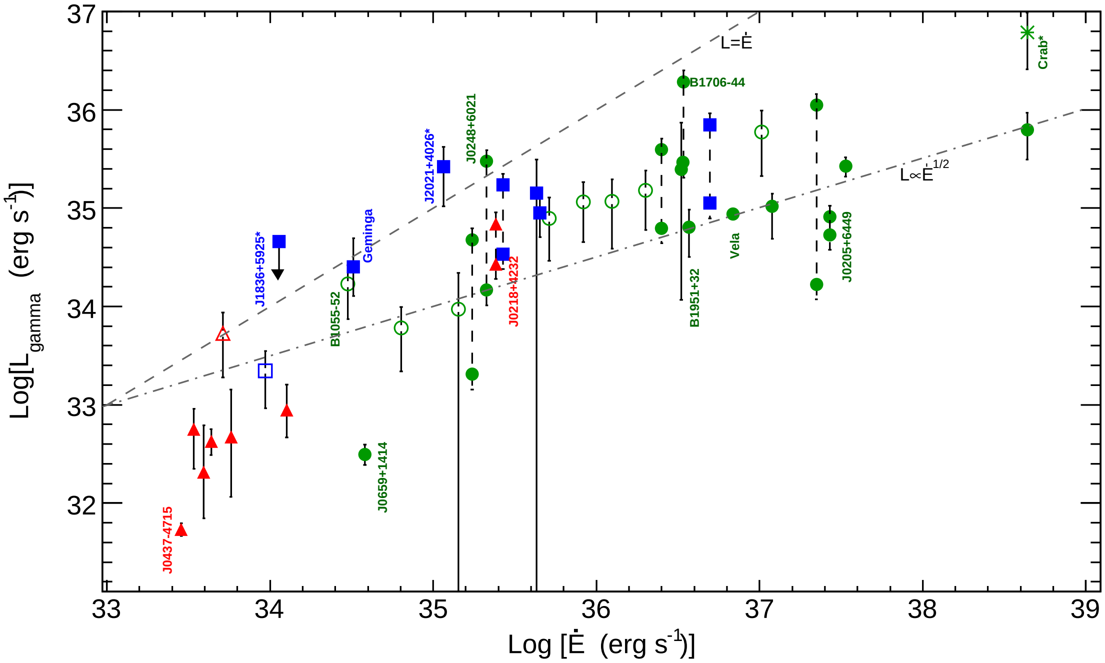

Fig. 6.— Gamma-ray luminosity L_γ versus the rotational energy loss rate $\dot{E}$. Dashed line: L_γ equal to $\dot{E}$. Dot-dashed line: L_γ proportional to the square root of $\dot{E}$. L_γ is calculated using a beam correction factor $f_\Omega = 1$ for all pulsars and the integral energy flux G_{100} from the on-pulse spectral analysis (see Section 2.2), except for PSRs J1836+5925 and J2021+4026 which use the total background-corrected phase-averaged flux, including a relatively bright unpulsed component (see Section 2.2). For the Crab we also plot the total high energy luminosity, $L_{\rm tot} = L_X + L_\gamma$, indicated by *. Several notable pulsars have been labeled. Blue squares: gamma-ray-selected pulsars. Red triangles: millisecond gamma-ray pulsars. Green circles: all other radio loud gamma-ray pulsars. Unfilled markers indicate pulsars for which only a DM-based distance estimate is available (see Table 5). Pulsars with two distance estimates have two markers connected with dashed error bars.

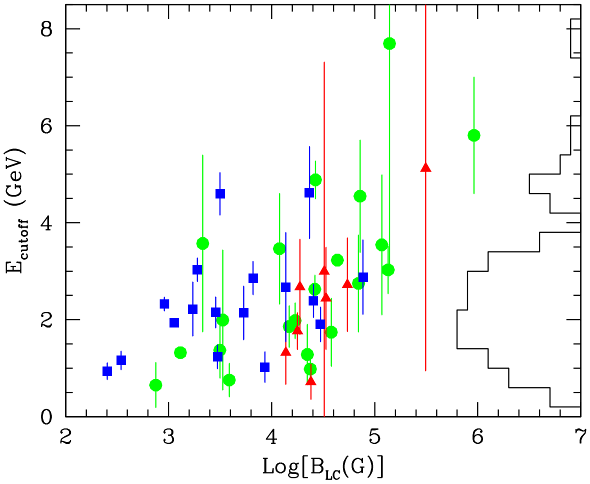

Fig. 7.— Value of the exponential cutoff $E_{\rm cutoff}$ versus the magnetic field at the light cylinder, $B_{\rm LC}$. The statistical uncertainties on $E_{\rm cutoff}$ are shown. An additional systematic bias of (+20%, −10%) may affect $E_{\rm cutoff}$ (see text). The histogram of $E_{\rm cutoff}$ values is projected along the right-hand axis. Blue squares: gamma-ray-selected pulsars. Red triangles: millisecond gamma-ray pulsars. Green circles: all other radio loud gamma-ray pulsars.

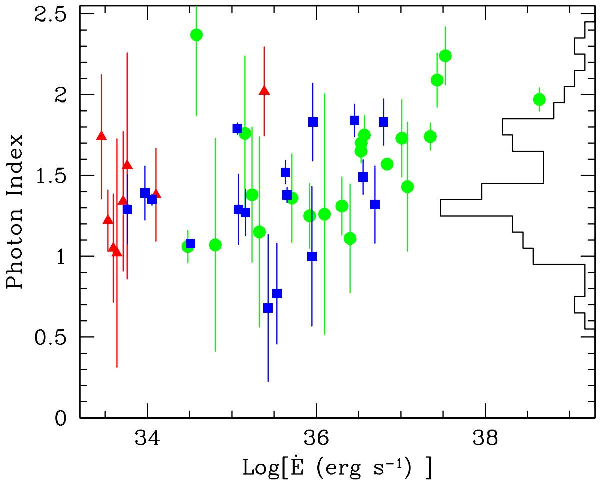

Fig. 8.— Photon index Γ versus the rotational energy loss rate, $\dot{E}$. For Γ, the statistical uncertainties combined with the systematic uncertainties due to the diffuse emission model are shown. An additional systematic bias of (+0.3, −0.1) affects Γ (see text). The histogram of the photon indices is projected along the right-hand axis. Blue squares: gamma-ray-selected pulsars. Red triangles: millisecond gamma-ray pulsars. Green circles: all other radio loud gamma-ray pulsars.

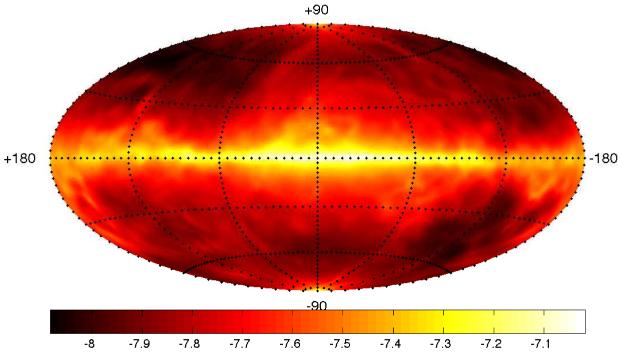

Fig. 9.— Aitoff projection sky map of the 5σ sensitivity in units of logarithmic **photon** flux ($\text{Log}(L_\gamma)$ ph $\text{cm}^{-2}\,\text{s}^{-1}$) for six months of *Fermi* LAT sky-survey data. The sensitivity analysis uses the model of the diffuse gamma-ray background described in the text (Section 4), and pulsar spectra with differential photon indices of $\Gamma = 1.4$ with an exponential cutoff energy of $E_{\text{cutoff}} = 2.2$ GeV.

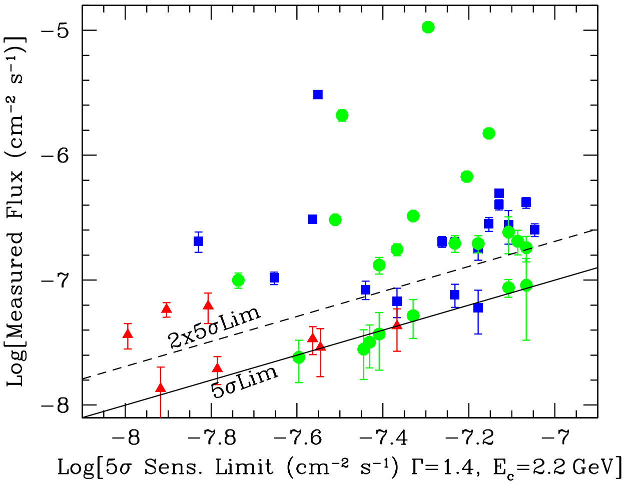

Fig. 10.— Measured integral photon flux above 100 MeV, F_{100}, versus the 5σ flux sensitivity described in Figure 9. For F_{100}, the statistical uncertainties combined with the systematic uncertainties due to the diffuse emission model are shown. An additional systematic bias of (+30%, −10%) affects F_{100} (see text). The effective blind search sensitivity is comparable to the $2 \times 5\sigma$ line, although a few pulsars are discovered at lower flux, presumably due to favorable pulse profiles, spectra or local backgrounds. Blue squares: gamma-ray-selected pulsars. Red triangles: millisecond gamma-ray pulsars. Green circles: all other radio loud gamma-ray pulsars.

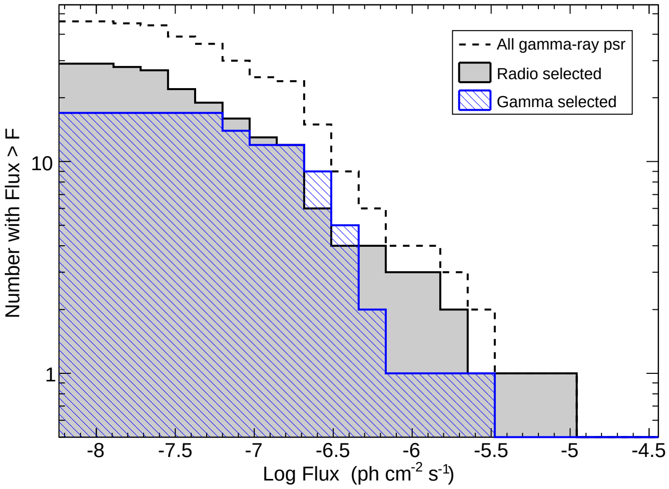

Fig. 11.— Log N–Log S distribution as described in Section 4 for all the detected pulsars (black dashed line), the radio-selected gamma-ray pulsars including MSPs (grey histogram), and the gamma-ray-selected pulsars (blue hatched histogram).

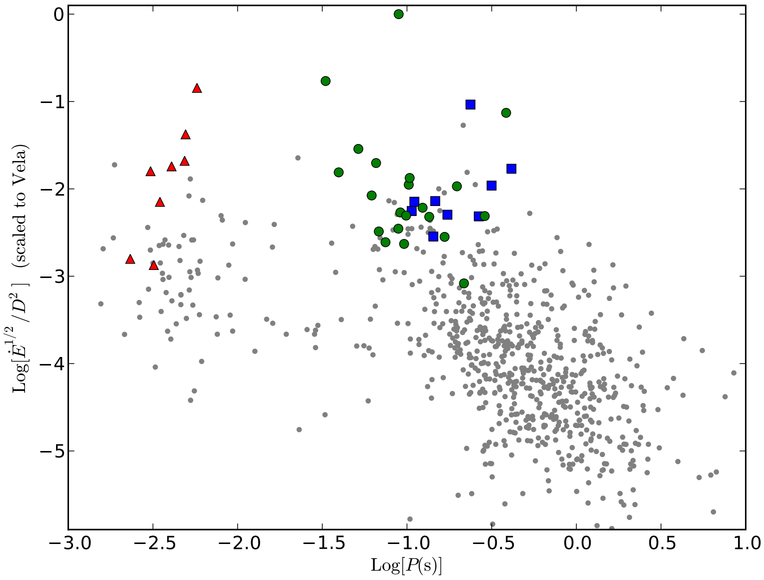

Fig. 12.— Pulsar "detectability" metric ($\dot{E}^{1/2}/d^2$, normalized to Vela) vs. spin period. Detected MSPs (red triangles) and young pulsars (radio-selected, green circles; gamma-ray-selected, blue squares) all have high values of this metric. For objects with a distance range in Table 5, we use here the geometric mean of the maximum and minimum values. Searched, but presently undetected objects (gray dots) are plotted using DM-derived distances. For the possible causes of non-detection see Section 5.1.

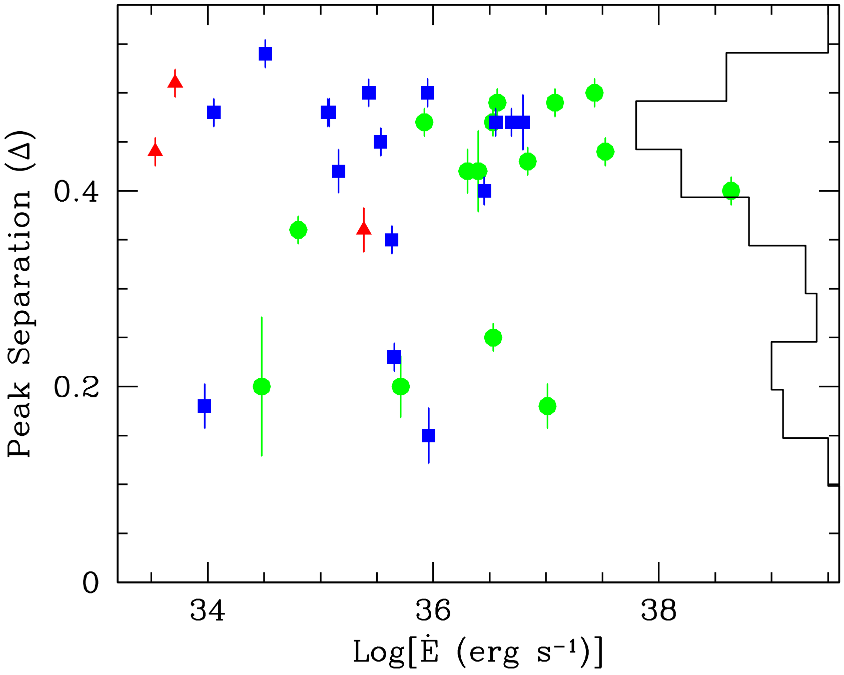

Fig. 13.— Separations Δ between the gamma-ray peaks, for those pulsars with two identified peaks, versus the spin-down power $\dot{E}$. The histogram of peak separations is projected along the right-hand axis. Blue squares: gamma-ray-selected pulsars. Red triangles: millisecond gamma-ray pulsars. Green circles: all other radio loud gamma-ray pulsars.

Appendix: Gamma-ray Pulsar Light Curves

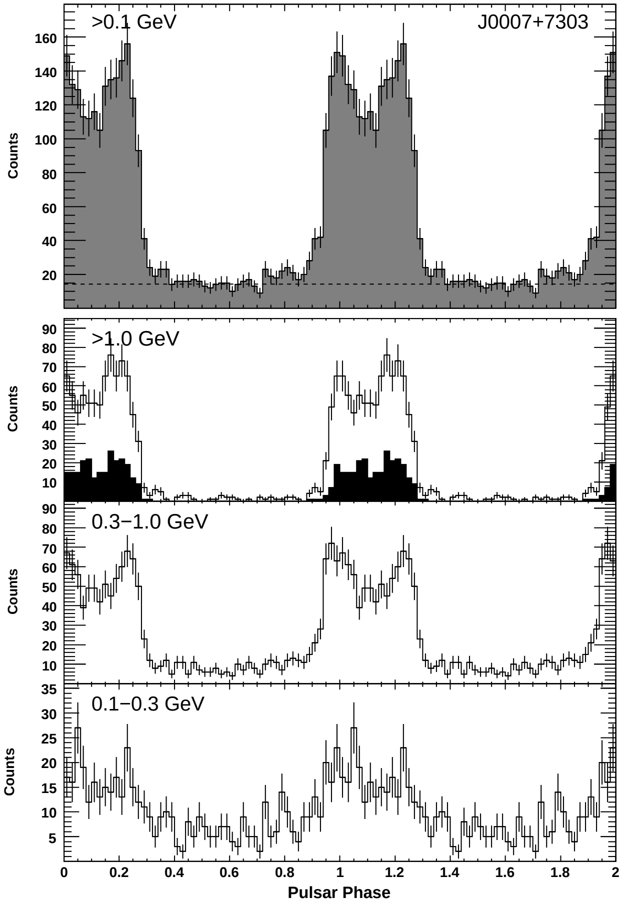

Fig. A-1.— Light curves for PSR J0007+7303 (P = 316 ms).

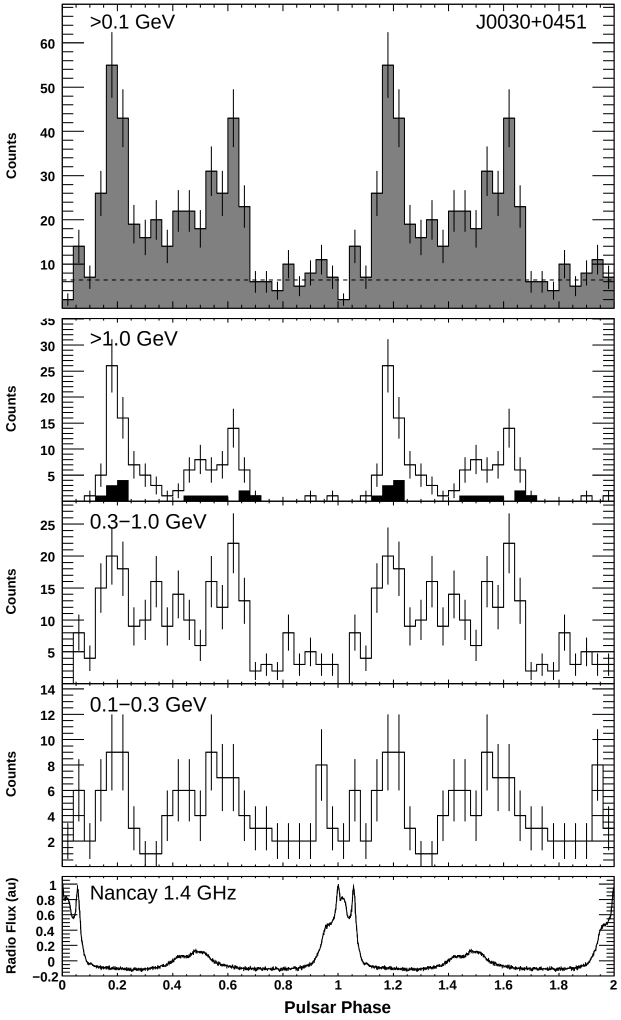

Fig. A-2.— Light curves for PSR J0030+0451 (P = 4.87 ms).

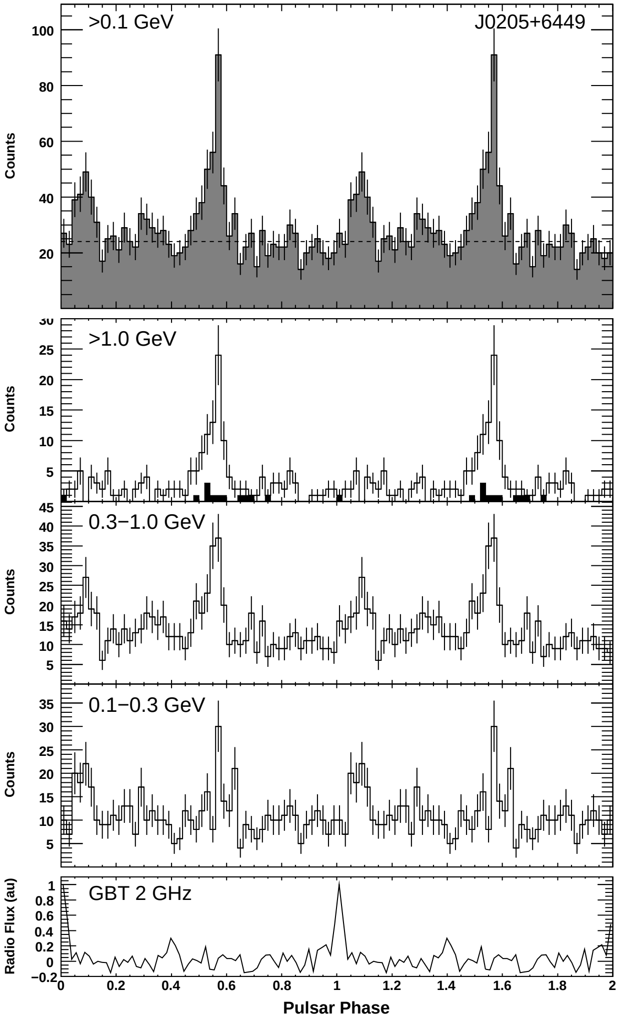

Fig. A-3.— Light curves for PSR J0205+6449 (P = 65.7 ms).

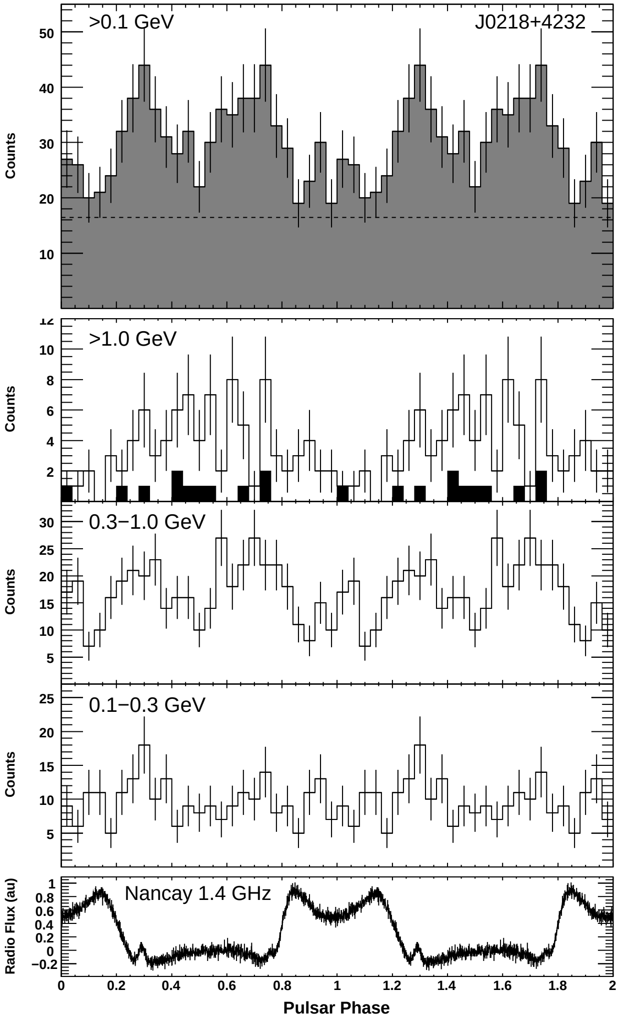

Fig. A-4.— Light curves for PSR J0218+4232 (P = 2.32 ms).

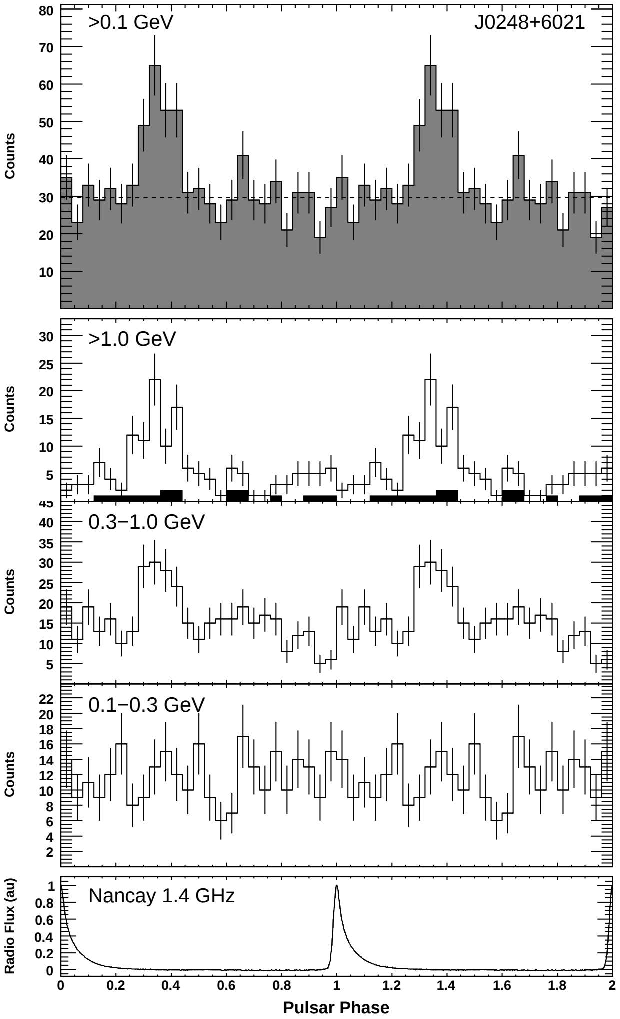

Fig. A-5.— Light curves for PSR J0248+6021 (P = 217 ms).

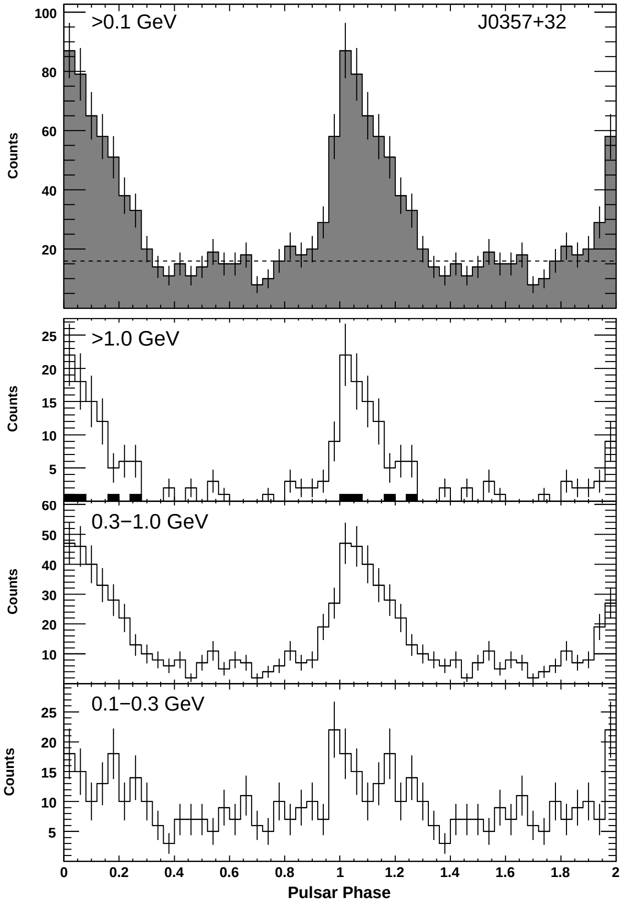

Fig. A-6.— Light curves for PSR J0357+32 ($P = 444$ ms).

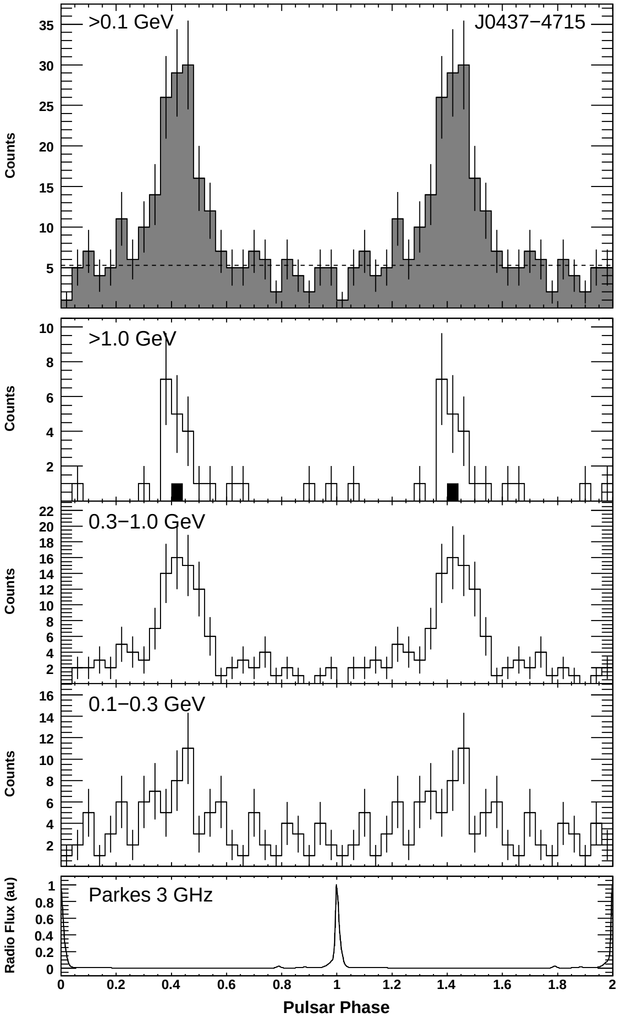

Fig. A-7.— Light curves for PSR J0437−4715 ($P = 5.76\,\mathrm{ms}$).

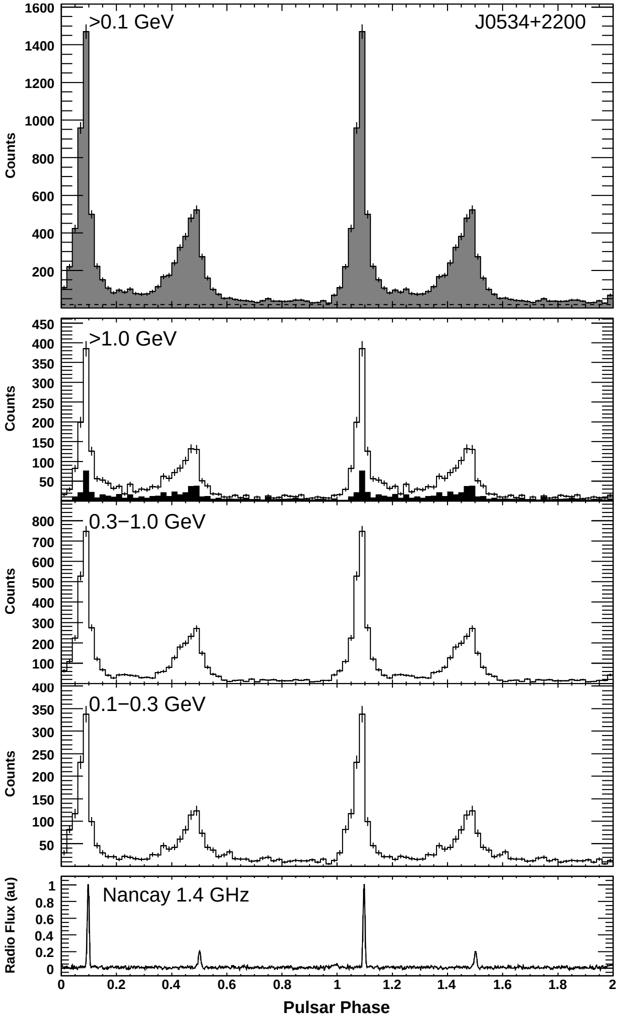

Fig. A-8.— Light curves for PSR J0534+2200 ($P = 33.1\,\mathrm{ms}$, Crab pulsar). The zero of phase is set to the radio precursor.

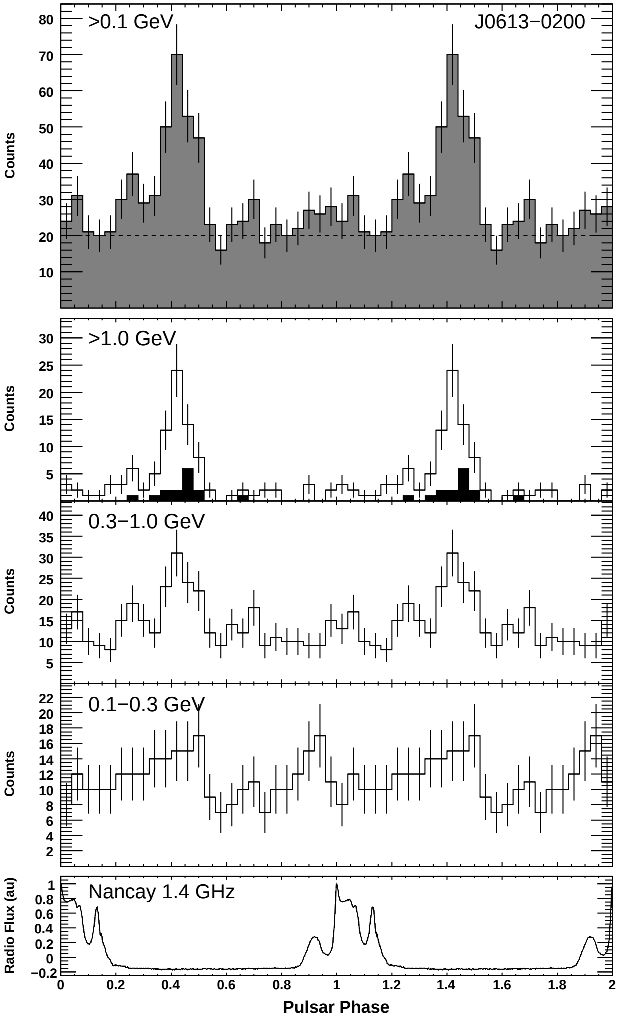

Fig. A-9.— Light curves for PSR J0613−0200 (P = 3.06 ms).

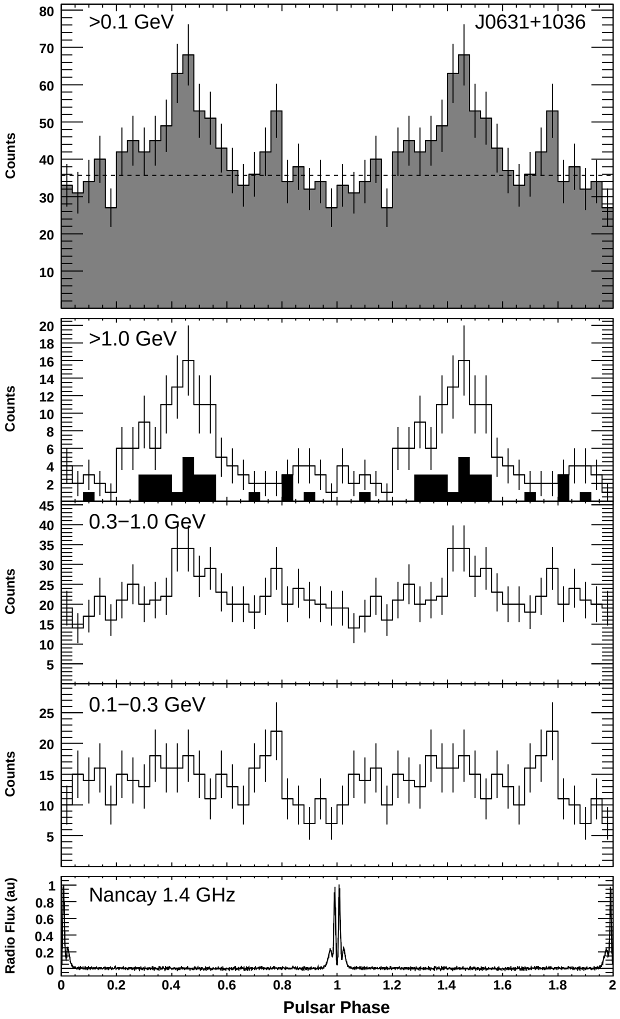

Fig. A-10.— Light curves for PSR J0631+1036 (P = 288 ms).

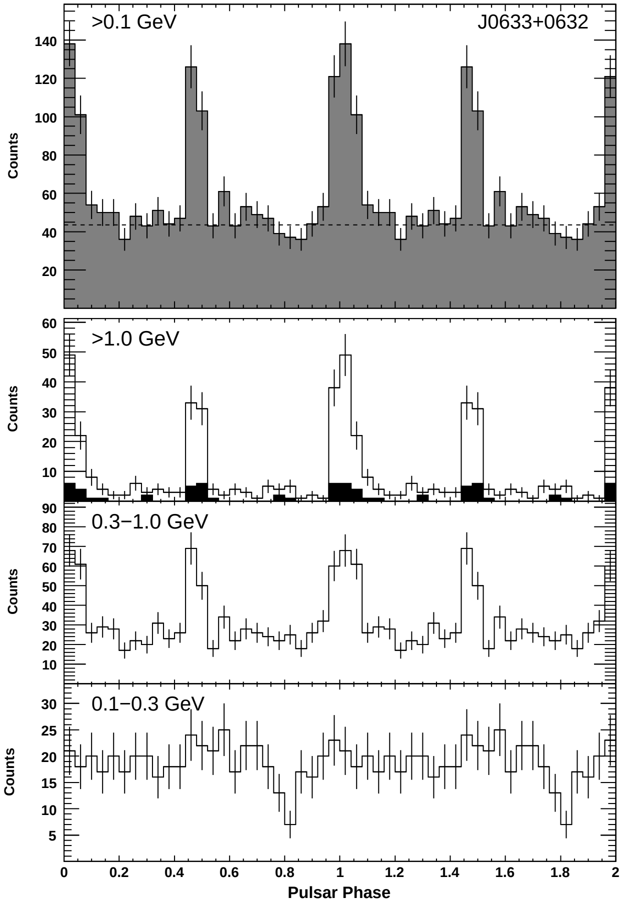

Fig. A-11.— Light curves for PSR J0633+0632 (P = 297 ms).

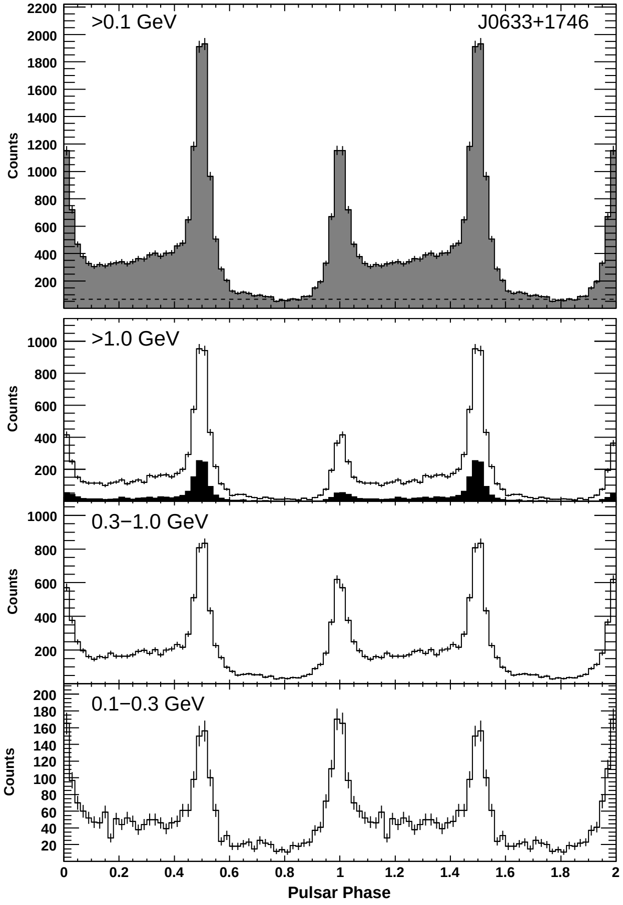

Fig. A-12.— Light curves for PSR J0633+1746 (P = 237 ms, Geminga pulsar).

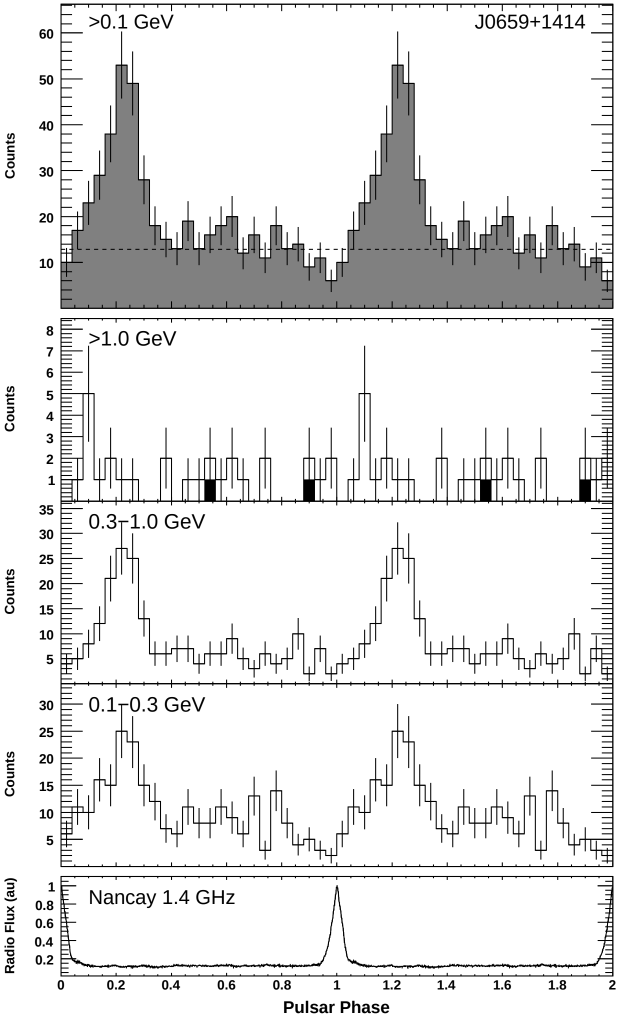

Fig. A-13.— Light curves for PSR J0659+1414 (P = 385 ms).

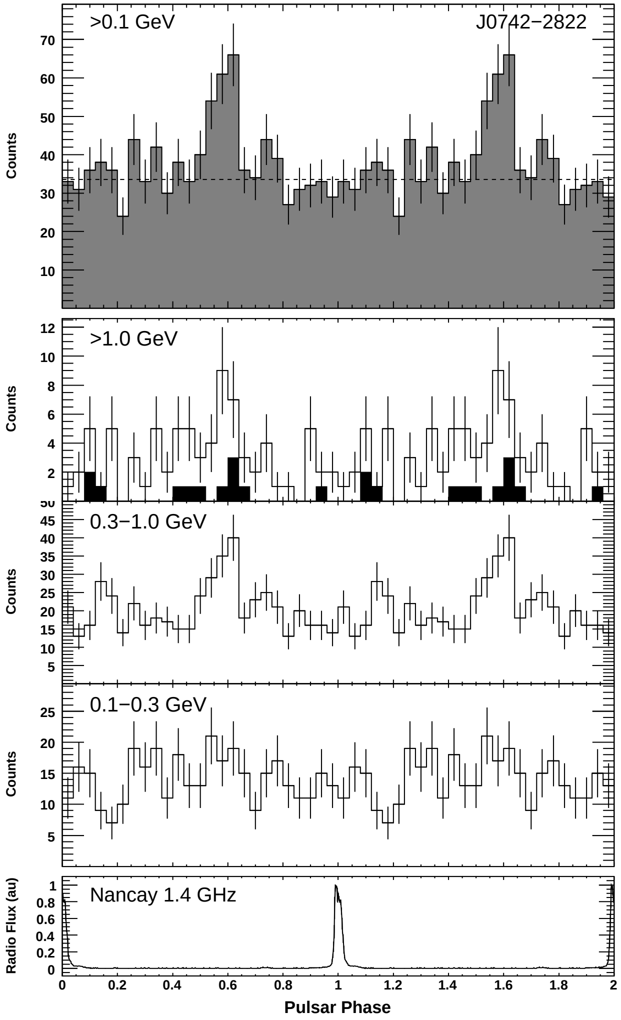

Fig. A-14.— Light curves for PSR J0742−2822 (P = 167 ms).

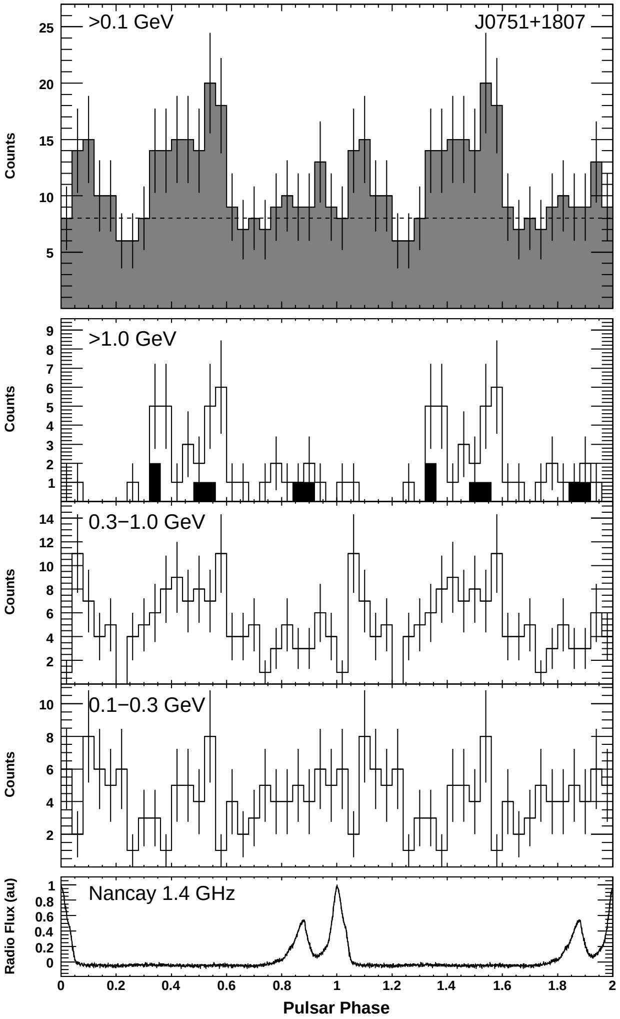

Fig. A-15.— Light curves for PSR J0751+1807 (P = 3.48 ms).

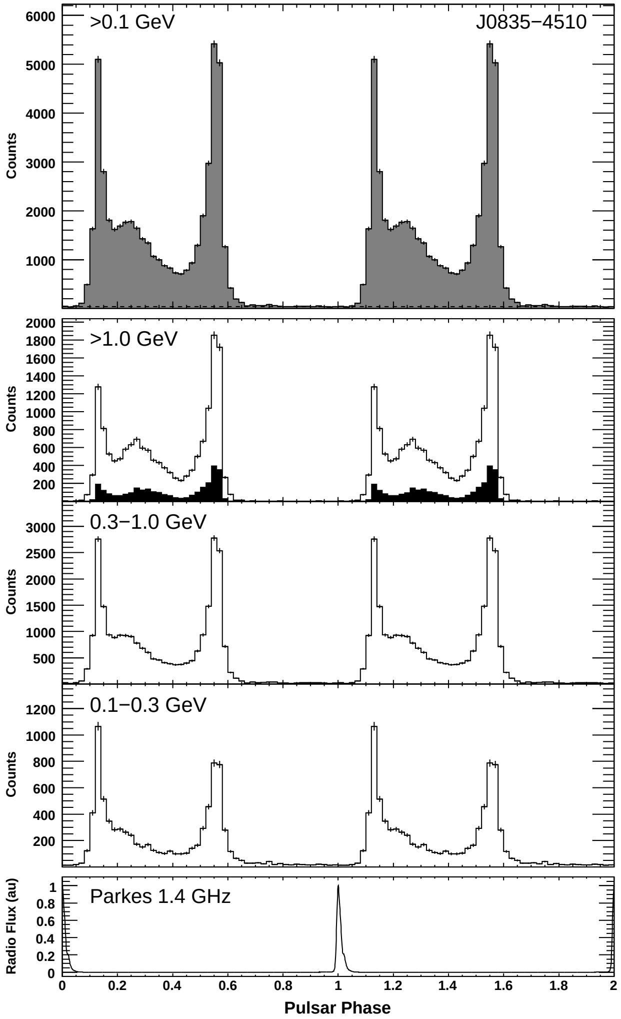

Fig. A-16.— Light curves for PSR J0835−4510 (P = 89.3 ms, Vela pulsar).

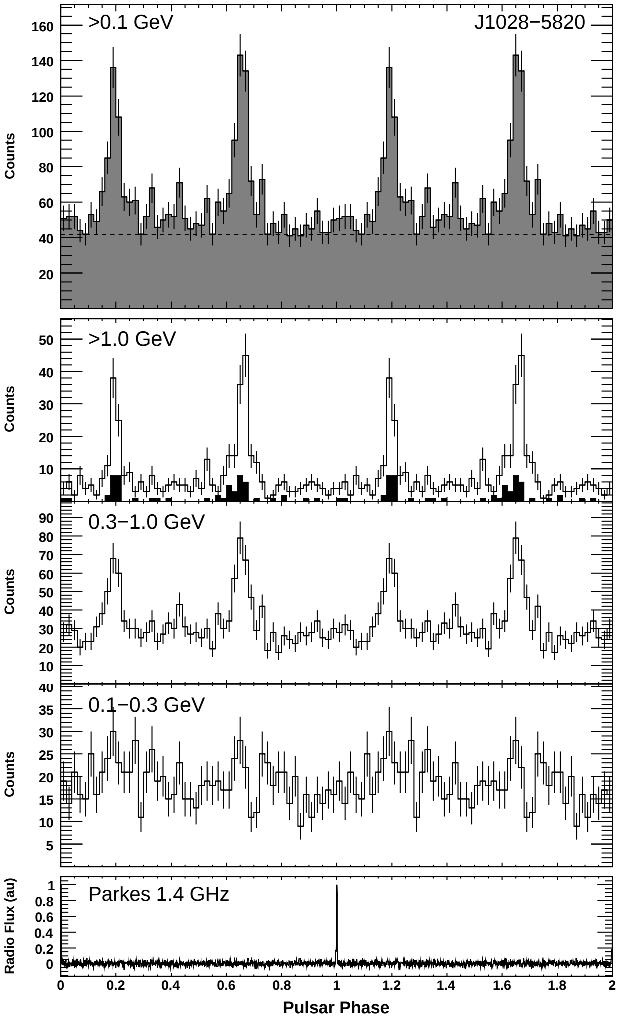

Fig. A-17.— Light curves for PSR J1028−5819 (P = 91.4 ms).

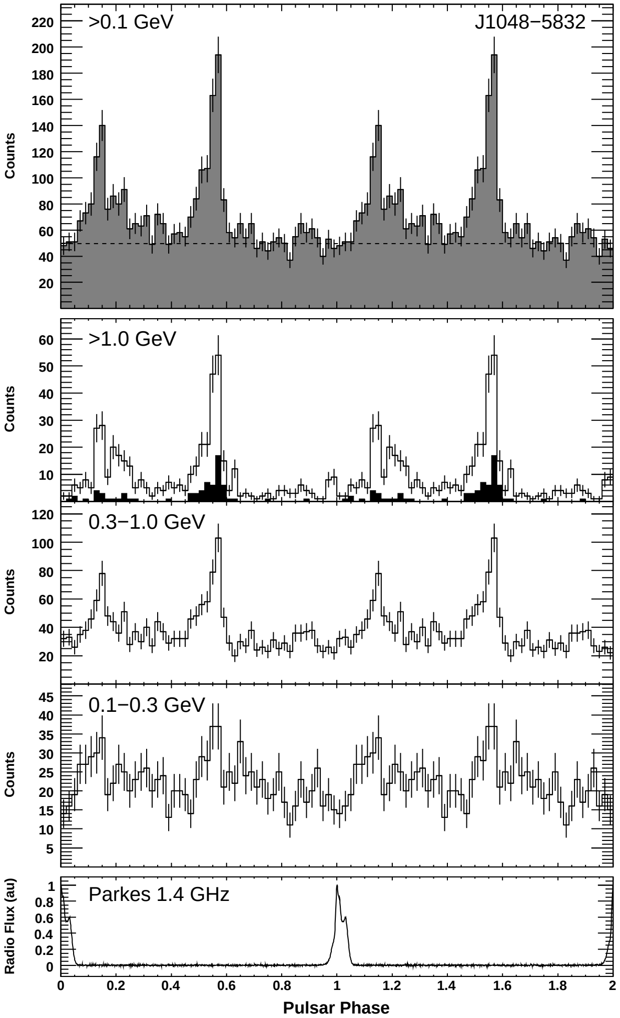

Fig. A-18.— Light curves for PSR J1048−5832 (P = 124 ms).

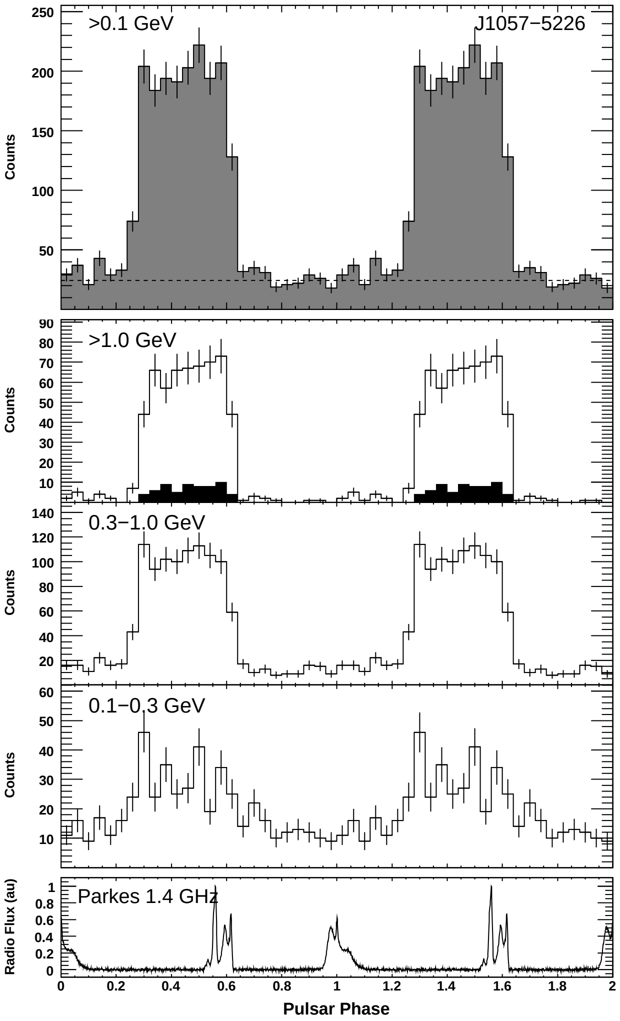

Fig. A-19.— Light curves for PSR J1057−5226 (P = 197 ms, PSR B1055−52).

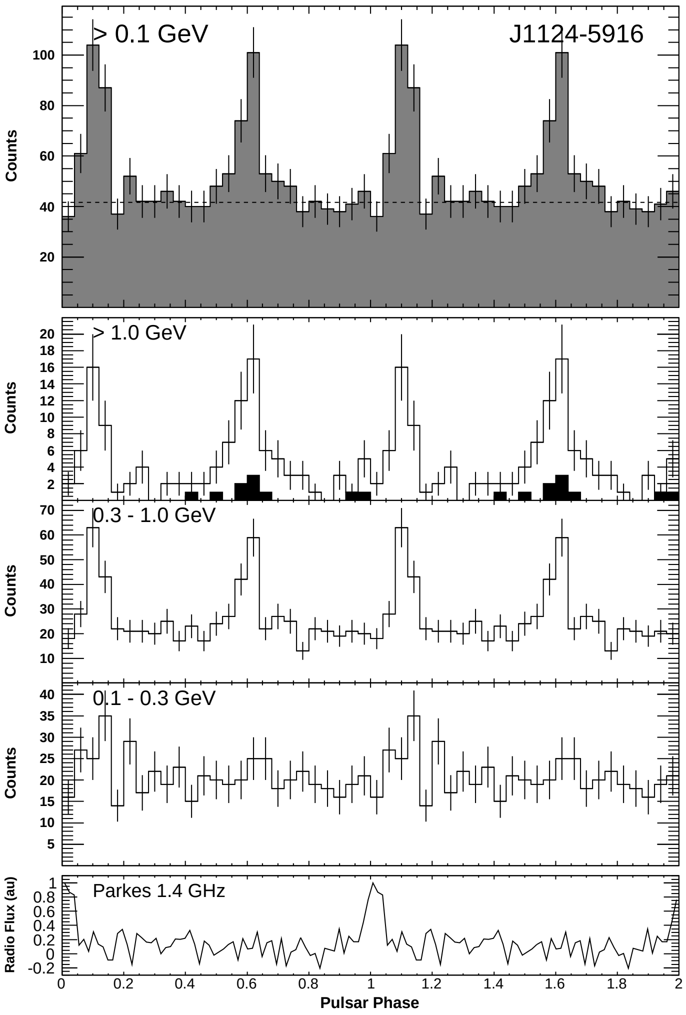

Fig. A-20.— Light curves for PSR J1124−5916 (P = 135 ms). The radio phase alignment has been corrected, as per an Erratum sent to the ApJ (December 2010).

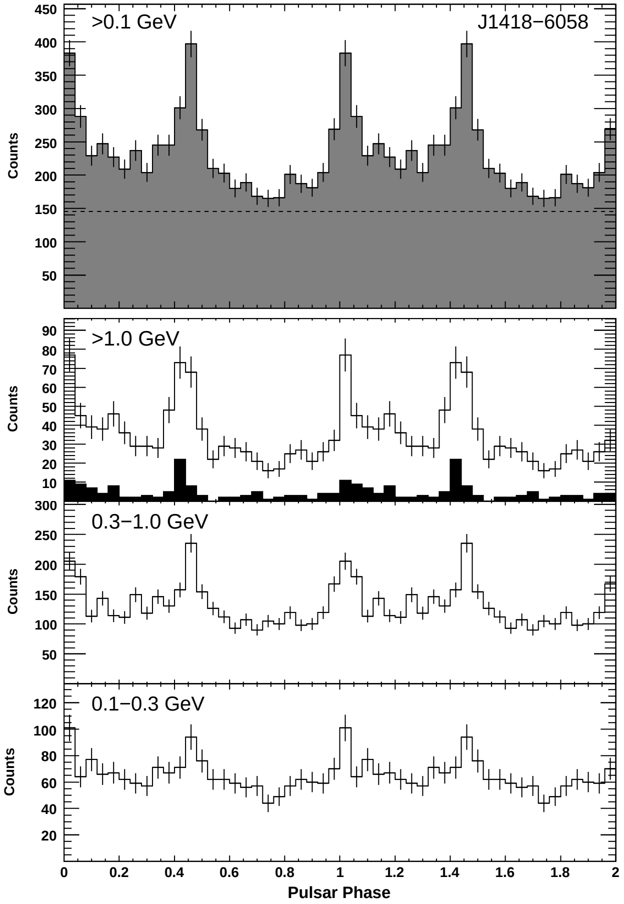

Fig. A-21.— Light curves for PSR J1418−6058 (P = 111 ms).

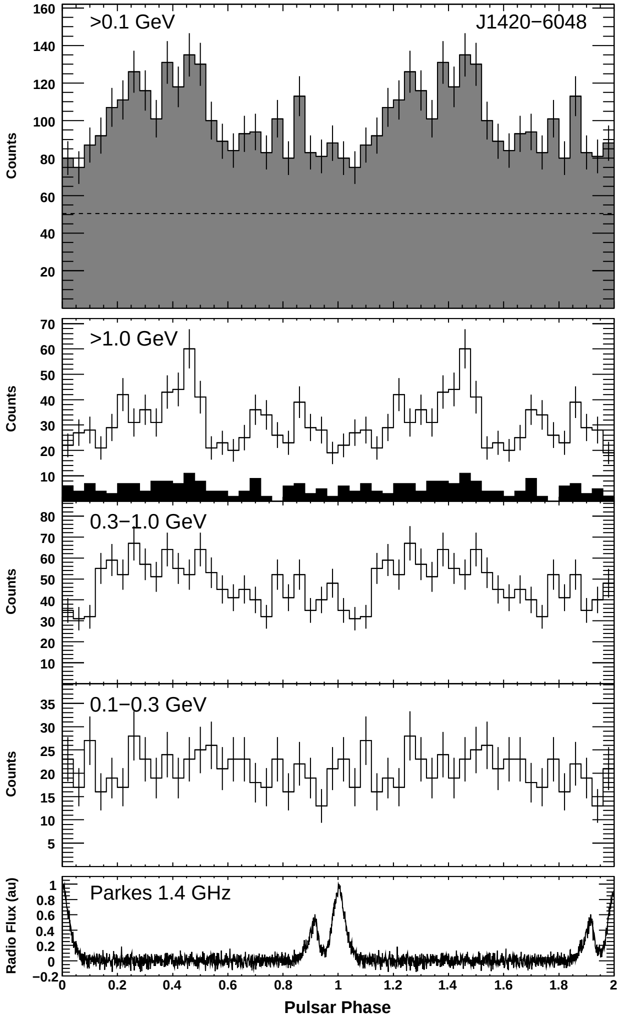

Fig. A-22.— Light curves for PSR J1420−6048 (P = 68.2 ms).

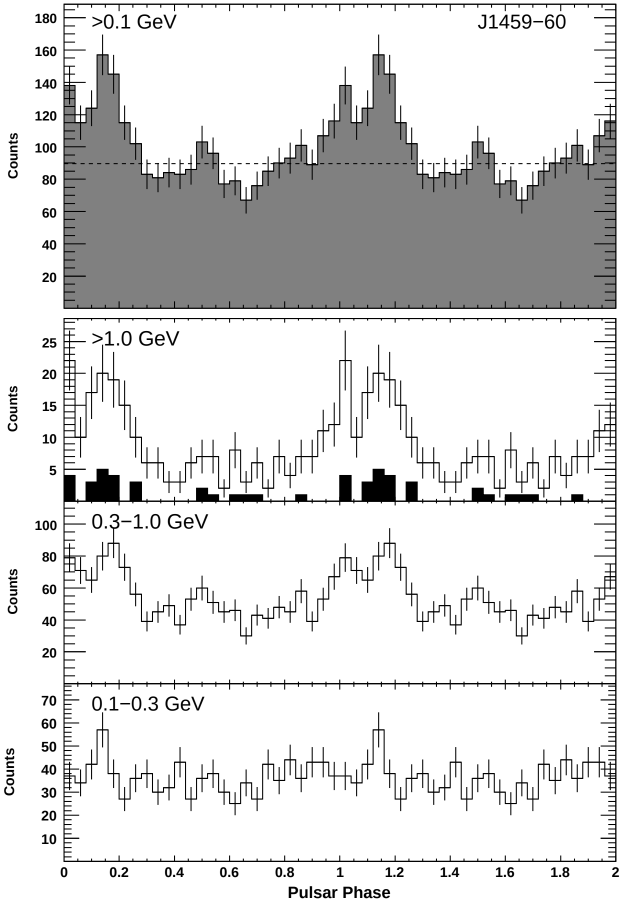

Fig. A-23.— Light curves for PSR J1459−60 (P = 103 ms).

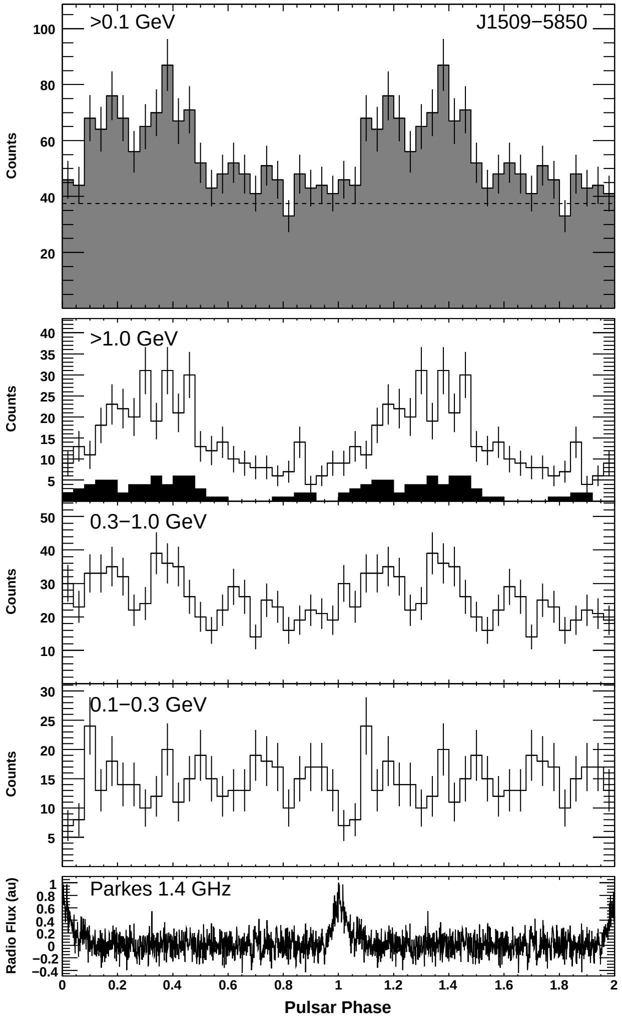

Fig. A-24.— Light curves for PSR J1509−5850 (P = 88.9 ms).

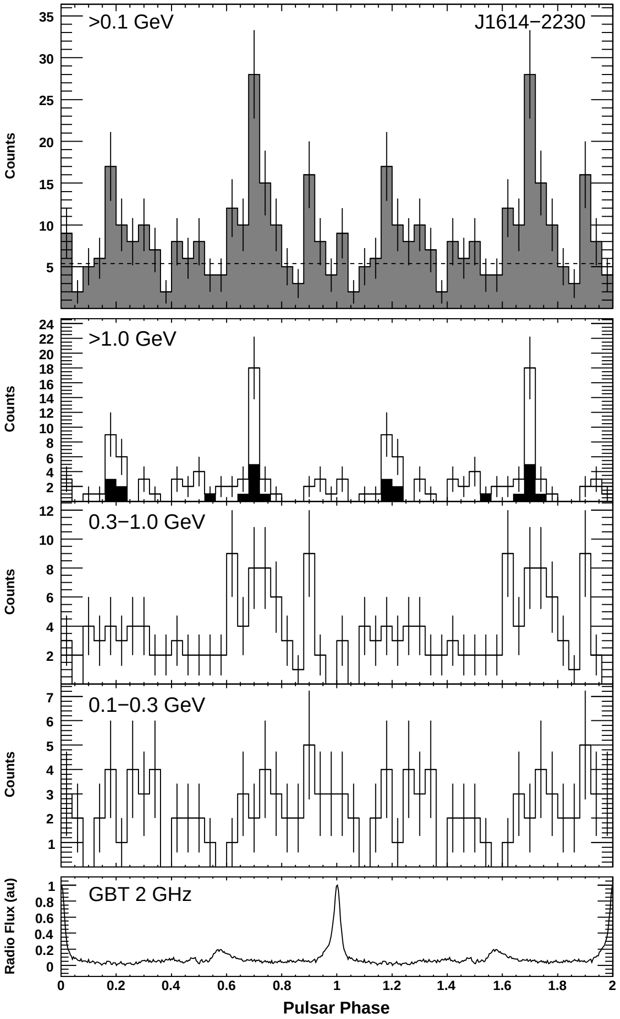

Fig. A-25.— Light curves for PSR J1614−2230 (P = 3.15 ms).

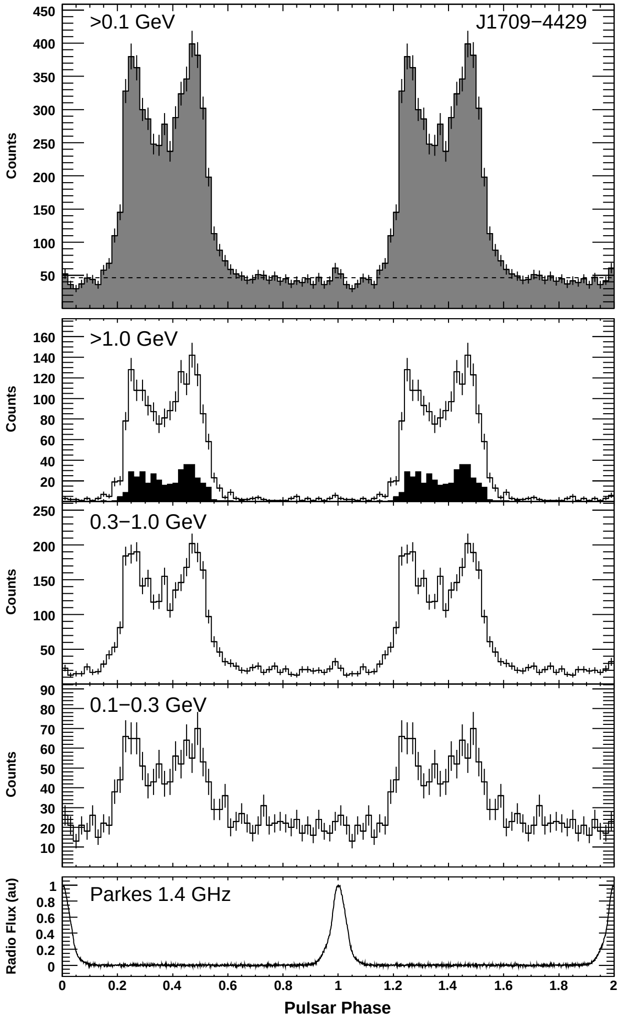

Fig. A-26.— Light curves for PSR J1709−4429 (P = 102 ms, PSR B1706−44).

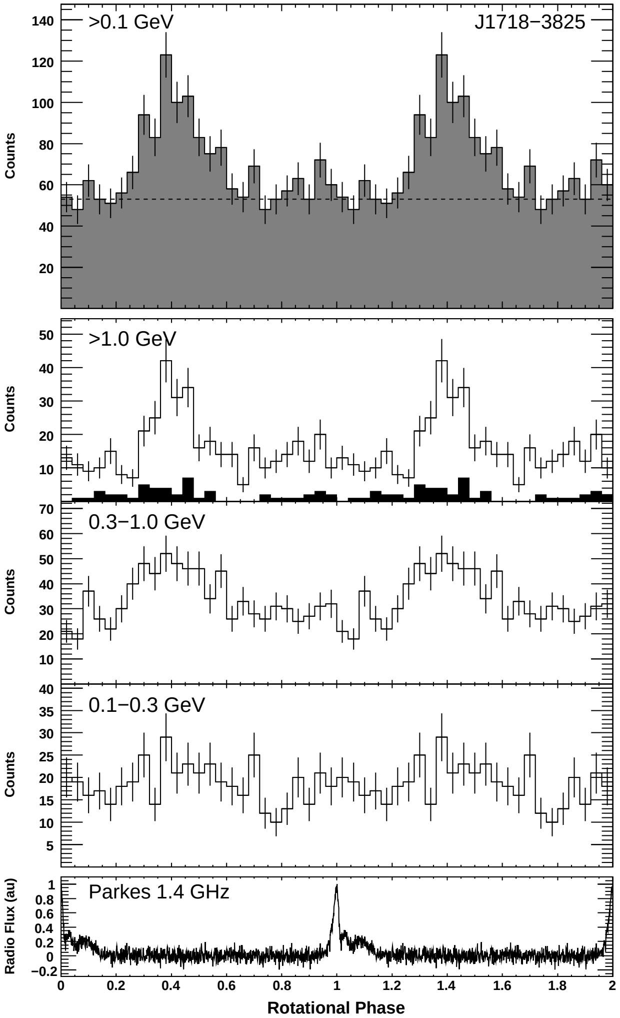

Fig. A-27.— Light curves for PSR J1718−3825 ($P = 74.7\,\mathrm{ms}$).

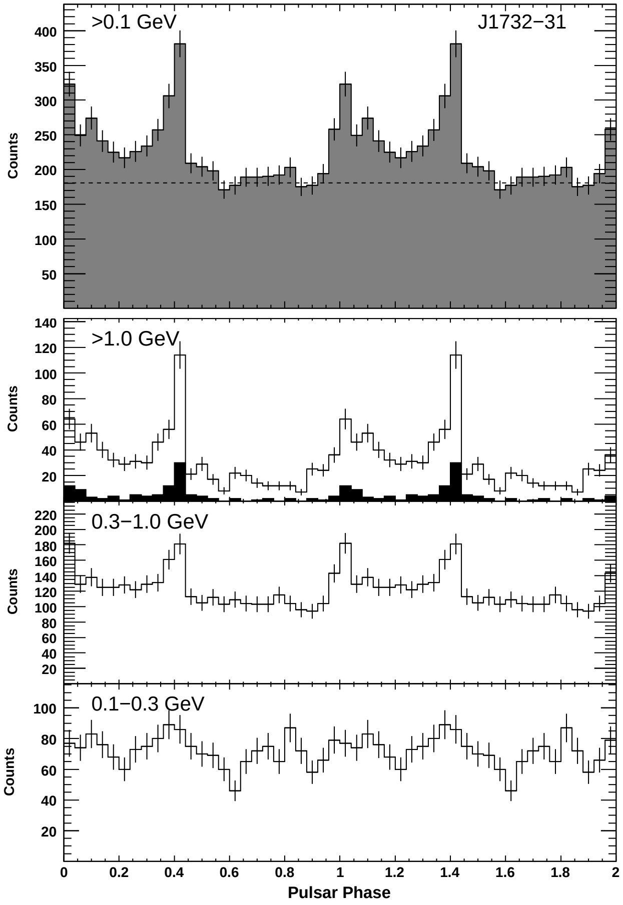

Fig. A-28.— Light curves for PSR J1732−31 ($P = 197\,\mathrm{ms}$).

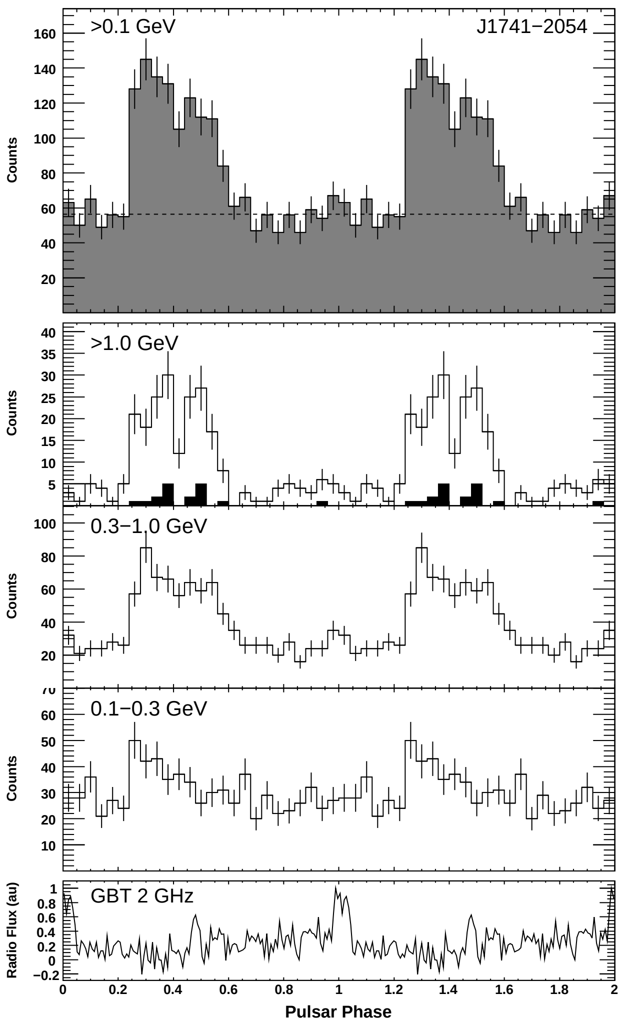

Fig. A-29.— Light curves for PSR J1741−2054 (P = 414 ms). While this pulsar is detected in the radio (Camilo et al. 2009), it was discovered by the LAT and is considered a gamma-ray-selected pulsar.

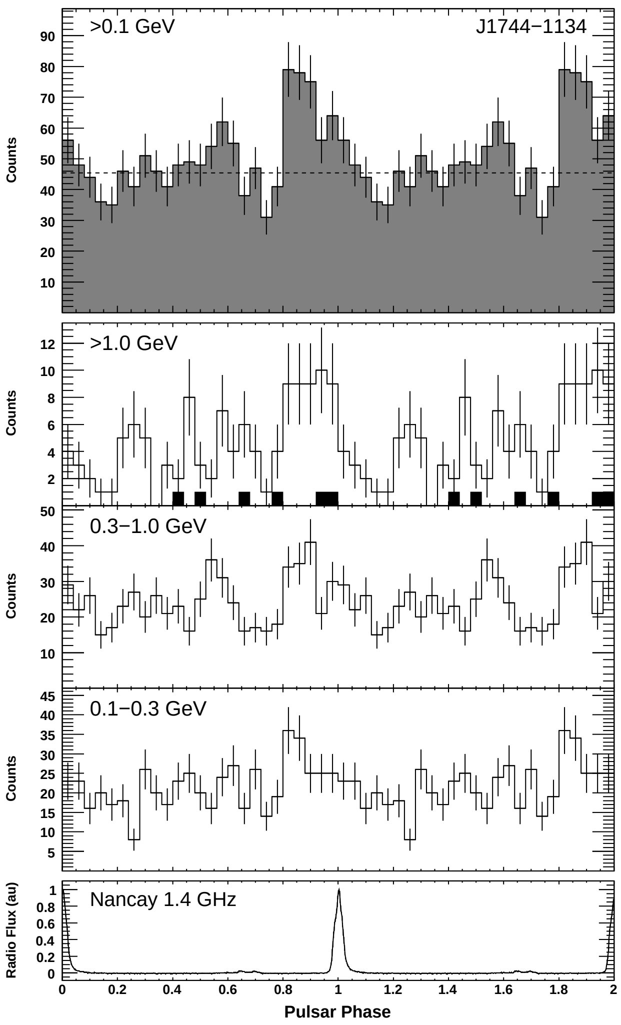

Fig. A-30.— Light curves for PSR J1744−1134 (P = 4.08 ms).

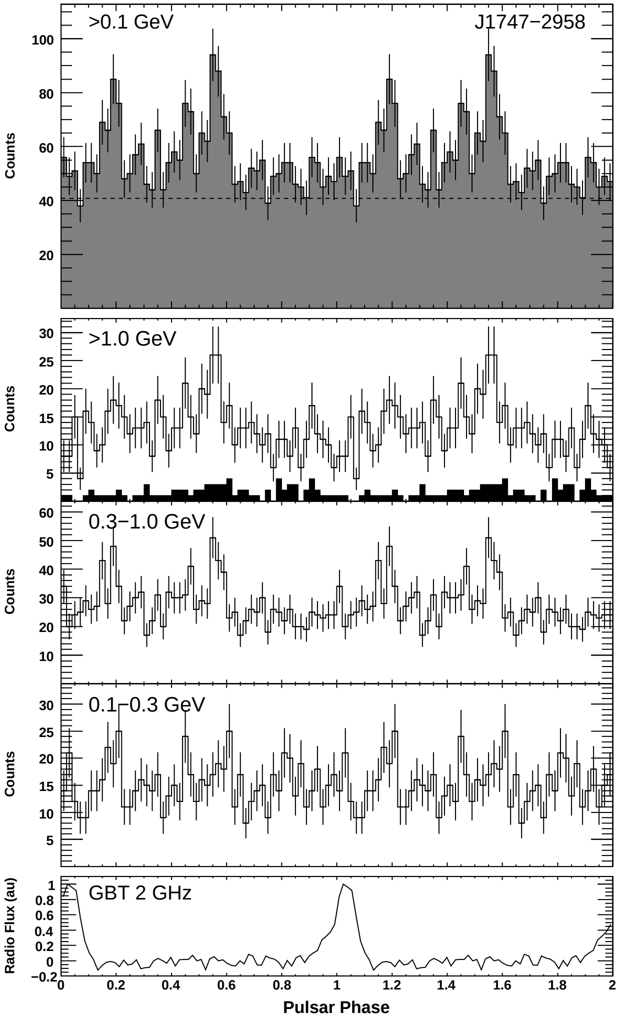

Fig. A-31.— Light curves for PSR J1747−2958 (P = 98.8 ms).

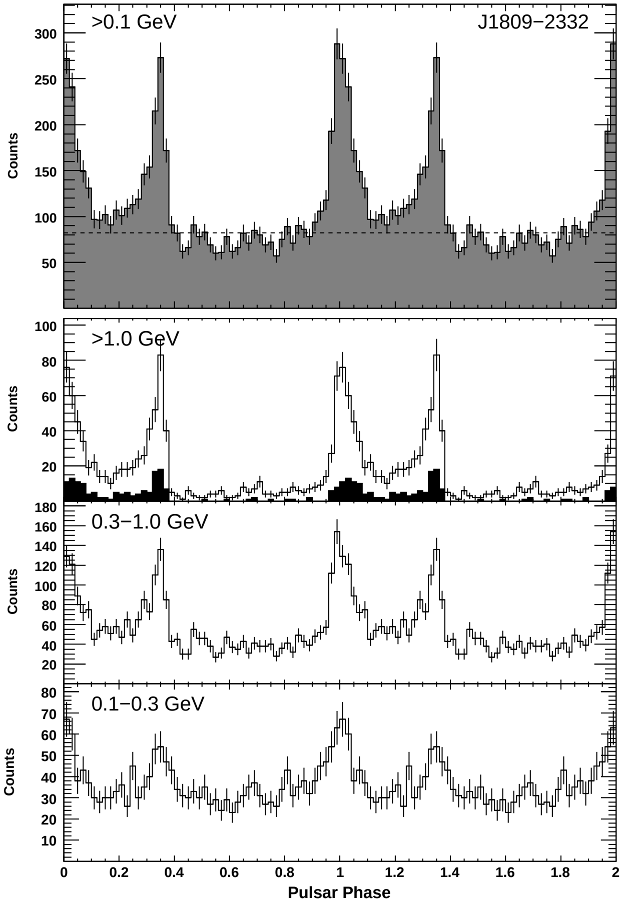

Fig. A-32.— Light curves for PSR J1809−2332 (P = 147 ms).

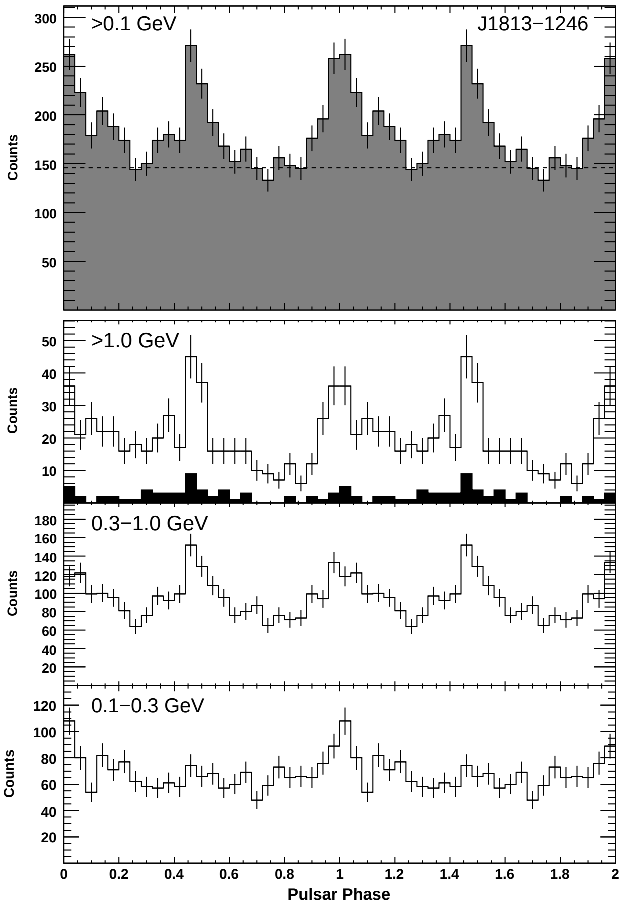

Fig. A-33.— Light curves for PSR J1813−1246 (P = 48.1 ms).

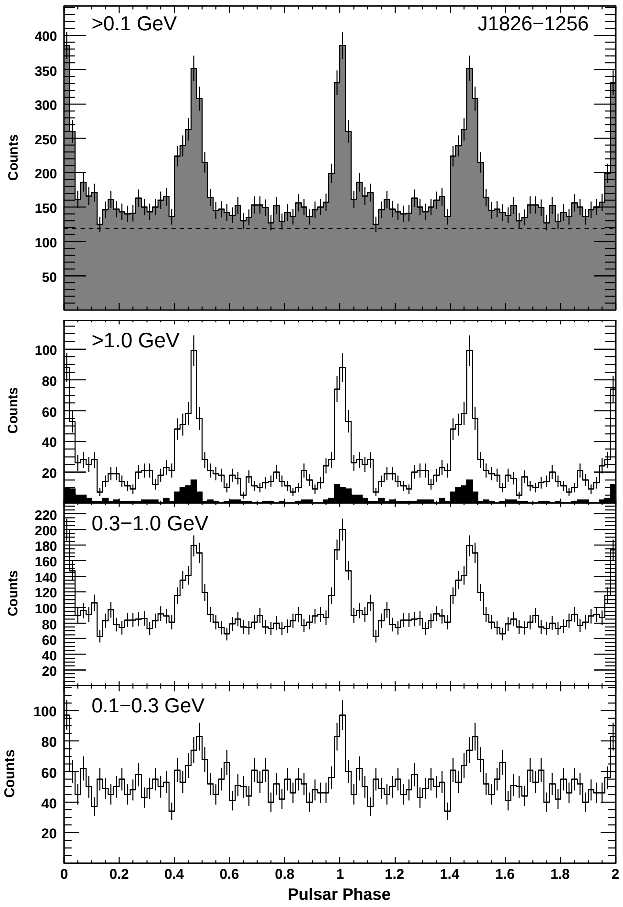

Fig. A-34.— Light curves for PSR J1826−1256 (P = 110 ms).

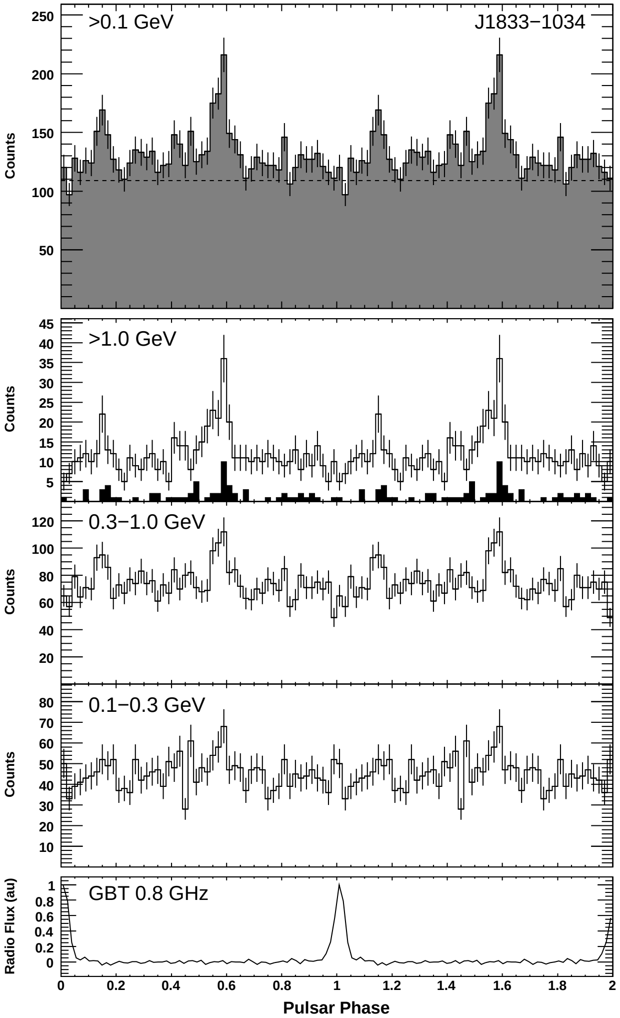

Fig. A-35.— Light curves for PSR J1833−1034 (P = 61.9 ms).

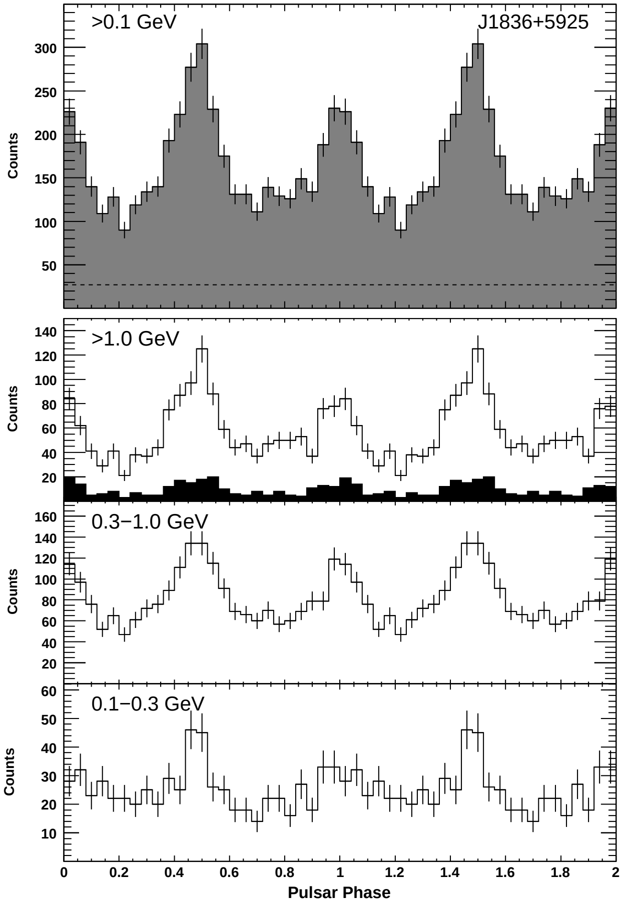

Fig. A-36.— Light curves for PSR J1836+5925 (P = 173 ms).

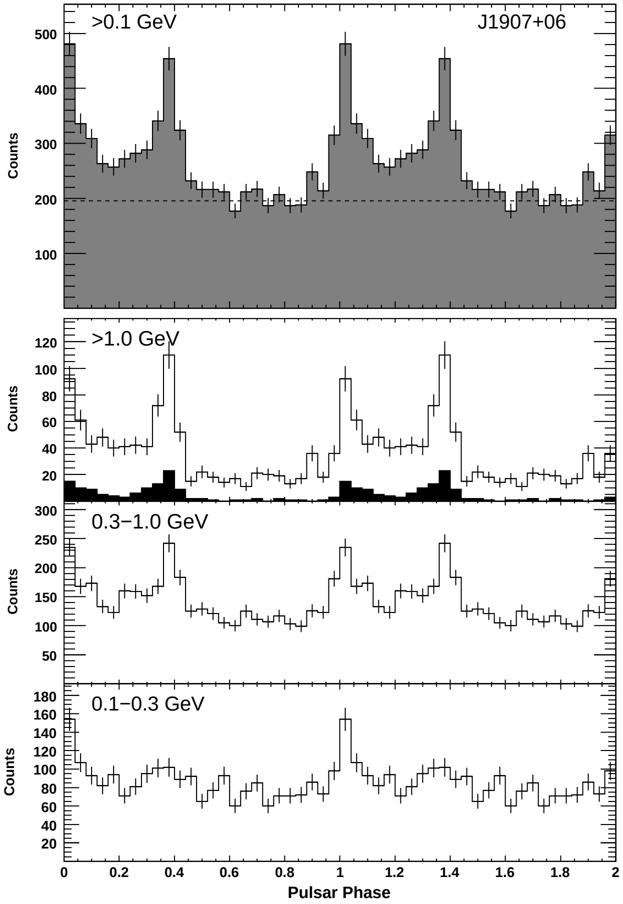

Fig. A-37.— Light curves for PSR J1907+06 (P = 107 ms).

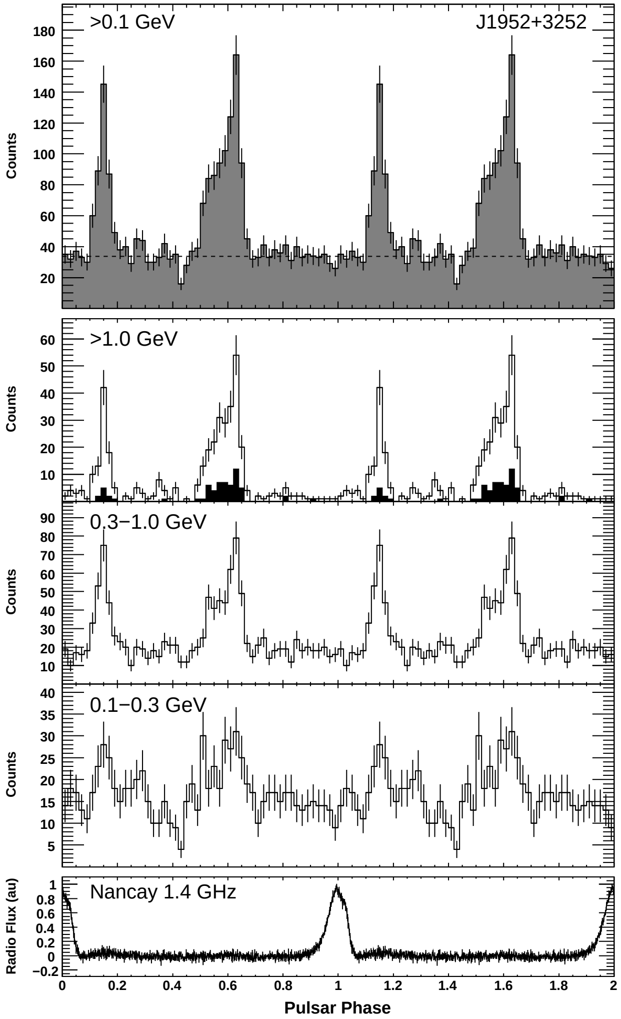

Fig. A-38.— Light curves for PSR J1952+3252 (P = 39.5 ms, PSR B1951+32).

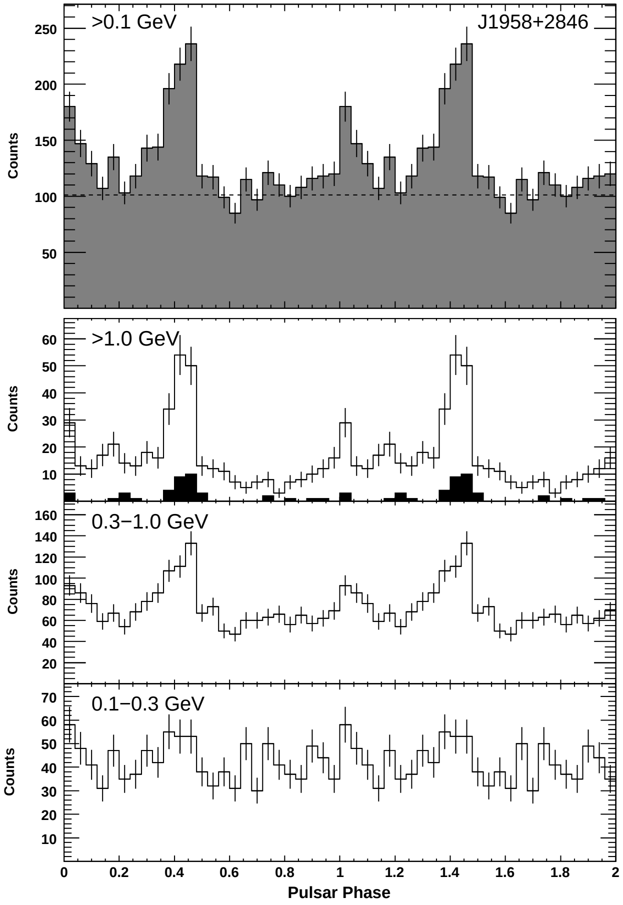

Fig. A-39.— Light curves for PSR J1958+2846 (P = 290 ms).

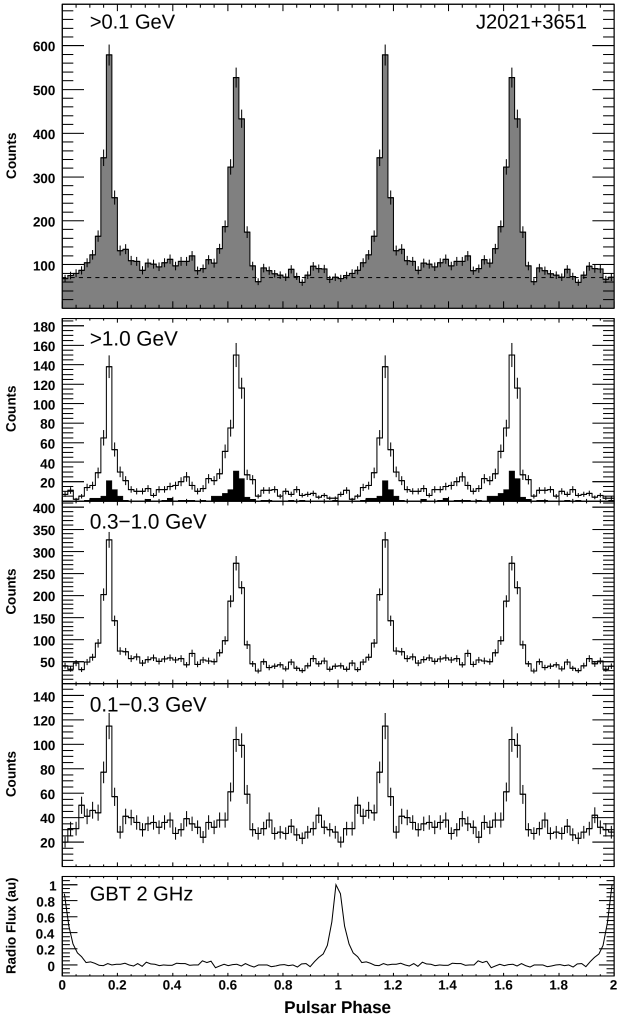

Fig. A-40.— Light curves for PSR J2021+3651 (P = 104 ms).

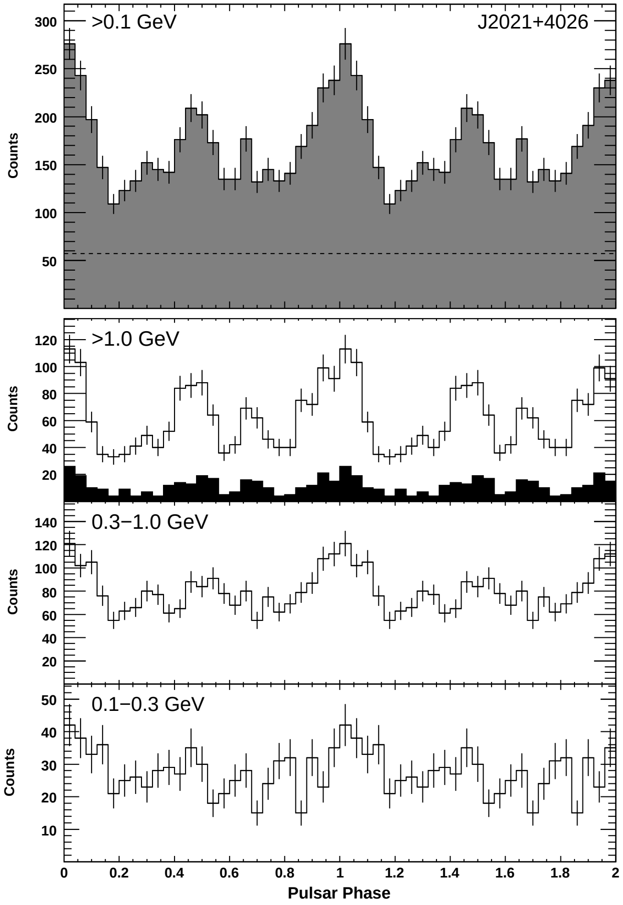

Fig. A-41.— Light curves for PSR J2021+4026 (P = 265 ms).

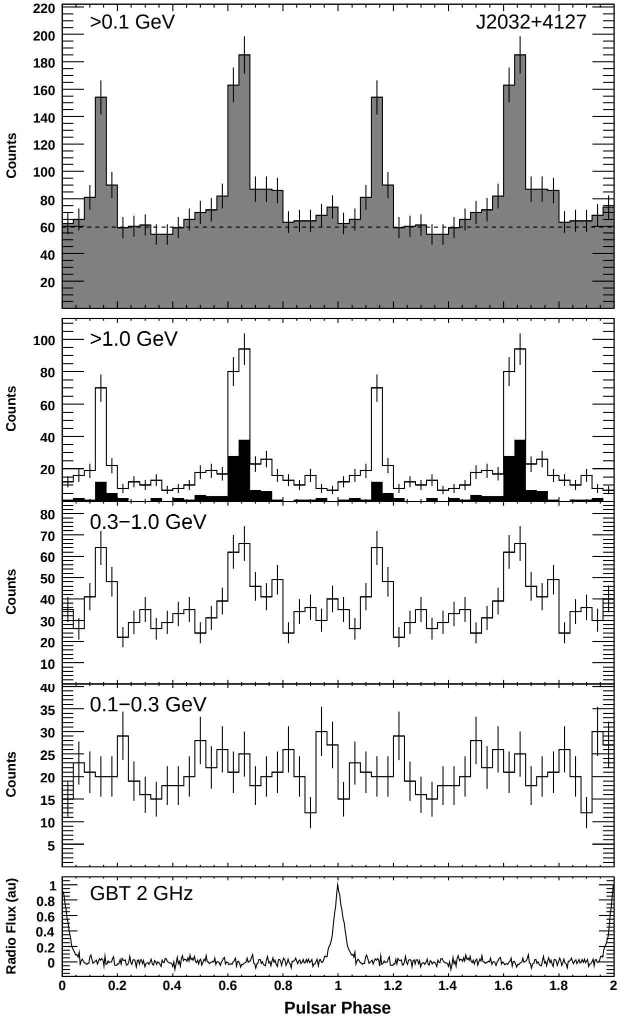

Fig. A-42.— Light curves for PSR J2032+4127 (P = 143 ms). While this pulsar is detected in the radio (Camilo et al. 2009), it was discovered by the LAT and is considered a gamma-ray-selected pulsar.

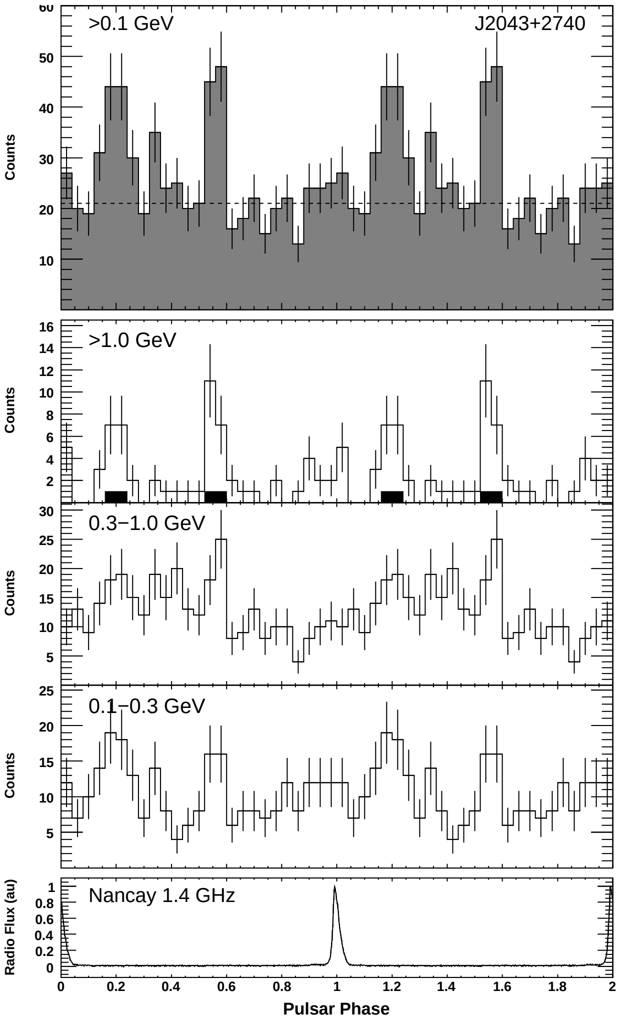

Fig. A-43.— Light curves for PSR J2043+2740 (P = 96.1 ms).

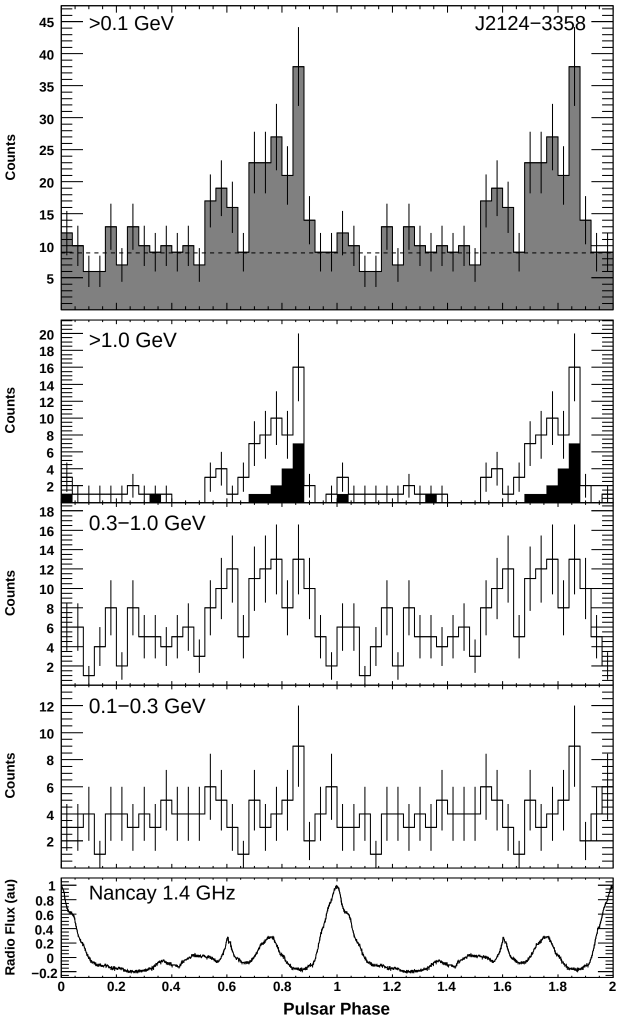

Fig. A-44.— Light curves for PSR J2124−3358 (P = 4.93 ms).

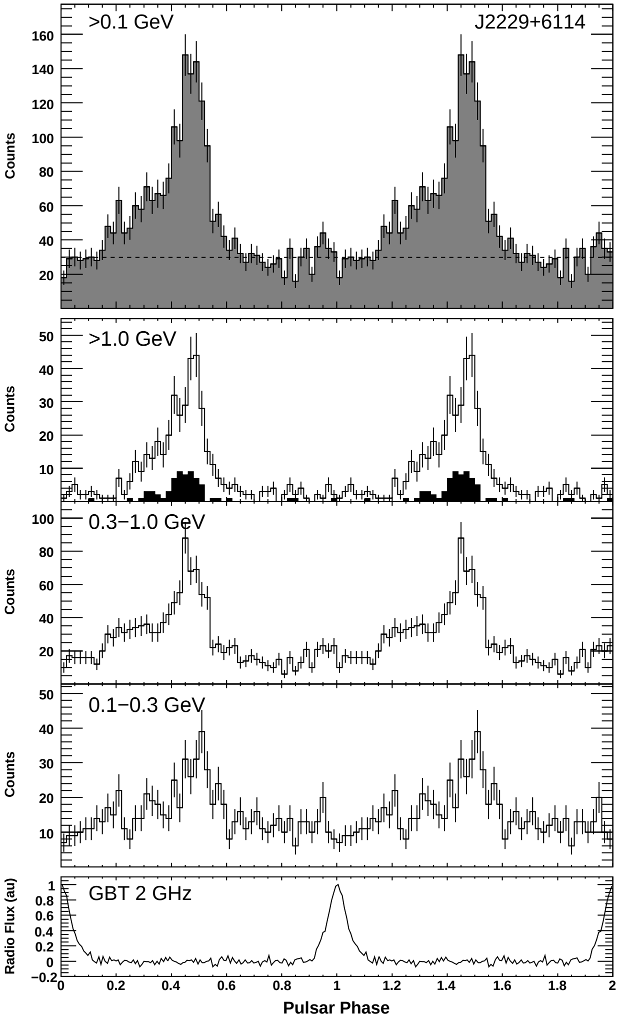

Fig. A-45.— Light curves for PSR J2229+6114 ($P = 51.6\,\mathrm{ms}$).

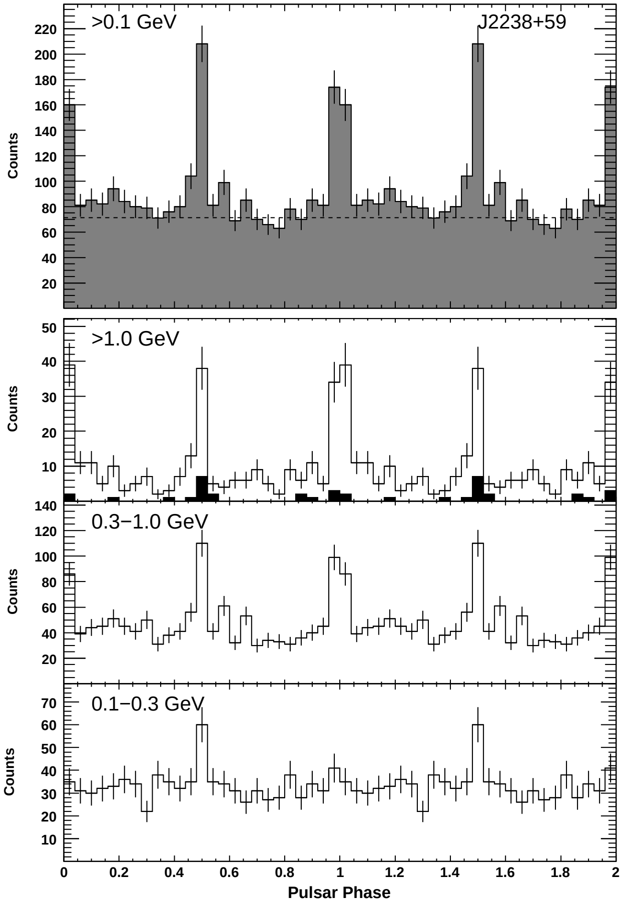

Fig. A-46.— Light curves for PSR J2238+59 ($P = 163\,\mathrm{ms}$).